TECHNISCHE UNIVERSITÄT MÜNCHEN

Lehrstuhl für Biologische Bildgebung

Computational Modeling of Signal Mechanisms for High Resolution Positron Imaging of Tumor Metabolism

Qian Wang

Vollständiger Abdruck den von der Fakultät für Elektrotechnik und Informationstechnik der Technischen Universität München zur Erlangung der akademischen Grades eines

Doktor der Naturwissenschaften

genehmigten Dissertation.

Vorsitzender:	Univ.-Prof. Dr. Norbert Hanik
Prüfer der Dissertation:	1. Univ.-Prof. Dr. Vasilis Ntziachristos
	2. Univ.-Prof. Dr. Bjoern Menze
	3. apl. Prof. Dr. Sibylle Ziegler

Die Dissertation wurde am 13.03.2015 bei der Technischen Universität München eingereicht und durch die Fakultät für Elektrotechnik und Informationstechnik am 13.07.2015 angenommen.

Computational Modeling of Signal Mechanisms for High Resolution Positron Imaging of Tumor Metabolism

Qian Wang

München 2015

Abstract

High-resolution positron imaging of tumor metabolism has previously been applied for some preclinical and intraoperative clinical applications. However, the interpretation of measured positron signals with respect to the underlying physiology is not straightforward and less quantitative. This thesis developed computational modeling methods to investigate the mechanisms of substrate and positron-emitting tracer metabolisms in solid tumors, and positron depositions in a silicon detector in the imaging process. A novel tumor physiology model was proposed to describe the interactions of relevant key metabolites within the network of metabolic pathways. The quantitative relationship between pathophysiological factors (such as expressions of enzyme, transporter and transcriptional factors, and vascular distribution) and tumor metabolism was established to support molecular imaging analysis. To understand the physical principles of positron imaging, the traversing processes of positrons in the silicon detector was modeled by Monte-Carlo simulation. In particular, we developed for the first time a machine learning approach to improve the spatial resolution by classifying the primary pixels within the detector using support vector machine. The classification model was constructed by learning the features of positron trajectories based on Monte-Carlo simulations. Computational modeling helps to capture the metabolic characteristics behind the positron imaging signals, provides an in-depth understanding of co-influences of physiological and system factors on measured signals, and has the potential to accelerate the development of positron imaging for clinical and preclinical applications.

Zusammenfassung

Hochauflösende Positronen-Bildgebung des Tumor-Metabolismus wurde in früheren Arbeiten schon auf präklinische und intraoperative klinische Anwendungen angewendet. Jedoch ist die Interpretation von gemessenen Positronen-Signalen in Hinblick auf die zugrundeliegende Physiologie sehr anspruchsvoll und bislang wenig quantitativ. In dieser Arbeit wurden Computermodelle entwickelt, um den Mechanismus von molekularer Bildgebung in soliden Tumoren zu untersuchen und um die Positronenwechselwirkung in einem Siliziumdetektor bei der Positronen-Bildgebung zu bestimmen. Eine neuartiges Modell der Tumor-Physiologie wurde vorgeschlagen, um die Wechselwirkungen von relevanten Schlüssel-Stoffwechselprodukten in dem Netzwerk von Stoffwechselwegen zu beschreiben. Eine quantitative Beziehung zwischen pathophysiologischen Faktoren (wie Expressionen von Enzymen, Transport und transkriptionelle Faktoren und Gefäßverteilung), und dem Tumor-Metabolismus wurde etabliert, um die Analyse der molekularen Bildgebung zu unterstützen. Um die physikalischen Prinzipien der Positronen-Bildgebung zu verstehen, wurde der im Siliziumdetektor ablaufende Prozess durch Monte-Carlo-Simulation modelliert. Insbesondere haben wir zum ersten Mal einen Ansatz entwickelt, der maschinelle Lerntechniken mit Unterstützung der Support-Vektor-Maschine verwendet, um die räumliche Auflösung durch Klassifizierung von Primär-Pixeln innerhalb des Positronen-Detektors zu verbessern. Die Klassifizierung wurde durch das Erlernen der Eigenschaften der Prositronen-Bahnen im Detektormaterial konstruiert, die auf Monte-Carlo-Simulationen basieren. Rechnerische Modelle können helfen, die metabolischen Merkmale hinter den Signalen der Positronen-Bildgebung zu erfassen. Sie geben ein tieferes Verständnis des Einflusses der physiologischen Faktoren und der Systemfaktoren auf die gemessenen Signale und besitzen das Potential, die Entwicklung von Positron-Bildgebung für klinische und vorklinische Anwendungen zu beschleunigen.

Acknowledgements

I would like to express my deepest appreciation to my supervisor: **Prof. Dr. Sibylle Ziegler**. You have been a tremendous mentor for me. I would like to thank you for encouraging my research and for allowing me to grow as a research scientist. Your advices on my researches and career have been invaluable.

I also would like to express my sincere gratitude to my supervisor: **Prof. Dr. Vasilis Ntziachristos** for offering me the opportunity to become your PhD student, and quite constructive suggestions on my researches and thesis. I also remain indebted for your understanding and supports on my way to graduation and pursuing future academic career.

I would especially like to thank **Dr. Kuangyu Shi** who has made great efforts to support me with my research and scientific career. He provides me a lot of wonderful experiences on research and manuscripts. He showed the attitude and the substance of a genius: he continually and persuasively conveyed a spirit of adventure in regard to research. Without his supervision and constant help this dissertation would not have been possible.

I gratefully acknowledge **Prof. Dr. Bjoern Menze** for his kindness to be the examiner of my doctoral exam. I want to thank you for your quite precious suggestions on my thesis and researches.

I would like to thank my colleagues and friends for their great favors on my studies and lives. I express my hearted gratitude toward **Liang Si** for the tremendous endorsements you gave on my life and career. My sincere thanks go to my dear colleagues **Zhen Liu** and **Xiaoyin Cheng** for the wonderful collaborations and discussions on biology, physiology and techniques.

A special thanks to my family. Words cannot express how grateful I am to **My Parents** for all of the sacrifices that you've made on my behalf. You sustained me on every aspect of my life with your all-enduring and most selfless love. In my most difficult periods, it is you that encourage me to persist on pursuing my dreams. I want to present this dissertation to you for all the loves you have given to me.

Contents

1. Introduction

Molecular imaging enables the non-invasive visualization of the cellular function and the follow-up of the molecular process in living organisms, and opens up an incredible number of exciting possibilities for clinical and preclinical applications [1]. An important application of molecular imaging involves monitoring tumor metabolic processes for the in-depth understanding of mechanisms behind the tumor formation, progression and metastasis [2]. With these knowledge, the tumor diagnosis, treatment and prognosis are hopefully improved. This chapter will present an overview of tumor pathophysiology and molecular imaging, in particular the modalities that may be used for high-resolution imaging of tumor metabolism, to sustain the studies of computation modeling of positron imaging of tumor metabolism in this thesis.

1.1. Overview of molecular imaging

The molecular imaging that has emerged in recent decades originates from the field of radio-pharmacology due to the need to better understand fundamental molecular pathways inside organisms in a noninvasive manner. It enables the visualization of the cellular function and the follow-up of the molecular process in living organisms without disturbing them. Unlike the previous methods of imaging which primarily image differences in qualities such as density or water content, molecular imaging uses probes (known as biomarkers) to help image particular targets and pathways [3].

The entire molecular imaging research chain is driven by molecular targets [3]. The choice of molecular target depends on given biological questions and disease management problems. The selected targets should be abundant and specified for the studied disease process to achieve a successful molecular imaging assay. The targets are imaged with the help of probes. In most strategies, a molecular imaging probe (or probes) must first be introduced into the living subject (*e.g.*, by injection into the blood stream). The probes can be small molecules, peptides, aptarmers, engineered proteins or even more complex nanoparticles. After injection, the specific component of the probe interacts with the intended molecular target, producing a signal that can hopefully be detected. The probes are then tested in-vitro (extracts of cells or intact cells in cell culture) and in-vivo (animal model) with appropriate imaging modality. The in-vitro test provides better understanding of the probe's ability to traverse the cell membrane and interact with targeting and clearance from cells. The in-vivo test allows the examination of pharmacokinetics and bio-distribution of the probe, and the optimization of administration routes and probe injection masses to achieve desired signal, signal-to-background ratio. The next step concerns the quantification and visualization issues in the animal model and cell-level model. These issues involve developing various algorithms for the image reconstruction and pharmacokinetics using the dynamic images acquired, mathematical modeling of organism metabolism and other statistical analysis. The research chain ends with translating the molecular imaging strategy into the clinical applications which requires obtaining approval from appropriate agencies.

There are many different modalities that can be used for non-invasive molecular imaging, such as magnetic resonance imaging (MRI), optical imaging, single photon emission computed tomography (SPECT), positron emission tomography (PET) and other molecular imaging methods. They are applied based on different imaging principles, using different biomarkers and are oriented toward a variety of illnesses.

MRI scanners use strong magnetic fields and radio waves to form images of the body and have been applied in the imaging of neuro, cardiovascular, musculoskeletal liver and gastrointestinal

and oncologic systems [4-6]. Hydrogen is the most frequently imaged nucleus in MRI because it is present in biological tissues in great abundance. Many other nuclides with a net nuclear spin could potentially be imaged with MRI, such as ^{3}He, ^{7}Li, ^{13}C, ^{17}O, ^{19}F, ^{23}Na, ^{31}P and ^{129}Xe. MRI has been modified for specialized applications, *e.g.*, diffusion MRI, magnetic resonance angiography (MRA), magnetic resonance spectroscopy (MRS), functional MRI, real-time MRI, interventional MRI, etc.

Optical imaging depends on fluorescence, bioluminescence, absorption or reflectance as the source of contrast [7]. It is characterized by high resolution while only superficial visible region due to its short penetration depth [8]. The imaging agent is usually metabolic substrates or proteins labeled with near-infrared (NIR) fluorophores, such as NIR fluorophores labeled αvβ-integrin, epidermal growth factor (EGF), pamidronate, glycosylphosphatidylinositol, human serum albumin, 2-Deoxy-D-glucose [9-12]. These infrared dye-labeled probes are used to target a variety of cancers, brain, osteoblasts, lymph nodes, etc.

SPECT is a nuclear medicine tomographic imaging technique using gamma rays which enables the acquisition of 3D information. The gamma rays come from the gamma-emitting radioisotope delivered into the patient through injection into the bloodstream. There are a range of radioisotopes (*e.g.*, ^{99m}Tc, ^{123}I, ^{131}I, ^{111}In, ^{201}Tl) that can be used depending on the specific application [13-15]. Typical applications include scanning of bone, myocardial perfusion, sestamibi parathyroid, white cells, brain tissue, etc. [13-15].

Similar to SPECT, PET is also a nuclear medicine imaging technique which produces a three-dimensional image or picture of functional processes in the body [1, 16, 17]. However, it detects two 511 keV photons from positron annihilation to estimate the density of the original molecule in the measured areas. The typical isotopes include ^{11}C, ^{13}N, ^{15}O, ^{18}F, ^{64}Cu, ^{62}Cu, ^{124}I, ^{76}Br, ^{82}Rb and ^{68}Ga, with ^{18}F being the most clinically utilized. PET as both a medical and research tool has been used heavily in clinical oncology (medical imaging of tumors and the search for metastases) and for clinical diagnosis of certain diffuse brain diseases such as those causing various types of dementias.

Positron imaging with beta probe or camera has been developed in recent years mainly for preclinical applications [18-20]. They measure the positrons directly before their annihilations and therefore have the advantage of high sensitivity and high spatial resolution (for the beta camera). Using kinetic modeling for analyzing the measured activities, cellular metabolic processes can be monitored in real time.

1.2. Tumor pathophysiology

A tumor, also known as a neoplasm, is an abnormal growth of tissue. Its physiology is uniquely different from that of normal tissues. It is characterized by oxygen depletion, extracellular acidosis, high lactate and adenosine levels, glucose and bicarbonate deprivation, energy impoverishment, significant interstitial fluid flow, etc. [21]. Tumors can be classified into four main groups: benign tumors, in situ tumors, malignant tumors, and tumors of uncertain or unknown behavior. A malignant tumor is a cancer, which involves abnormal cell growth with the potential to invade or spread to other parts of the body. Its characteristics are proposed as self-sufficiency in growth signaling, insensitivity to anti-growth signals, evasion of apoptosis, enabling of a limitless replicative potential, induction and sustainment of angiogenesis, activation of metastasis and invasion of tissue [22]. Cancer has a reputation as a deadly disease and therefore has attracted considerable attention for its treatment, diagnosis and prognosis to increase population survival.

The tumor microenvironment is an intricate and diversified system, and characterized by a series of crucial features distinct from the normal tissues [21]. The severe structural and functional abnormality of tumor microvessels is one of these crucial features. It comprises a disorganized vascular network, increased intervessel distances, existence of avascular areas, large diameter microvessels, enlongated, tortuous vessels, arterio-venous anastomoses, the absence of flow regulation, etc. [21, 23, 24]. The chaotic network of microvessels results from tumor angiogenesis, a process by which new blood vessels develop from an existing vasculature, through endothelial cell sprouting, proliferation, and fusion [25, 26]. As the basis of supporting tumor system and channels for nutrient and oxygen supply and waste removal, tumor microvasculature significantly influences the tumor physiology, such as oxygenation and glucose metabolism.

Tumor oxygenation status is highly homogeneous and the prevalence of hypoxic tissue areas (*i.e.* areas with O_2 tensions [pO_2] $\leq$ 2.5 mmHg) is the key pathophysiological property. They are found in a wide range of human malignancies including cancers of the breast, uterine cervix, vulva, head and neck, prostate, rectum, pancreas, brain tumors, etc. [21]. Tumor hypoxia results from the imbalance between the supply and consumption of oxygen. The limited oxygen supply arises as the result of inadequate perfusion (due to structural and function abnormalities of the tumor microcirculation) and increased diffusion distances. The diminished oxygen availability leads to substantial limitations in the efficacy of oxygen dependent treatments such as standard radiotherapy and O_2-dependent chemotherapy. Tumor hypoxia primarily causes impairment of cell proliferation and eventually induces the death of both normal and most tumor cells. However,

a few tumor cells can escape hypoxia-induced cell death by triggering adaptions in the proteome and genome, thus favoring tumor progression [27]. It has been reported that tumor hypoxia regulates the activities and/or expressions of proteins (although some protein subtypes are not sensitive to oxygen status) by signaling pathways with the latter being responsible for the catalysis of metabolic pathways (*e.g.*, hexokinase [HK], lactate dehydrogenase [LDH]), substance transport (*e.g.*, glucose transporter [GLUT], monocarboxylate transporter [MCT]), and transcription and stimulation factor (*e.g.*, hypoxia inducible factor [HIF] and vascular endothelial growth factor [VEGF]) [28-32].

Hypoxia has two types based on forming mechanisms: chronic (diffusion-limited) and acute (perfusion-limited) hypoxia. Chronic hypoxia, the long-term hypoxia (duration > 2 h), implies the perivascular regions surpassing the maximum oxygen diffusion distance due to the expansion of the intervascular space. Acute hypoxia, transient spatio-temporally (duration < 2 h), is caused by the temporary shut-down of flow (ischemic hypoxia) and/or severe reduction of oxygen content in tumor microvessels (hypoxemic hypoxia). The vascular oxygen content reduction mainly results from the transient plasma flow in tumor microvessels (temporal fluctuations in red blood cell flux) which limits the blood hemoglobin content. Therefore the oxygen supply is suppressed whereas other nutrient (*e.g.*, glucose) supply and waste (*e.g.*, lactate) removal are maintained in hypoxemic hypoxia [33], in contrast to the ischemic hypoxia which abolishes the nutrient supply and waste removal. Acute hypoxia has been reported with insignificant influence on the hypoxia imaging [34] and pathophysiological factors, such as HIF and GLUT1 [28, 33], whereas it is of importance on promoting the tumor malignancy and generating genomic instability as claimed in studies [32, 35]. These conflicting viewpoints motivate further investigation on acute hypoxia for the in-depth insights into its physiological functions.

The transcription factor HIF-1 is a key regulator for the induction of genes facilitating adaptation and survival of tumor cells and the whole organism from normoxia to hypoxia [36, 37]. It is exclusive with regards to oxygen availability and is stabilized by hypoxic conditions. More than 100 genes have been identified with the regulation of HIF-1 for a variety of tumor-adaptive functions, such as erythropoiesis/iron metabolism, angiogenesis, glucose metabolism, cell proliferation/survival and apoptosis. The HIF-1 related pathways have been linked to the embryonic development and pathophysiology of numerous human diseases (especially cancer and ischemic diseases). Immunohistochemical analyses have demonstrated the detectable levels of HIF-1α in benign tumors and elevated HIF-1α levels in malignant tumors, in contrast to its absence in normal tissue. The correlations between HIF-1 overexpression and patient mortality, poor prognosis or treatment resistance have been noted in many studies [38]. The many aspects

of HIF-1 regulation provide a variety of possibilities for therapeutic intervention. The cancer therapy may be effective by disrupting the HIF-1 pathways and functions.

The glucose metabolism in tumors is adapted toward glycolysis, even for normoxic cells, known as the 'Warburg effect' [39]. This genomic and proteomic adaptation is accompanied with enhanced rates of glucose consumption for energy purposes. Glycolysis, the metabolic pathway that converts glucose into pyruvate, has lower energy generation efficiency than aerobic respiration. Therefore the glycolysis rate is raised to compensate its inability to produce energy by increasing the expression and/or activities of related enzymes (*e.g.*, HK) and transporters (*e.g.*, GLUT). FDG, an analog of glucose, has been widely used for diagnosis, staging, and monitoring treatment of cancers, particularly in Hodgkin's disease, non-Hodgkin's lymphoma, colorectal cancer, breast cancer, melanoma, and lung cancer [40]. It has also been approved for use in diagnosing Alzheimer's disease [41]. FDG has similar transport and glycolysis kinetics to glucose, and competes with glucose for enzymes and transports during their uptake. Due to the tiny amount of FDG injected compared to glucose, the glucose uptake is not affected after the FDG injection. However FDG uptake depends on the glucose presence. After the phosphorylation of glycolysis, glucose and FDG are transformed into glucose-6-phosphate (to be further metabolized) and FDG-6-phosphate which is trapped in cells for radioisotope decay and cannot be further metabolized.

Lactate and proton, the product of glycolysis, is accumulated in tumors and is the major reason for tumor acidity. The accumulation of lactic acid has been proved to correlate with increased metastasis and poor disease-free and overall survival [42]. Lactic acid is dissociated in tumors into a lactate anion and a hydrogen cation. Although more studies of lactate focus on its production and contribution to tumor progression, metastasis and therapy, some tumor cells (*e.g.*, cervical cancer SiHa cells [43] and breast cancer MDA-MB-231 cells [44]) have been demonstrated to utilize lactate for energy purposes (lactate oxidation), decreasing tumor acidity in the presence of oxygen. Lactate oxidation requires (i) membrane-bound MCTs for lactate movement; (ii) LDH for lactate converting to pyruvate before it can enter into the tricarboxylic acid (TCA) cycle; (iii) adequate concentration of oxygen (lactate cannot be consumed anaerobically); (iv) healthy and functional mitochondria required for TCA cycle and electron transport chain (ETC). Lactate production and utilization can occur simultaneously and/or shift from net lactate production to net lactate uptake based on the external lactate concentrations and facilitated by lactate transporters: MCTs.

MCT4, which has low lactate affinity, is responsible for lactate export in the hypoxic region. The extracellular lactate accumulated shuttles toward the normoxic region due to the concentration difference. In the normoxic region, the lactate is imported by MCT1, which has high affinity of

lactate. In the oxygenated cell, the lactate is converted into pyruvate with the catalyzation of LDH and then enters the TCA cycle. Although the lactate is proven with positive correlation with tumor progression and metastasis [45, 46], the evidence that lactate utilization (reduced lactate accumulation) lessens the negative effect of a hostile tumor microenvironment is not clear to date. Lactates are transported across the cell membrane in association with protons [47] (*i.e.* co-transport). The mechanism of lactate co-transport involves rapid-equilibrium lactate and proton binding, with the proton binding first (ordered-binding), and the lactate may bind only to the transporter in the proton-bound state. Only the fully unbound carrier or the fully bound carrier can undergo a conformational change associated with transport of substrates across the membrane.

Tumor metabolism consists of complex interactions between oxygenation states, metabolites, ions, the vascular network and signaling cascades [42]. Since our study mainly focuses on the glucose and lactate metabolism and related metabolites, the mechanisms of the metabolism of other substances are not introduced here.

1.3. Imaging positron labeled tracer

1.3.1. Properties of positron

Positrons originate from the natural radioactive decay. The proton-rich radioactive atom *X* (such as ^{11}C, ^{13}N, ^{15}O, ^{18}F and ^{68}Ga) achieves stability by emitting a positron, converting a proton to a neutron (v) and producing the daughter nucleus Y, whose atom number is one less than the parent. The general equation for positron decay from an atom is:

$$ {}^{A}_{Z}\mathrm{X} \rightarrow {}^{A}_{Z_{-1}}\mathrm{Y} + {}^{0}_{1}\beta^{+} + \nu + \mathrm{Q}\left(+\mathrm{e}^{-}\right) $$

where A and Z are the mass number and the atom number respectively. Since the atom number of the daughter nucleus is less than the parent, one of the orbital electrons is ejected from the atom to balance charge. The electron overcomes the binding energy by supplied energy from the nucleus and leaves the atom with residual kinetic energy, represented by Q in the above equation.

The rate of the decay is characterized by the parameter called the half-life of the radionuclide ($T_{0.5}$). The half-life is the time it takes for half of the unstable nuclei present to decay. The radioactivity A_t of the radionuclide after a time t is given by:

$$ A_t = A_0 * 2^{-t/T_{0.5}} \tag{1.1} $$

where A_0 is the original activity at the time 0. As examples, the half-lives of ^{11}C, ^{13}N, ^{15}O, ^{18}F and ^{68}Ga are 20.4, 9.96, 2.03, 109.8 and 68.3 mins, respectively. The half-life determines the applicability of the tracer. Overly short half-life limits the clinical and preclinical applications of the tracers, whereas the longer half-life introduces additional risks on the possible nuclear contamination due to the improper treatment and utilization procedures.

The positron will have an initial energy after emission, which can take a continuum of values up to a maximum E_{max}. The E_{max} for ^{11}C, ^{13}N, ^{15}O, ^{18}F and ^{68}Ga are 0.959, 1.197, 1.738, 0.633 and 1.898 MeV, respectively. With given E_{max}, the theoretical energy spectrum of a nuclide can be simulated by [48, 49]:

$$N(E)dE = \mathrm{W}pF(Z,W)(E_{max} - E)^2 \tag{1.2}$$

Where $N(E)$ is the probability of a positron at energy E (keV), W=1+E/511, p is the momentum of the positron:

$$p = \sqrt{W^2 - 1} \tag{1.3}$$

$$F(Z,W) = \frac{2\pi\eta}{1-e^{-2\pi\eta}} \tag{1.4}$$

$$\eta = -ZW/137p \tag{1.5}$$

The examples of simulated energy spectrum of several nuclides are shown in Figure 1.1.

After emission from the nucleus, the positron loses kinetic energy by interactions with the surrounding matter. The positron interacts with the other nuclei by one of four types of interactions [16]: (i) inelastic collisions with atomic electrons; (ii) elastic scattering with atomic electrons; (iii) inelastic scattering with a nucleus; and (iv) elastic scattering with a nucleus. The positron energy loss is mainly attributed to the first type of interaction. And the third type of interaction often corresponds with Bremsstrahlung radiation. The scattering and collisions induce a deflection in the positron path and the positron has an extremely tortuous passage through matter. A positron loss its energy by inelastic scattering until it has zero kinetic energy and then combines with an electron (the annihilation). The ranges of positrons in the water (the main component of tissue) before annihilation are usually below 20 mm [16]. The annihilation of the positron and electron gives off electromagnetic radiation. The most probable form is the radiation of two photons of 511 keV, which are emitted at 180° to each other. The photons are emitted in opposite directions to conserve momentum. However in many cases, the photon pairs are not emitted strictly at 180° due to non-zero momentum when the positron and electron annihilate.

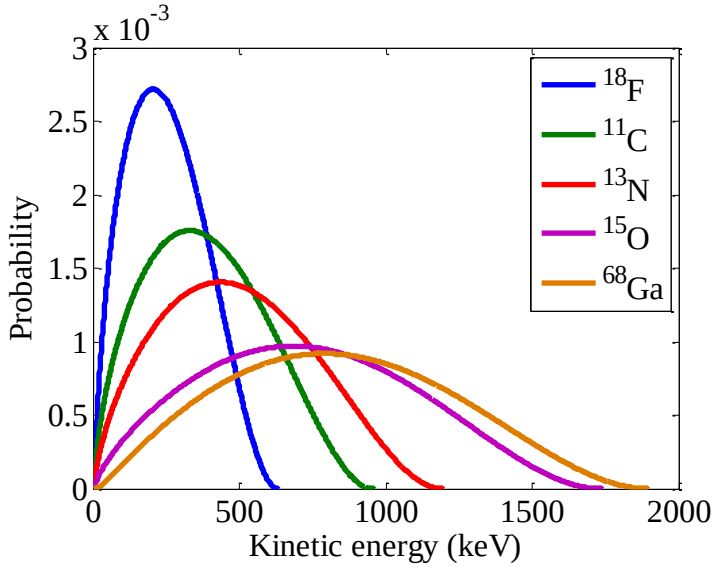

Figure 1.1. Examples of simulated energy spectra of some nuclides

The photon pair interacts with the atoms in an absorbing material by (i) the photoelectric effect; (ii) the Compton effect; (iii) pair production, depending on the energy of the electromagnetic energy (the photon energy). These interactions lead to ionization of the atom and liberation of excited electrons by the transfer of energy in the interaction. The radiation detectors are developed based on the interaction of ionizing radiation with matter. The radiation detector converts the deposited energy into a measurable electrical signal or charge. There are three broad categories of radiation detector: proportional chambers, semi-conductor detectors and scintillation detectors. Among them, the scintillation detector is most widely used for the detection of 511keV photons in PET. It typically consists of a scintillator (an inorganic crystal) emitting visible light photons after the interaction of photons within the detector. A photon detector (photo-multiplier tubes (PMTs) or semiconductor based photodiodes) is connected to the scintillator to measure the number of scintillation photons.

1.3.2. PET imaging

PET is a functional imaging technique the produces a three dimensional (3D) image of functional processes of radioactive tracer accumulation in the body. The system detects the gamma pairs coming from the positron-electron annihilation. The positron is emitted directly from a positron emitting radionuclide. A tracer is labeled with the radionuclide as the probe of PET imaging. The tracer is normally an analogy of the substance that is necessary for metabolism, *e.g.*,

[18F]fludeoxyglucose ([^{18}F]FDG), the radioactive analog of glucose, [18F]fluorothymidine ([^{18}F]FLT) [50], the analog of nucleoside thymidine.

A PET scanner counts coincident events between pairs of detectors [16, 51]. The straight line connecting the centers of two detectors is a "line of response (LOR)". Unscattered photon pairs recorded for a specific LOR arise from annihilation events located within a thin volume centered around the LOR, which is referred as a "tube of response". Among registered events (events meeting the detection criteria), there are also unwanted events due to photon scattering or accidental detection of two photons from unrelated positron annihilations. These interruptions are corrected in PET image analysis.

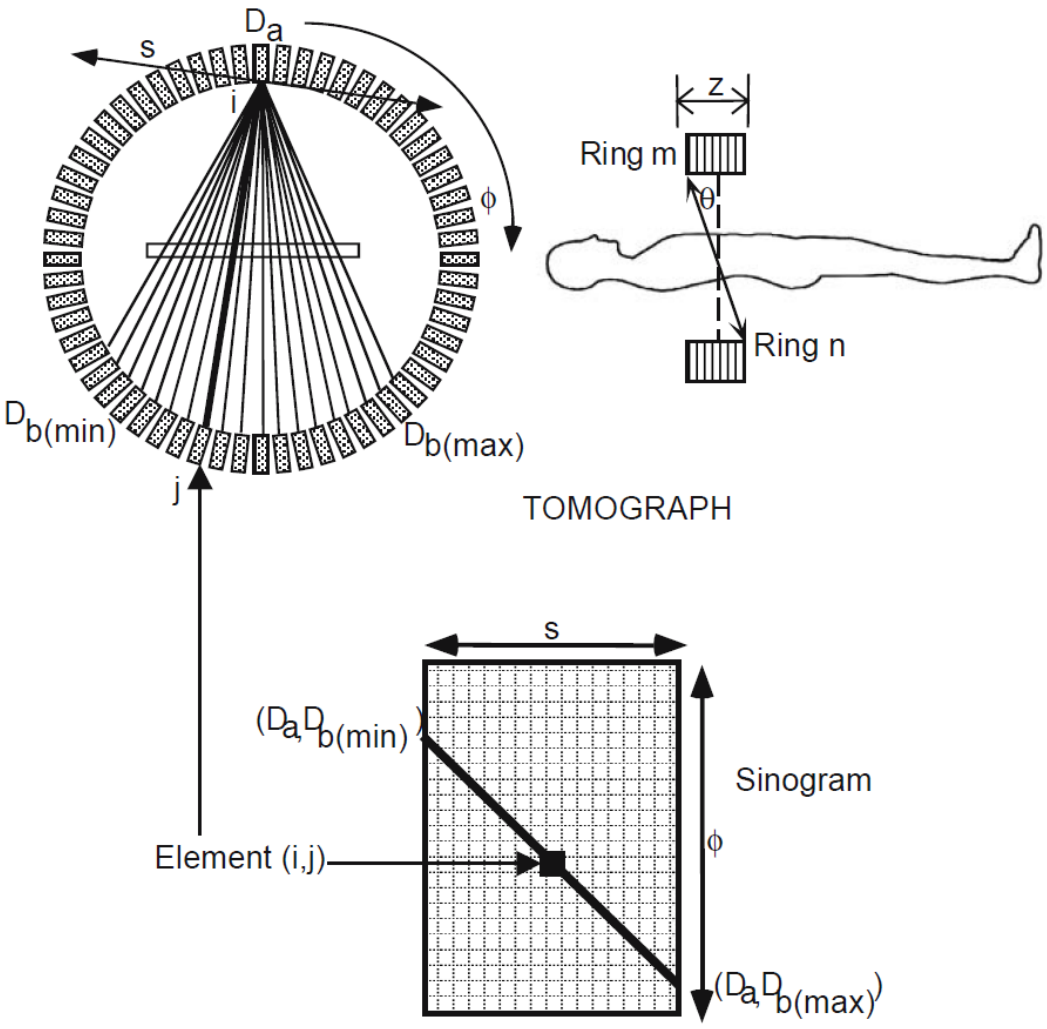

Figure 1.2.The mapping from sampling projections to sinograms [16].

In PET imaging, the natural parameterization of PET data uses the indices (D_a, D_b) of the two detectors in coincidence. This parameterization method has the following disadvantages: (1) it is poorly adapted to analytic algorithms and (2) recorded coincidences in a given scan may be too small to take full advantage of the nominal spatial resolution of the scanner. To overcome these, individual detector elements from coincidence pairs with opposing detectors are mapped to the sinogram (2D) or Michelogram space (3D), as shown in Figure 1.2. In the 2D case, the radial variable s (signed distance between the LOR and the center of the detector ring) and angular variable ϕ (the orientation of the LOR) are used to parameterize a LOR with respect to a Cartesian coordinates system (the polar angles $\theta = 0^{\circ}$). In the 3D case, this is extended to measuring projections at polar angles $\theta > 0^{\circ}$. Therefore, the sinograms/Michelograms formed in PET are composed of projection $p(s, \phi, \theta, z)$.

With the sinogram, three sets of data are required for the image reconstruction: (1) the emission scan which is to be reconstructed; (2) a set of normalization sinograms (one per plane in 2D) to correct for differential detector efficiencies and geometric effects related to the ring detector, or a series of individual components from which such a normalization can be constructed; (3) a set of sinograms of attenuation correction factors to correct for photon attenuation (self-absorption or scattering) by the object. The general PET image reconstruction procedure starts with applying the correction for random coincidences and x-ray transform on measured data to obtain the sinograms. The sinograms are then corrected for attenuation and normalized for different crystal efficiencies. Next, the corrected sinograms are reconstructed using analytic or iterative algorithm to reconstruct the image (the image reconstruction process is illustrated in section 2.3). The filtered back projection is a typical algorithm used for PET image analytic reconstruction. The iterative algorithms (such as maximum-likelihood expectation maximization and ordered subset expectation maximization algorithms) are developed to overcome the drawbacks of analytic algorithms for the image reconstruction. During the final step, scalar corrections for dead time and decay may also be applied.

Clinical PET imaging is being used in the areas of cancer diagnosis and management, cardiology and cardiac surgery, and neurology and psychiatry [16]. In clinical oncology, due to enhanced activities and/or expressions of GLUT (facilitating glucose transport) and HK (catalyzing phosphorylation), more FDG will be trapped in hypoxic regions until it decays. It results in intense radiolabeling of tissues with high glucose uptake, such as brain, liver and most cancers, Therefore, FDG PET can be used for diagnosis, staging and monitoring treatment of cancers, in particular in Hodgkin's lymphoma, non-Hodgkin's lymphoma and lung cancer. A few other isotopes and radiotracers are also introduced into oncology for specific purposes, such as 11C-

Metomidate PET for detecting tumors of adrenocortical origin[52, 53], 3,4-dihydroxy-6-18F-fluoro-L-phenylalanine (18F-FDOPA) PET for finding and localizing pheochromocytoma [54].

PET neuroimaging is based on an assumption that areas of high radioactivity are associated with brain activity. Using [^{15}O]H_2O PET, the flow of blood to different parts of the brain is measured indirectly. FDG PET can also be utilized for neuroimaging since the brain is normally a rapid user of glucose and brain pathologies such as Alzheimer's disease greatly decrease brain metabolism of both glucose and oxygen [55]. Therefore, FDG PET has the potential to differentiate and diagnose Alzheimer's disease early. Several other radiotracers have been developed for PET that are ligands for specific neuroreceptor subtypes [^{11}C]raclopride [56], [^{18}F]fallypride [57] and [^{18}F]desmethoxyfallypride [58] for dopamine D2/D3 receptors, [^{11}C]McN 5652 [59] and [^{11}C]DASB [60] for serotonin transporters, [^{18}F]Mefway for serotonin 5HT1A receptors [60], [^{18}F]Nifene for nicotinic acetylcholine receptors or enzyme substrates (*e.g.*, 6-FDOPA for the AADC enzyme) [60]. These agents permit the visualization of neuroreceptor pools in the context of a plurality of neuropsychiatric and neurologic illnesses. PET has also been applied in the studies on neuropsychology, psychiatry and stereotactic surgery (treatment of intracranial tumors, arteriovenous malformations and other surgically treatable conditions).

Cardiology, atherosclerosis and vascular disease are also studied by PET. FDG PET imaging of atherosclerosis detects patients at risk of stroke and can help test the efficacy of novel anti-atherosclerosis therapies [61]. In addition, PET is a feasible technique for studying skeletal muscles [62]. The muscle activation data about deeper lying muscles such as the vastus intermedialis and the gluteus minimus can be captured by PET imaging.

1.3.3. Direct positron imaging

Compared with PET imaging which detects the 511 keV photons from the annihilation of electron-positron pairs, beta imaging involves the direct exposure of the detector to the irradiation of beta particles (*i. e.*, electrons and positrons) emitted from the radionuclides. As a newly emerging modality, beta imaging provides higher spatial resolution and sensitivity compared with other imaging modalities and therefore enables the functional imaging of delicate biological structures in *in-vitro* and *in-vivo* experiments. The spatial resolution of beta imaging is largely determined by the beta particles, and the materials of imaging samples and beta detectors. As beta particles are multiple-scattered when traversing the beta detector, (*i.e.*, the partial volume effect), the spatial resolution of beta imaging is limited in particular for high energy beta particles with oblique incident angles. The spatial resolution has been improved by energy

weighted centroid approximation [63] or classification algorithm (searching the primary incident sites of particles in the 2D imaging plane of beta detector as explained in Section 4.2).

The beta camera has been applied in some clinical and preclinical applications including intraoperative navigation, microfluidic radioassay, digital autoradiography, and radioluminescence microscopy [18-20, 64, 65]. These applications are based on several important imaging technologies, such as charged-coupled device (CCD), complementary metal-oxide semiconductor (CMOS) and position sensitive avalanche photodiode (PSAPD). The applications of a CCD for beta imaging under direct irradiation [66-69] and indirect irradiation via a scintillation sheet [64, 65, 69, 70] have been reported, such as β-imager coupled with a parallel plate avalanche chamber [71], μ-imager integrated with a scintillator sheet [69], and radioluminescence microscopy fitted with a scintillator plate and microscope offering a high resolution on single cell level [64, 65]. Position sensitive CMOS detectors have also been used in beta imaging, such as the series of Medipix chips: Medipix 1, 2 and 3 (including Timepix), which was developed by the CERN Medipix collaboration. Several applications of Medipix and Timepix chips under the irradiation of beta particles using various radioactive sources (^{3}H, ^{14}C, ^{18}F, ^{32}P, *etc*.) have been presented [63, 72-77].

As a powerful tool monitoring tumor metabolism, the beta camera has been coupled to the microfluidic chip for imaging the process of [^{18}F]FDG uptake on small cell population or single cell level [18]. The microfluidic radioassay can provide a platform for integrated and digital control of small volumes of reagents suitable for bioassays of small cell populations. Although many techniques are available for measuring biochemical functions in microfluidic systems, the use of radiometric methods can provide high sensitivity for small amounts of radiotracers. The microfluidic radioassay platform for measuring cellular [^{18}F]FDG uptake can complement conventional clinical techniques, such as FDG PET, and enable monitoring of glycolysis in response to novel clinical therapies [18]. Vu, et al. has developed an integrated beta-camera and microfluidic chip for quantitative imaging of glycolysis radioassays using [^{18}F]FDG. This system is demonstrated to have the abilities of digital control and quantitative measurements of glycolysis of melanoma cell lines. Nevertheless, their measurement is not dynamic, which means the FDG uptake is only measured at certain points in time. To confront this drawback, our group has developed a novel system integrating a beta camera, a microfluidic chip and other accessories (such as a digital pump) to realize the real time FDG uptake monitoring.

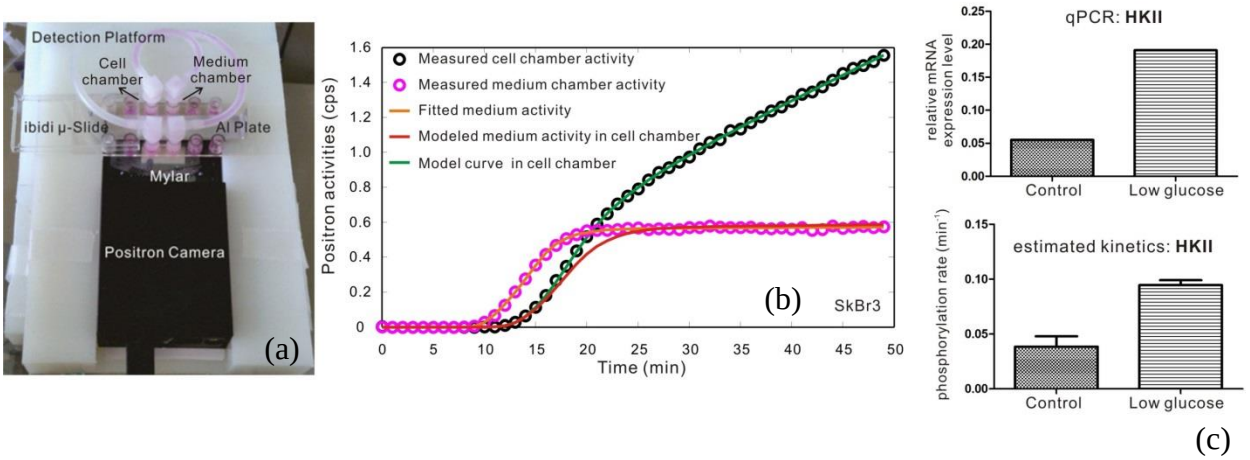

Figure 1.3. (a) *The platform of positron imaging of [^{18}F]FDG uptake by SkBr3 cells.* The dual chamber protocol (one cell chamber and the other medium chamber) is applied. The tracer is loaded firstly to the medium chamber and then the cell chamber. (b) *The measured cell and medium chamber activities and their fitted activities.* The medium chamber activity curve is corrected with delay and dispersion to obtain the modeled medium activity in the cell chamber. (c) *An application of the dynamic positron imaging of FDG uptake (the difference of measured cell chamber activity and medium activity in cell chamber) on estimating protein kinetics.* The phosphorylation rate catalyzed by HKII is estimated higher for cells treated with low glucose compared with that in the control (cells without low glucose treatment). This result is verified by comparing with the relative mRNA expression levels of the two conditions (low glucose and control). Images and data courtesy of Dr. Kuangyu Shi and Zhen Liu, Technical University Munich.

Our tumor metabolism positron imaging platform is shown in Figure 1.3(a), where the signals indicating the FDG uptake process by the human breast cancer cell SkBr3 are captured in real time. The dual chamber protocol (one cell chamber and the other medium chamber) is utilized. In the measurement, the tracer is loaded first to the medium chamber and then flows through the cell chamber. The activities in both chambers are measured simultaneously and plotted in Figure 1.3(b). To obtain the modeled (corrected) medium activity in cell chamber, the measured medium chamber activity is corrected taking into consideration of the tracer flow delay and dispersion caused by tube connection between the two chambers. The modeled medium activity in the cell chamber serves as the FDG input of the cell chamber. Therefore, the dynamic FDG uptake is acquired by deducting the modeled medium activity in the cell chamber from the total activity in the cell chamber.

With the dynamic FDG uptake curve and the two-tissue compartment model, the kinetic

parameters of the enzymes or transporters involved in the FDG uptake occurring within this imaging system can be estimated. As exhibited in Figure 1.3(c), the phosphorylation rate (determined by hexokinase II [HKII], the catalyst of phosphorylation in the glycolysis) of SkBr3 cells incubated in low glucose conditions is estimated higher than that in the control. This phenomenon is attributed to the overexpression of HKII under low glucose conditions, which has been verified using quantitative real-time polymerase chain reaction (qPCR). The relative mRNA expression levels (measured by qPCR) of the cells treated with low and normal glucose are compared as displayed in Figure 1.3(c). The result from the qPCR is consistent with that from the kinetics estimation by microfluidic chip protocol.

As for *in-vivo* application of positron imaging, a window chamber protocol is put forward as illustrated in Figure 1.4. The rat is implanted a window chamber which facilitates the direct contact of solid tumor with the positron camera in the measurement. The rat is immobilized in case of image disturbance by rat movement. The tumor metabolism within the window can be monitored in real time using this system.

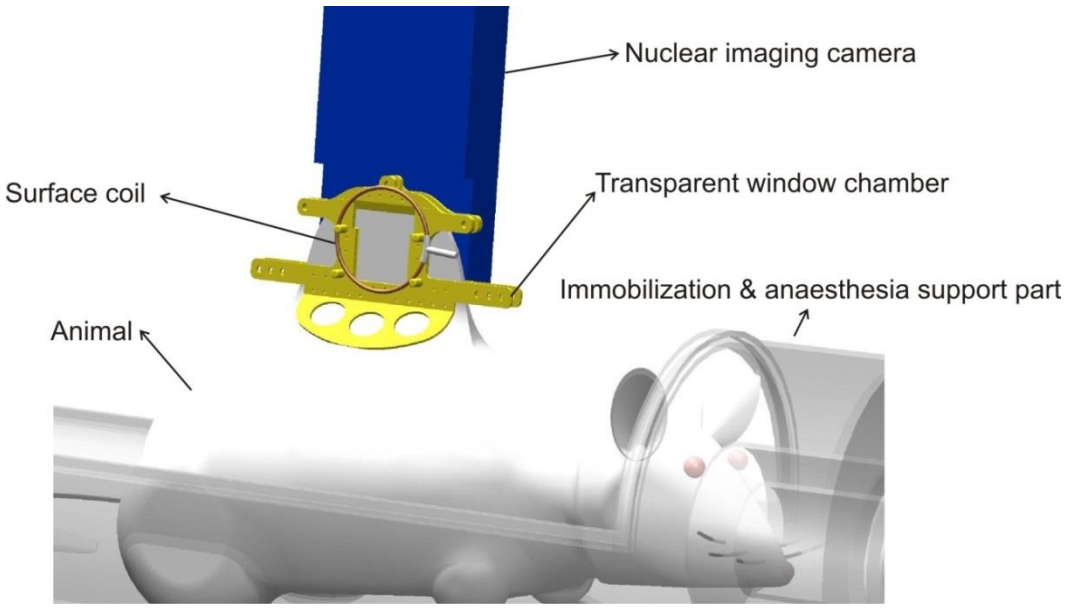

Figure 1.4. The sketch of window chamber protocol for *in-vivo* application of positron imaging

1.4. Thesis outline

Positron imaging has been used for monitoring tumor cellular metabolic processes. To capture high resolution positron images of tumor metabolisms, the in-depth understanding of the formation mechanisms of signals originated from the positron-emission tracers that are

accumulated in solid tumors is necessary. In general, the positron signals are formed by two steps. First, the positron-emitting probe is injected and accumulated more in the tumor regions due to its specific interactions with tumor microenvironment. Secondly, the positrons emitted from solid tumors are captured by a detector. For systematic and deep understanding of signal mechanisms and high resolution positron imaging, the computational modeling is introduced in this thesis to simulate the tumor metabolic processes and improve the spatial resolution of positron imaging. The thesis is organized in 7 chapters to have clear illustrations of the computational modeling methods and their applications.

This chapter gives an overview of molecular imaging, tumor physiology, and principles and applications of PET and direct positron imaging. It is a background knowledge preparation for the introduction of computational modeling.

Chapter 2 constructs a theoretical basis. The general computational methods supporting the molecular imaging of tumor metabolisms are presented: (1) the simulation methods to generate the tumor microenvironment (including the formation and angiogenesis of tumor vasculature, the spatio-temporal evolvement of substances, the cellular metabolism and substrate transport); (2) the machine learning models and algorithms (classification and regression) for image quality improvement; (3) the algorithms for image reconstruction (ML-EM and OSEM algorithms); (4) the pharmacokinetic modeling (one and two tissue compartment and Patlak models) and data analysis methods for metabolic parameter (such as the rates of FDG uptake and phosphorylation) estimation.

In Chapter 3, pathophysiological models describing the key metabolic pathways (mediated by enzymes and transporters) and substrate interactions in solid tumors are constructed and the modeling methods (parameter selection, boundary conditions, etc.) are illustrated. Several metabolites (*e.g.*, oxygen, glucose, lactate, protons, bicarbonate ions), transporters (GLUT, MCT1 and MCT4), a key enzyme (HK), and a key transcriptional factor (HIF-1) are integrated into the models. The glucose and lactate metabolic pathways are the major pathways investigated. The quantitative relationship between the tumor phenotypes (*i.e.*, pathophysiological factors, characterized by expressions of transporters, enzyme, transcriptional factor and vasculature) and metabolism of substrates or probe (glucose, lactic acid and FDG) are explored and parameterized (analytic parameters are proposed to characterize the relationship).

Chapter 4 puts forward the methods for positron camera characterization and spatial resolution improvement for ^{18}F positron imaging. The characterization methods (for evaluating spatial resolution, sensitivity, linearity and background) and Monte-Carlo simulations as theoretical predictions of measurements are introduced. To reduce the effect of multiple scattering on the

imaging with positron camera and improve the spatial resolution, a novel data-driven method is proposed based on the classification of primary pixels fired by positrons within the silicon detector (Timepix detector) using support vector machine.

The computational models describing tumor metabolisms are validated and applied in Chapter 5. The proposed models are verified by comparing the simulation results with *in vivo* and *in vitro* literature data. The multiple influences of different pathophysiological factors on substrate concentrations (characterizing the metabolism), and the quantitative relationship between tumor phenotypes and metabolisms are evaluated by analyzing the proposed analytic parameters. We compare the simulation results brought from the relationship analysis with the experimental observations.

Chapter 6 applies the classification algorithm (proposed in chapter 4) on the ^{18}F positron imaging using an absorbing edge protocol and a leaf sample to assess its ability on spatial resolution enhancement. The measured characteristics of positron imaging are evaluated and compared with the predictions from Monte-Carlo simulation.

Chapter 7 summarizes the contributions of the modelling methods proposed in this thesis.

2. Computational methods for molecular imaging of tumor metabolism

Computational modeling and methods are widely involved in the molecular imaging procedures. They are useful tools assisting the interpretation of the formation mechanisms behind the measured signals and images. Four types of computation modeling, which support molecular imaging of tumor metabolisms, are introduced in this chapter. *Principle-driven modeling* simulates tumor metabolic pathways and establishes the quantitative relationship between the tumor metabolisms and tumor phenotypes. The principles of modeling vasculature angiogenesis, enzyme and transport kinetics, and ion interactions are explained. *Data-driven modeling* exploits machine learning algorithms (such as classification and regression algorithms) for molecular imaging analysis. This modeling may contribute to the enhancement of disease identification and prediction accuracy. *Scanner modeling* facilitates the image reconstruction, which is an indispensable step for molecular imaging. *Pharmacokinetic modeling* is used for the functional imaging and quantitative analysis of substrate kinetic distributions, and the evaluation and prediction of relevant protein expressions and activities in solid tumors. It provides a potential for substantial broadening the information that can be extracted from the measurements using PET or positron detector.

2.1. Simulation methods for modeling tumor metabolism

Due to our advanced understanding of tumor physiology and computational technology, theoretical simulation has been developed as a complementary method for the optimization of cancer diagnosis and therapy. This method has been applied to model the complicated tumor microenvironment (TME) with multiple features and interactions [78]. Casciari *et al*. have developed a mathematical model to predict the TME and growth in EMT6/Ro multicellular tumor spheroids [79]. The concentration distributions of oxygen (O_2), glucose, lactate, hydrogen ions (H^+), carbon dioxide (CO_2), bicarbonate ions (HCO_3^-) and chloride ions (Cl^-) along the spheroid radial direction and their effects on cell growth and metabolism were predicted by solving reaction-diffusion equations. The mathematical model was then developed by Molavian *et al.* in one dimension to explain the tumor interstitial oxygen tension (pO_2) and pH distributions as a function of distance from a single blood vessel and tumor cell glucose metabolic pathways [80]. They semi-quantitatively derived the experimental results of Helmlinger *et al.* on pO_2 and pH distributions [81]. Dașu *et al.* presented a 2D computational model to simulate tumor oxygenation, as well as a method to emulate the effects of diffusion-limited hypoxia and perfusion-limited hypoxia [82]. Based on this, Kelly and Brady put forward a model to simulate the spatio-temporal distribution of the hypoxia-specific tracer [^{18}F]fluoromisonidazole ([^{18}F]Fmiso) in tumors and generated meaningful dynamic time activity curves (TACs) for [^{18}F]Fmiso [83]. Dalah *et al.* thereafter extended Kelly's work to simulate the TACs of the radioactive tracer [^{64}Cu]-diacetyl-bis(N^4-methylthiosemicarbazone) (Cu-ATSM) and demonstrated its potential role in tumor sub-volume delineation for radiotherapy treatment planning [84]. Petit *et al*. theoretically investigated the influence of intra-voxel heterogeneity on optimal dose prescription in radiotherapy by modeling the oxygenation and dose distributions [85]. Moennich *et al.* simulated the [^{18}F]Fmiso dynamics based on histology-derived microvessel maps and the influence of acute and chronic hypoxia on [^{18}F]Fmiso PET imaging [34, 86]. The simulation methods for constructing mathematical models of tumor metabolism are illustrated as follows.

2.1.1. Tumor microvasculature formation and angiogenesis

The vasculature is the basis to sustain the tumor metabolism by supplying the tissue with oxygen and nutrients and deporting the waste. The formation and angiogenesis of tumor vasculature have been modeled mathematically in 2D or 3D manner. In many cases, the tumor vasculature is built by probabilistic methods with consideration of its geometrical features (*e.g.*, microvessel diameters and intervessel distances) [82-85]. The ranges of these parameters (geometrical

features) were found by fitting experimental data [23, 24]. The microvessel distributions were usually characterized by mean values and coefficients of variations (CV or relative standard deviation) [82]. For a 2D simulation, fixed or (normal-) distributed microvessel diameters are assumed within the ranges reported by the literature [23, 24]. The tumor microvessels are assumed orthogonal to the modeling plane. Although it is reported that vascular perpendicularity may lead to an underestimation in pO_2 [83], realistic pO_2 simulation under the vascular perpendicularity assumption has been achieved with flow limited assumption (without the projection of 3D microvessels) [82]. As microvessel orientations are randomly distributed in reality, some studies have integrated this effect in the framework of 2D simulations. The 3D vasculature was projected on the modeling plane to form a 2D vascular map and the branching angles (characterizing microvessel orientations) have been introduced by convoluting the orientation operator (cosine) to the 2D vascular map [83]. Another method of vasculature simulation is based on the histology-derived vessel structural map [34, 86]. The microvessels, extracted from the digital image of immunohistochemically stained tumor sections, are approximated parallel with the modeling plane.

Mathematical modeling of vascular angiogenesis has been reported [25, 35, 87]. The tumors exceeding some critical diameter ($\approx$2 mm) lack of nutrients and oxygen and therefore become hypoxic. The hypoxia is assumed to trigger cellular release of tumor angiogenic factors. The simulation of angiogenesis process normally starts with the cellular release of tumor angiogenic factors. Then they diffuse into the surrounding tissue to activate the endothelial cells of nearby blood vessels. In response to angiogenic factor, the endothelial cells sprout, migrate and proliferate toward the tumor, forming the tumor vasculature. The proliferation and migration of endothelial cells in response to different signaling cues are considered in the models. Mathematical models of tumor-induced angiogenesis fall into three major categories [87]: (i) continuum models that treat the endothelial cells density and chemical species as continuous variables that evolve according to a reaction-diffusion system, (ii) mechanochemical models that incorporate some of the mechanical effects of endothelial cell and extracellular interaction on cell motion, in addition to the diffusible chemical species, (iii) discrete, cell-based models in which cells are treated as units and move, grow and divide according to prescribed rules. A typical continuum model can be formulated as follows:

$$\frac{\partial n}{\partial t} = -\nabla \cdot \vec{J} + f(n, c) \tag{2.1}$$

$$\frac{\partial c}{\partial t} = D\nabla^2 c + g(n, c) \tag{2.2}$$

Where $n(x, t)$ is a vector comprised of the densities of all cell types involved in the process (*e.g.*,

endothelial cells, pericytes, *etc.*). $c(x,t)$ is a vector containing the concentrations of substances influencing migration and/or proliferation, such as, protease enzymes, fibronectin and angiogenic inhibitor. $\vec{J}$ is the flux of endothelial cells, which comprises a random diffusive component and a set of tactic components, and can be written in the form:

$$\vec{J} = -D_n \nabla n + \sum_i \chi_i(c) n \nabla c_i \tag{2.3}$$

The chemicals responsible for these tactic components of the flux could be tumor angiogenesis factor, fibronectin, *etc.* $\chi_i(c)$ is the tactic sensitivity of endothelial cells in response to a gradient of the *i*th tactic component. It is usually assumed that $\chi_i(c)$ depends only on the concentration of the corresponding tactic chemical. The function $f(n,c)$ combines the effects of cell proliferation and apoptosis, while $g(n,c)$ is a vector function describing the dynamics of production, uptake and degradation of the chemical components included in the model. *D* is a diagonal matrix containing the diffusivities of each chemical species.

The simplest boundary conditions are no-flux condition for the endothelial cell density and Dirichlet boundary conditions for the chemicals:

$$J = 0 \quad \text{and} \quad c = c_0(t) \tag{2.4}$$

The continuum models have been developed to describe both the onset of angiogenesis and the later stages of the angiogenic process, whereas, it cannot predict the vascular structures. In order to predict the vascular structures, the discrete models are proposed. It treats sprouts individually and tracks the motion of the tip of a growing sprout, which is characterized by the position and velocity of the tip cell. The evolution of the tip velocity (for the *i*th sprout) is governed by a stochastic differential equation:

$$dv_i = -\beta v_i(t)dt + \sqrt{\alpha} dW_i(t) + \kappa \nabla a \sin\left|\frac{\Phi_i}{2}\right| dt \tag{2.5}$$

This equation comprises a viscous damping term, a white noise term to model random motion and a chemotactic component. β is a viscosity coefficient, W is the Wiener process, a white noise process, κ is the chemotactic responsiveness, a is the tumor angiogenesis factor concentration. Φ is the angle between the direction the tip is moving and that towards the tumor angiogenesis factor source. The tip position x_i is determined by the following equation:

$$\frac{dx_i(t)}{dt} = v_i(t) \tag{2.6}$$

Finally, the equation for the average density satisfies:

$$\frac{\mathrm{d}\rho_i(t)}{\mathrm{dt}} = k_g \frac{\rho_{max}-\rho_i(t)}{\rho_{max}-\rho_{min}}\rho_i(t) - \frac{s_i(t)}{L_i(t)}\rho_i(t) + k_b\left[\rho_p(t) - \rho_i(t)\right] - \sum_{j=1}^{\nu_i} k_b\left[\rho_i(t) - \rho_j(t)\right] \quad (2.7)$$

where k_g is the proliferation rate, k_b is the redistribution coefficient, $\rho_p(t)$ represents the parent vessel density, ν_i is the number of branches that the *i*th sprout has at time *t*, s_i is the instantaneous speed of the *i*th sprout calculated as $s_i(t) = \|v_i\|$ and L_i is the sprout length calculated from

$$\frac{dL_i(t)}{dt} = s_i(t) \quad (2.8)$$

At each time step these three ordinary differential equations (ODEs) are solved for each sprout. The total number of sprouts changes due to branching (birth) and anastomosis (death of sprouts).

The above models do not consider blood flow. However, since the shear stresses generated within the capillary network by the flowing blood strongly influence vessel adaptation and network remodeling, the flow of blood as a non-Newtonian fluid in an adaptive dynamic capillary network is therefore considered in the recent new work [25, 35]. Due to the complexity of modeling angiogenesis with blood flow effect, it is not explained here.

2.1.2. Spatio-temporal evolution of substrates in tumors

The spatial-temporal evolvements of species in tumor interstitial space (in tumor tissue) satisfy reaction–diffusion equations. The reaction-diffusion equations for ions are different from those for neutral species, since the electric potentials caused by other ions in the system need to be considered. In tumor interstitial fluid, considering the migration, diffusion and convection, the molar flux of the component *s*: $\overrightarrow{N_s}$ (the flux density quantity) is expressed in terms of the concentration $[s]$ gradient [88]:

$$\overrightarrow{N_s} = -z_s u_s \mathrm{F}[s]\nabla\varphi - D_s\nabla[s] + [s]\vec{v} \quad (2.9)$$

$\overrightarrow{N_s}$ indicates the direction in which the species is moving and the number of moles going per unit time acorss a unit plane, oriented perpendicular to the flow of the species. z_s is the charge, u_s is the mobility, F is Faraday's constant, φ is the electrical potential, and D_s denotes the diagonal diffusion coefficient matrix. $\vec{v}$ is the bulk velocity of the species. The region of interest is assumed to be isotropix and uniform, where the substance diffusivities are represented by a scalar matrix, independent on coordinates. In the tissue (outside the blood vessels), there are no significant currents, so the convection term can be neglected. The movement of the species can deviate from this average velocity by diffusion if there is a concentration gradient $\nabla[s]$, or by migration if there is an

electric field $\nabla\varphi$ and if the species is charged. For neutral species, *e.g.*, oxygen, glucose and CO_2, the first term of above equation is zero. Whereas, the ions (*e.g.*, H^+, HCO_3^-) expose to the eletric fields generated by other ions within the system and therefore the first term is non-zero.

Based on the Einstein-Nernst equation and zero total charge fluxes, the flux of a species can be rewritten as

$$\overrightarrow{N_s} = -D_s\nabla[s] + z_s D_s[s](\sum_{k=1}^{n} z_k D_k \nabla[k])/(\sum_{k=1}^{n} z_k^2 D_k[k]) \tag{2.10}$$

where index *k* covers all the charged species. The second term of the above equation is zero for neutral species.

Now the flux expressions can be used in the reaction-diffusion equation. The reaction-diffusion equation for component *s* is as follows:

$$\frac{\partial[s]}{\partial t} = -\nabla \cdot \overrightarrow{N_s} + P_s \tag{2.11}$$

After substituting equation (2.9) into equation (2.10), the final reaction-diffusion equation is obtained:

$$\frac{\partial[s]}{\partial t} = D_s\nabla^2[s] - z_s\nabla[s] \cdot \frac{\vec{C}}{\vec{B}} - \frac{z_s[s](AB - \vec{C}\cdot\vec{D})}{B^2} + P_s \tag{2.12}$$

$$A = \sum_{k=1}^{n} z_k D_k \nabla^2[k] \tag{2.13}$$

$$B = \sum_{k=1}^{n} z_k^2 D_k[k] \tag{2.14}$$

$$\vec{C} = \sum_{k=1}^{n} z_k D_k \nabla[k] \tag{2.15}$$

$$\vec{D} = \sum_{k=1}^{n} z_k^2 D_k \nabla[k] \tag{2.16}$$

where, P_s is the metabolic rate of species *s*. For neutral species, the distributions are not affected by electric potentials (*i. e.*, the 2nd and 3rd term on the right of equation (2.11) are zero).

2.1.3. Substrate cellular metabolism

The substrate cellular metabolism in tumors can be reflected by Michaelis-Menten terms [82-84], which are derived from the Michaelis-Menten equations for the simplest case of an irreversible enzyme reaction, converting a single substrate (A) into a product (P) by enzyme (E).

$$A + E \underset{k_{-1}}{\overset{k_1}{\rightleftharpoons}} EA \xrightarrow{k_2} E + P$$

The time-dependent variations of the individual reactants are expressed by the differential equations:

$$\frac{\mathrm{d}[\mathrm{A}]}{\mathrm{d}t} = -k_1[\mathrm{A}][\mathrm{E}] + k_{-1}[\mathrm{EA}] \tag{2.17}$$

$$\frac{\mathrm{d}[\mathrm{E}]}{\mathrm{d}t} = -k_1[\mathrm{A}][\mathrm{E}] + (k_{-1} + k_2)[\mathrm{EA}] \tag{2.18}$$

$$\frac{\mathrm{d}[\mathrm{EA}]}{\mathrm{d}t} = k_1[\mathrm{A}][\mathrm{E}] - (k_{-1} + k_2)[\mathrm{EA}] \tag{2.19}$$

$$\frac{\mathrm{d}[\mathrm{P}]}{\mathrm{d}t} = -k_2[\mathrm{EA}] = v \tag{2.20}$$

where [A], [E] and [EA] are the concentrations of substrate, enzyme and enzyme-substrate complex. *v* is the turnover rate defined as the product formation. It depends on and is therefore directly proportional to the amount of complex EA. The time-dependent changes of [EA] and [E] can be taken to be zero: d[EA]/dt=d[E]/dt=0. Then equations (2.17) and (2.18) simplify to:

$$k_1[\mathrm{A}][\mathrm{E}] = (k_{-1} + k_2)[\mathrm{EA}] \tag{2.21}$$

Substitution of [E] according to the principle of mass conservation, $[\mathrm{E}]_0 = [\mathrm{E}] + [\mathrm{EA}]$, yields the term

$$[EA] = \frac{k_1[\mathrm{A}][\mathrm{E}]_0}{k_1[\mathrm{A}] + k_{-1} + k_2} \tag{2.22}$$

by entering this into equation (2.20) a relationship between turnover rate and substrate amount is obtained:

$$v = \frac{\mathrm{d}[\mathrm{P}]}{\mathrm{d}t} = k_2[\mathrm{EA}] = \frac{k_2[\mathrm{E}]_0[\mathrm{A}]}{\frac{k_{-1}+k_2}{k_1} + [A]} = \frac{V[\mathrm{A}]}{K_\mathrm{m} + [A]} \tag{2.23}$$

$$V = k_2[\mathrm{E}]_0 \tag{2.24}$$

$$K_m = \frac{k_{-1}+k_2}{k_1} \tag{2.25}$$

where the expression $(k_1+k_2)/k_1$ contains three rate constants which are combined into a common constant K_m, the Michaelis-Menten constant, while $k_2[\mathrm{E}]_0$ is replaced by *V*, the maximum

velocity. This equation, based on the steady-state theory, is of fundamental importance for enzyme kinetics.

In the simulation, the turnover rate is usually used to represent the substrate (such as, O_2 and glucose) consumption rate. Moreover, modified Michaelis-Menten kinetics has been proposed to more approach the realistic substrate consumption rate [80]. For instance, a modification function plotting the measurements is multiplied to the Michaelis-Menten term.

2.1.4. Substate transport across cell membrane

Cell membranes act as barriers to most, but not all, molecules. The permeability of a membrane to different substances depends on several factors relating to the interaction of the phospholipids bilayer with the solute: lipid solubility, size, charge and preference of channels and transporters. Based on these factors, there exist three principal ways for a substance traversing the cell membrane: passive, active and bulk transport. The passive transport is diffusion of a substance across a membrane with no energy investment, no use of ATP. It contains simple diffusion, dialysis, osmosis and facilitated diffusion.

Essential small molecules, such as O_2 and CO_2, can cross the cell membrane by diffusion, which is one principle method of substrate movements within cells. The diffusion is the net movement of a substance from an area of higher concentration to an area of lower concentration and therefore leads to the equal concentrations on both sides of cell membrane. Large polar molecules and ions cannot pass through phospholipid bilayer, so that they diffuse through a semipermeable membrane with the help of special proteins (channel or carrier proteins). Examples include glucose and radioactive tracers, which traverse the membrane largely with facilitation of transporters (*e.g.*, glucose transporters). Principally, transport occurs in both direction (*cis* and *trans* cite of the membrane) and is regarded as a reversible process, similar to any chemical and thus to any enzyme catalyzed reaction. Based on this fact, instead of the simple Michaelis-Menten equation, the relationship derived for reversible reactions should be applied [89], where A_1 is the substance to be transported at the *cis* site, and A_2 the substance after the transport at the *trans* site; E is the free transport system:

$$v_{\mathrm{T}} = \frac{(k_1 k_2 [\mathrm{A}_1] - k_{-1} k_{-2} [\mathrm{A}_2])[\mathrm{E}]_0}{k_1 [\mathrm{A}_1] + k_{-2} [\mathrm{A}_2] + k_{-1} + k_2} \tag{2.26}$$

Regarding only a uni-direction transport from the *cis* to the *trans* site, the term $k_{-1}k_{-2}[A_2]$ for the reverse transport may be disregarded and therefore the above equation reduces to:

$$v_{\mathrm{T}} = \frac{k_1 k_2 [\mathrm{A}_1][\mathrm{E}]_0}{k_1[\mathrm{A}_1] + k_{-2}[\mathrm{A}_2] + k_{-1} + k_2} \tag{2.27}$$

If conditions are chosen, where the substrate concentration at the *trans* site A_2 is zero, the transport rate v_T simplifies to the Michaelis-Menten equation, $k_2[E]_0$ being the maximum velocity:

$$v_{\mathrm{T}} = \frac{k_2[\mathrm{A}_1][\mathrm{E}]_0}{[\mathrm{A}_1] + \frac{k_{-1}+k_2}{k_1}} = \frac{V_1[\mathrm{A}_1]}{K_{\mathrm{m}1} + [\mathrm{A}_1]} \tag{2.28}$$

Generally the transport must be regarded from both sites. For each of the sites a Michaelis-Menten equation may be taken, the net flow being the difference between both individual flows:

$$v_{\mathrm{T}} = \frac{V_1[\mathrm{A}_1]}{K_{\mathrm{m}1} + [\mathrm{A}_1]} - \frac{V_2[\mathrm{A}_2]}{K_{\mathrm{m}2} + [\mathrm{A}_2]} \tag{2.29}$$

This equation fits for the cases of both asymmetry and symmetry transports. For the symmetric transport, V and K_m are same for both sites:

$$v_{\mathrm{T}} = V K_{\mathrm{m}} \frac{[\mathrm{A}_1] - [\mathrm{A}_2]}{(K_{\mathrm{m}} + [\mathrm{A}_1])(K_{\mathrm{m}} + [\mathrm{A}_2])} \tag{2.30}$$

Active transport spends energy, usually in the form of ATP, to move a substance across a cell membrane against its natural tendency, up a concentration gradient. It requires the use of carrier protein, and includes protein-mediated active transport (*e.g.*, sodium potassium pump) and co-transport (*e.g.*, lactate$^-$ and H^+ co-transport). As an example, the kinetics of carrier-mediated transport of lactate across mammalian plasma membranes involves rapid-equilibrium lactate and proton binding, with the proton binding first (ordered-binding), and the lactate may bind only to the transporter in the proton-bound state, and only the fully unbound carrier or the fully bound carrier can undergo a conformational change associated with transport of substrates across the membrane. The following elementary steps constitute a symmetric ordered-binding scheme with protons binding the unbound carrier (E1 or E2) and lactate binding the proton-bound carrier (EH1 or EH2) [47]:

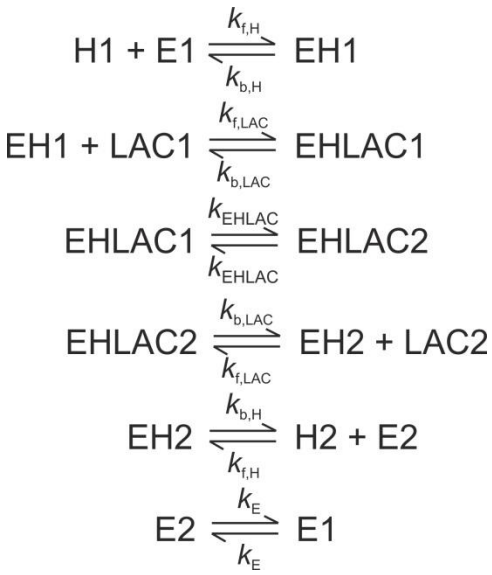

Here the two sides of the membrane are labeled 1 and 2. The enzyme states with binding sites exposed to side 1 are denoted E1, EH1, and EHLAC1. Similarly, enzyme states with binding sites exposed to side 2 are denoted E2, EH2, and EHLAC2. Protons and lactate on side 1 are denoted H1 and LAC1, respectively; protons and lactate on side 2 are denoted H2 and LAC2.

From the above scheme, the unidirectional carrier fluxes from side 1 (*cis* site) to side 2 (*trans* site) are (the intermediate formula induction is not presented here):

$$flux_{12} = k_{\mathrm{EHLAC}}[\mathrm{EHLAC1}] = k_{\mathrm{EHLAC}}\frac{k_{\mathrm{f,LAC}}}{k_{\mathrm{b,LAC}}}[\mathrm{EH1}][\mathrm{LAC1}] \tag{2.31}$$

$$flux_{21} = k_{\mathrm{EHLAC}}[\mathrm{EHLAC2}] = k_{\mathrm{EHLAC}}\frac{k_{\mathrm{f,LAC}}}{k_{\mathrm{b,LAC}}}[\mathrm{EH2}][\mathrm{LAC2}] \tag{2.32}$$

Therefore, the net flux is given by

$$J_{12} = flux_{12} - flux_{21} \tag{2.33}$$

where, apparent [LAC1] K_{m} of $flux_{12}$ is given by:

$$K_{m,12}^{\mathrm{LAC1}} = \frac{K_{LAC}[\frac{k_E}{k_{EHLAC}}\left(1+\frac{[H2]}{K_H}+\frac{[H2][LAC2]}{K_HK_{LAC}}\right)+\left(\frac{[H2][LAC2]}{K_HK_{LAC}}+\frac{k_E}{k_{EHLAC}}\right)(1+\frac{[H1]}{K_H})]}{\frac{[H1]}{K_H}[\left(1+\frac{[H2]}{K_H}+\frac{[H2][LAC2]}{K_HK_{LAC}}\right)+\left(\frac{[H2][LAC2]}{K_HK_{LAC}}+\frac{k_E}{k_{EHLAC}}\right)]} \tag{2.34}$$

Apparent [LAC1] V_{max} of $flux_{12}$ is written by:

$$V_{max,12}^{\mathrm{LAC1}} = \frac{k_{EHLAC}[E_0]\left(\frac{[H2][LAC2]}{K_H K_{LAC}} + \frac{k_E}{k_{EHLAC}}\right)}{\left(1+\frac{[H2]}{K_H}+\frac{[H2][LAC2]}{K_H K_{LAC}}\right)+\left(\frac{[H2][LAC2]}{K_H K_{LAC}}+\frac{k_E}{k_{EHLAC}}\right)} \tag{2.35}$$

Apparent [LAC2] K_{m} of $flux_{12}$ is given by:

$$K_{m,12}^{\mathrm{LAC2}} = \frac{K_{LAC}[\frac{k_E}{k_{EHLAC}}\left(1+\frac{[H1]}{K_H}+\frac{[H1][LAC1]}{K_H K_{LAC}}\right)+\left(\frac{[H1][LAC1]}{K_H K_{LAC}}+\frac{k_E}{k_{EHLAC}}\right)(1+\frac{[H2]}{K_H})]}{\frac{[H2]}{K_H}[\left(1+\frac{[H1]}{K_H}+\frac{[H1][LAC1]}{K_H K_{LAC}}\right)+\left(\frac{[H1][LAC1]}{K_H K_{LAC}}+\frac{k_E}{k_{EHLAC}}\right)]} \tag{2.36}$$

Apparent [LAC2] V_{max} of $flux_{12}$ is expressed by

$$V_{max,12}^{\mathrm{LAC2}} = \frac{k_{EHLAC}[E_0]\left(\frac{[H1][LAC1]}{K_H K_{LAC}} + \frac{k_E}{k_{EHLAC}}\right)}{\left(1+\frac{[H1]}{K_H}+\frac{[H1][LAC1]}{K_H K_{LAC}}\right)+\left(\frac{[H1][LAC1]}{K_H K_{LAC}}+\frac{k_E}{k_{EHLAC}}\right)} \tag{2.37}$$

K_{H} and K_{LAC} are defined equilibrium constants: $K_{\mathrm{H}} = k_{\mathrm{b,H}}/k_{\mathrm{f,H}}$, $K_{\mathrm{LAC}} = k_{\mathrm{b,LAC}}/k_{\mathrm{f,LAC}}$.

The ordered (as illustrated above) and random-binding mechanisms can be simulated by kinetic models, and apparent kinetic parameters for specific types of experiments are derived. Based on the analysis of the expressions for the apparent kinetic parameters, additional experiments can be proposed to be able to distinguish between ordered and random-binding mechanisms.

Due to facilitated and active transport, most ions and molecules in tumors have unequal concentrations on both sides of the cell membrane, therefore the P_{s} in equations (2.10) and (2.11) representing local production/consumption of extracellular substrates $[S_{\mathrm{ex}}]$ should be substituted by the transport term $T_{\mathrm{s}}([S_{\mathrm{ex}}], [S_{\mathrm{in}}])$:

$$\frac{\partial [S_{\mathrm{ex}}]}{\partial t} = D_s \nabla^2 [S_{\mathrm{ex}}] - z_s \nabla [S_{\mathrm{ex}}] \cdot \frac{\vec{C}}{\vec{B}} - \frac{z_s [S_{\mathrm{ex}}](AB - \vec{C}\cdot\vec{D})}{B^2} + T_{\mathrm{s}}([S_{\mathrm{ex}}], [S_{\mathrm{in}}]) \tag{2.38}$$

And the evolvement intracellular substrate $[S_{\mathrm{in}}]$ satisfies the reaction equation (no diffusion involved):

$$\frac{\partial [S_{\mathrm{in}}]}{\partial t} = T_{\mathrm{s}}([S_{\mathrm{ex}}], [S_{\mathrm{in}}]) + P_s([S_{\mathrm{in}}])) \tag{2.39}$$

2.2. Machine learning algorithms for molecular imaging

The machine learning methods including supervised, unsupervised and ensemble learning have been widely used for molecular imaging [90]. Supervised learning is the machine learning task of inferring a function (*i.e.*, predictor model) from labeled training data and generating

reasonable predictions of the response to new data. Supervised learning splits into two broad categories: classification (such as support vector machine, discriminant analysis, nearest neighbors and naïve Bayers classification) and regression (such as linear, non-linear, generalized linear and decision tree regression). The regression model is more computationally efficient that classification model. Unsupervised learning tries to find hidden structure in unlabeled data and it comprises hierarchical, k-Means and k-Medoids clustering, and Gaussian mixture and Hidden Markov models for clustering.

The regression and classification algorithms have been applied in molecular image analysis for improving diseases (*e.g.*, lesions and brain diseases) identification and prediction [91-94]. For example, the supervise machine learning has been used to derive the system matrix for the image reconstruction of radiotracer uptake in lesions. The system matrix is adapted by learning the simulated lesion features. The method improves the quantitative accuracy of lesion metabolism analysis and makes the lesion identification more precisely [95]. In order to select a more accurate model for pharmacokinetic analysis, the machine learning method (temporal difference reinforcement learning) is also used for model selection and parameter estimation [96].

Regression models describe the relationship between a dependent variable y (*i.e.*, response variable), and independent variable or variables, X (*i.e.*, predictor variables). The matrix, X, of observations on predictor variable usually called the design matrix. A multiple linear regression model can be expressed as [97, 98]

$$y_i = b_0 + b_1 X_{i1} + b_2 X_{i2} + \cdots + b_p X_{ip} + \varepsilon_i \qquad i = 1, \cdots, n \tag{2.40}$$

where y_i is the ith response. b_j is the jth coefficient and b_0 is the constant term in the model. X_{ij} denotes the ith observation on the jth predictor variable, $j = 1, \cdots, p$. ε_i is the ith random noise term.

The general form of a linear regression model is

$$y_i = b_0 + \sum_{k=1}^{K} b_k f_k(X_{i1}, X_{i2}, \cdots, X_{ip}) + \varepsilon_i \qquad i = 1, \cdots, n \tag{2.41}$$

where $f(.)$ is a scalar-valued function of the independent variables X_{ij}. The functions $f(X)$ might be in any form including nonlinear functions or polynomials

The multivariate linear regression model expresses a d-dimensional continuous response vector as a linear combination of predictor terms plus a vector of error terms with a multivariate normal distribution. The multivariate linear regression model is

$$\boldsymbol{y_i} = \boldsymbol{X_i b} + \boldsymbol{\varepsilon_i} \tag{2.42}$$

where $\boldsymbol{y_i} = (y_{i1}, \dots, y_{id})'$ denote the response vector for observation i, $i = 1, \dots, n$. $\boldsymbol{b}$ and $\boldsymbol{X_i}$ is $K \times 1$ coefficient vector and $d \times K$ design matrix. The d-dimensional vector of error terms follows a multivariate normal distribution

$$\boldsymbol{\varepsilon_i} \sim MVN_d(0, \Sigma) \tag{2.43}$$

Parametric nonlinear models represent the relationship between a continuous response variable and one or more continuous predictor variables in the form

$$y = f(X, b) + \varepsilon \tag{2.44}$$

where, y is an n×1 vector of observations of the response variable. f is any function of X and b that evaluates each row of X along with the vector b to compute the prediction for the corresponding row of y. X is an n×p matrix of predictors, with one row for each observation, and one column for each predictor. b is a p×1 vector of unknown parameters to be estimated. ε is an n×1 vector of independent, identically distributed random noises.

To estimate the values of the parameters b in regression models, the mean squared differences between the observed responses y and the predictions of the model $f(X, b)$ are minimized by algorithms such as least squares estimation, maximum likelihood estimation [99]. The parameter estimations by ordinary least squares (OLS) and covariance-weighted least squares (CWLS) algorithms, two types of least squares estimation, are illustrated here.

The coefficients are estimated using iterative least squares estimation for non-linear regression model. While as to linear regression model, the OLS estimate for the coefficient vector $\boldsymbol{b}$ that minimizes

$$\sum_{i=1}^{N} (\boldsymbol{y_i} - \boldsymbol{X_i b})'(\boldsymbol{y_i} - \boldsymbol{X_i b}) \tag{2.45}$$

The $K \times 1$ vector of OLS regression coefficient estimates is

$$\boldsymbol{b}_{\text{OLS}} = (\boldsymbol{X'X})^{-1}\boldsymbol{X'y} \tag{2.46}$$

The CWLS introduces a diagonal matrix $\boldsymbol{C}_0$, whose inverse matrix C_0^{-1} contain weights for each dimension to model heteroscedasticity. Given $\boldsymbol{C}_0$, the CWLS solution is the vector **b** that minimizes

$$\sum_{i=1}^{N} (\boldsymbol{y_i} - \boldsymbol{X_i b})'\boldsymbol{C}_0(\boldsymbol{y_i} - \boldsymbol{X_i b}) \tag{2.47}$$

In this case, the $K \times 1$ vector of CWLS regression coefficient estimates is

$$\boldsymbol{b}_{\mathrm{CWLS}} = (\boldsymbol{X}'(\boldsymbol{I}_n \otimes \boldsymbol{C}_0)^{-1}\boldsymbol{X})^{-1}\boldsymbol{X}'(\boldsymbol{I}_n \otimes \boldsymbol{C}_0)^{-1}\boldsymbol{y} \tag{2.48}$$

where $\boldsymbol{I}_n$ is unit diagonal matrix. Because of the length limitation, the thesis is not going to extend the introduction of regression algorithms.

Among a variety of classification models, the support vector machine (SVM) is widely used due to its high predictive accuracy [100-102]. For instance, neurodegenerative diseases, such as Alzheimer's disease and mild cognitive impairment, are classified and predicted with SVM using the brain-region specific features from molecular image (MRI or fMRI image) [103, 104]. An SVM classifies data by finding the best hyperplane that separates all data points of one class from those of the other class. The best hyperplane for an SVM means the one with the largest margin between the two classes. Given some training data: a set of *n* points (vectors) $\boldsymbol{x}_i$ along with their categories y_i, $i = 1, \cdots, n$. The y_i is either 1 or -1 indicating the class to which the point $\boldsymbol{x}_i$ belongs. The aim of the SVM is to maximum margin hyperplane that divides the points having $y_i = 1$ from those having $y_i = -1$. The equation of any hyperplane is

$$\boldsymbol{w} \cdot \boldsymbol{x} - b = 0 \tag{2.49}$$

where $\boldsymbol{w}$ denotes the normal vector to the hyperplane. The parameter $b/\|\boldsymbol{w}\|$ determines the offset of the hyperplane from the origin along the normal vector $\boldsymbol{w}$

Two hyperplanes are selected in a way to separate the data and then their distance is maximized. The region bound by them is called "the margin". This hyperplanes are described by the equations:

$$\boldsymbol{w} \cdot \boldsymbol{x} - b = 1 \quad \text{and} \quad \boldsymbol{w} \cdot \boldsymbol{x} - b = -1 \tag{2.50}$$

The distance between these two hyperplanes is $2/\|\boldsymbol{w}\|$, the $\|\boldsymbol{w}\|$ is minimized to obtain the largest distance under the constraint to prevent the date points falling into the margin:

$$y_i(\boldsymbol{w} \cdot \boldsymbol{x_i} - b) \geq 1, \qquad i = 1, \ldots, n \tag{2.51}$$

Considering the mathematical convenience, the optimization problem of SVM is usually given as the equivalent problem of minimizing $\|\boldsymbol{w}\|^2/2$:

$$\operatorname{argmin}_{(\boldsymbol{w},b)} \frac{\|\boldsymbol{w}\|^2}{2} \qquad \text{subject to } y_i(\boldsymbol{w} \cdot \boldsymbol{x_i} - b) \geq 1 \tag{2.52}$$

By introducing the Lagrange multipliers $\boldsymbol{\alpha}$, the above constrained problem can be expressed as:

$$\text{argmin}\ \max_{(\boldsymbol{w},b)\ \ \alpha\geq 0}\left\{\frac{1}{2}\|\boldsymbol{w}\|^2-\sum_{i=1}^{n}\alpha_i[y_i(\boldsymbol{w}\cdot\boldsymbol{x_i}-b)-1]\right\} \tag{2.53}$$

A modified maximum margin ideal that allows for mislabeled examples has been developed [101] and this algorithm deals with the data sets which cannot be split completely. In this case the soft margin method is put forward will choose a hyperplane that splits the examples as cleanly as possible. Therefore, the objective function is increased by a function which penalizes non-zero ξ_i, and the optimization becomes a tradeoff between a large margin and a small error penalty. The optimization problem becomes:

$$\text{argmin}_{(\boldsymbol{w},b)}\left\{\frac{\|\boldsymbol{w}\|^2}{2}+C\sum_{i=1}^{n}\xi_i\right\} \qquad \text{subject to } y_i(\boldsymbol{w}\cdot\boldsymbol{x_i}-b)\geq 1 \tag{2.54}$$

The optimization with Lagrange multipliers is therefore modified into:

$$\arg\min_{(\boldsymbol{w},b,\boldsymbol{\xi})}\max_{\boldsymbol{\alpha},\boldsymbol{\beta}\geq 0}\left\{\frac{1}{2}\|\boldsymbol{w}\|^2+C\sum_{i=1}^{n}\xi_i-\sum_{i=1}^{n}\alpha_i[y_i(\boldsymbol{w}\cdot\boldsymbol{x_i}-b)-1+\xi_i]-\sum_{i=1}^{n}\beta_i\xi_i\right\} \tag{2.55}$$

The SVM optimization will be illustrated later in section 4.2.1.

2.3. Image reconstruction algorithms for molecular imaging

The 2D and 3D imaging reconstruction algorithms used in PET mainly include the classical analytic algorithm and the iterative algorithm. The typical analytic algorithm is filtered-back-projection (FBP) algorithm, which is characterized by its linearity and easier control of the spatial resolution and noise correlations in the reconstruction and therefore it still remains important in a number of reconstruction algorithms. The iterative algorithm is of increasing importance. Using the iterative algorithm, the image quality can be improved by more accurate modeling of the data acquisition. Among the variety of iterative methods, the maximum-likelihood expectation maximization (ML-EM) algorithm and its accelerated version: ordered subset expectation maximization (OSEM) are most original and popular.

The number of coincident events detected by a pair of detectors D_a and D_b (associated with an LOR: $\mathcal{L}_{D_a,D_b}$) is a Poisson variable with a mean: [16]

$$\langle p_{D_a,D_b}\rangle=\tau\int_{\text{FOV}}d\vec{r}f(\vec{r})\psi_{D_a,D_b}(\vec{r}) \tag{2.56}$$

where τ is the acquisition time and $f(\vec{r})$ denotes the tracer concentration. FOV is the field of view with the radium R_F and $f(\vec{r})$ is assumed as zero out of FOV. Recovering $f(\vec{r})$ is the aim of reconstruction. $\psi_{D_a,D_b}(\vec{r})$ indicates the sensitivity function ($\vec{r}=(x,y,z)$). The analytic

algorithms model each tube of response as a mathematical line joining the center of the front face of the two crystals. Thus the sensitivity function is zero except when $\vec{r} \in \mathcal{L}_{D_a,D_b}$. With this approximation, the detected coincident events can be expressed by a line integral of the tracer distribution [16]:

$$\langle p_{D_a,D_b} \rangle = \int_{\mathcal{L}_{D_a,D_b}} d\vec{r} f(\vec{r}) \tag{2.57}$$

Using indices (D_a, D_b) to parameterize PET data often induces adapting problem. An alternative *sinogram* parameterization is therefore used, where the variables s and ϕ represent the location and orientation of the LOR (the transaxial sonogram coordinates), respectively. The line integral of the tracer distribution in 2D space is then defined as

$$p(\phi, s, z_0) = \int_{-\infty}^{+\infty} dt\, f(x = s\cos\phi - t\sin\phi, y = s\sin\phi + t\cos\phi, z = z_0) \tag{2.58}$$

where *t* is the coordinate along the line. $0 \leq \phi < \pi$ and $|s| < R_{\mathrm{F}}$. The above equation indicates the *x-ray transform*, which transforms the function $f(\vec{r})$ into its sinogram $p(s, \phi)$ by operator X: $p(s, \phi) = (Xf)(s, \phi)$.

Tomographic reconstruction relies on Fourier analysis. The Fourier transform of a function $f(x, y)$ is defined:

$$(\mathcal{F}f)(v_x, v_y) = F(v_x, v_y) = \int_{\mathbb{R}^2} dxdyf(x, y)\exp(-2\pi i(xv_x + yv_y)) \tag{2.59}$$

And the inverse Fourier transform is

$$(\mathcal{F}^{-1}F)(x, y) = f(x, y) = \int_{\mathbb{R}^2} dv_x dv_y F(v_x, v_y)\exp(2\pi i(xv_x + yv_y)) \tag{2.60}$$

where v_x and v_y denote the frequencies associated to x and y, respectively.

The central section theorem states that the 1D Fourier transform of x-ray transform with respect to the radial variable *s* is related to the 2D Fourier transform of the image *f*.

$$P(\nu, \phi) = F(v_x = \nu\cos\phi, v_y = \nu\sin\phi) \tag{2.61}$$

where

$$P(\nu, \phi) = (\mathcal{F}\mathrm{p})(\nu, \phi) = \int_{\mathbb{R}^2} dsp(\phi, s)\exp(-2\pi is\nu) \tag{2.62}$$

ν is the frequency associated to the radial variable s.

Combing equations (2.59)-(2.61), the tracer concentration $f(x,y)$ can be estimated by FBP inversion, which has two steps of inversions:

$$f(x,y) = (X^* p^{\mathrm{F}})(x,y) = \int_0^{\pi} d\phi p^F(s = x\cos\phi + y\sin\phi, \phi) \tag{2.63}$$

where the filtered projections are

$$p^{\mathrm{F}}(s,\phi) = \int_{-R_F}^{R_F} ds' p(s',\phi) h(s-s') \tag{2.64}$$

And the ramp filter kernel is defined as:

$$h(s) = \int_{-\infty}^{+\infty} d\nu |\nu| \exp(2\pi i s \nu) \tag{2.65}$$

The operator X^* mapping p^{F} onto f is called the back projection. $(X^* p^{\mathrm{F}})(x,y)$ is the sum of the filtered data p^{F} for all lines that contain the point (x, y).

As to the iterative algorithms, the mean number of events detected for one LOR is written as

$$\langle \vec{p} \rangle = \{\langle p_j \rangle = \tau \int_{\mathrm{FOV}} d\vec{r} f(\vec{r}) \psi_j(\vec{r}), j = 1, \dots, N_{\mathrm{LOR}}\} \tag{2.66}$$

where j represents the detector pair (d_a, d_b) for the simplification, and N_{LOR} is the number of detector pairs in coincidence. The sensitivity function $\psi_j(\vec{r})$ depends on attenuation and scatter, gaps in the detectors, non-uniform resolution of the detectors, *etc.*

Iterative algorithms model the image as a linear combination of the basis functions:

$$f(\vec{r}) \approx \sum_{i=1}^{P} f_i b_i(\vec{r}) \tag{2.67}$$

Therefore the mean number of the events detected by the jth detector pair:

$$\langle p_j \rangle = \sum_{i=1}^{P} a_{j,i} f_i \qquad j = 1, \dots, N_{\mathrm{LOR}} \tag{2.68}$$

where the elements of the *system matrix* are

$$a_{j,i} = \tau \int_{\mathrm{FOV}} d\vec{r} b_i(\vec{r}) \psi_j(\vec{r}) \qquad j = 1, \dots, N_{\mathrm{LOR}}; i = 1, \dots, P$$

In order to reconstruct the tracer image, the objective function $Q(\vec{f} = (f_1, \dots, f_p), \vec{p})$ is defined, which is determined by the unknown imaging coefficients and the measured data. The estimated tracer distribution *f** can be obtained by optimizing the objective function. The general ways for tracer image estimation is:

$$f^* = \text{argmax}_{\vec{f},\, f_i \geq 0} \; Q(\vec{f}, \vec{p}) \tag{2.69}$$

The objective function in the ML-EM and OSEM algorithms is the Poisson likelihood:

$$Q(\vec{f}, \vec{p}) = \sum_{j=1}^{N_{LOR}} \{ -\sum_{i=1}^{P} a_{j,i} f_i + p_j \log(\sum_{i=1}^{P} a_{j,i} f_i) \} \tag{2.70}$$

The optimization of the objective function can be achieved by a variety of methods, such as Gradient-based methods, methods using subsets of the image vector, methods based on surrogate cost functions, block-iterative methods. The ML-EM can be derived using surrogate functions.

The EM iteration is a mapping of the current image estimate $\vec{f}^n$ onto the next estimate $\vec{f}^{n+1}$ until the equilibrium (convergence) is reached:

$$f_i^{n+1} = f_i^n \frac{1}{\sum_{j'=1}^{N_{\text{LOR}}} a_{j',i}} \sum_{j=1}^{N_{\text{LOR}}} a_{j,i} \frac{p_j}{\sum_{i'=1}^{P} a_{j,i'} f_{i'}^n} \qquad i = 1, \dots, P \tag{2.71}$$

This objective function increases monotonically at each iteration and converges for $n \to \infty$ to an image $\vec{j}^*$ maximizing the loglikelihood.

The OSEM algorithm is the modification of ML-EM algorithm. The LOR data is divided into *S* disjoint subsets $J_1, \dots, J_S \subset [1, \dots, N_{\text{LOR}}]$. Each subset is processed in a well-defined order and the iterations have the form:

$$f_i^{n+1} = f_i^n \frac{1}{\sum_{j' \in J_{\text{n, mod S}}} a_{j',i}} \sum_{j \in J_{\text{n, mod S}}} a_{j,i} \frac{p_j}{\sum_{i'=1}^{P} a_{j,i'} f_{i'}^n} \qquad i = 1, \dots, P \tag{2.72}$$

where $J_{\text{n, mod S}}$ indicates the subset at iteration *n*.

2.4. Data analysis and pharmacokinetic modeling

Pharmacokinetics describes how the body affects a specific drug (such as biomarkers in molecular imaging) after administration through the mechanisms of absorption and distribution, as well as the chemical changes of the substance in the body (e.g. by metabolic enzymes), and the effects and routes of excretion of the metabolites of the drug [16, 105]. A number of different

models have been developed in order to simplify conceptualization of the many processes that take place in the interaction between an organism and a drug. One of these models, the compartment model, gives the best approximation to reality. In the application of PET or positron imaging, one tissue compartment model and two tissue compartment model are usually used for modeling the blood blow and tracer accumulation in tumors, respectively.

2.4.1. One and two tissue compartment models

The one tissue compartment model has been used to describe the bidirectional flux of tracer between blood and tissue, as shown in Figure 2.1. The model is characterized by time-dependent tracer concentration in tissue, $C_t(t)$, and arterial blood, $C_a(t)$ and two first-order kinetic rate constants (K_1, k_2). It is assumed that within each compartment (blood and tissue) the tracer is homogeneously distributed. The unidirectional tracer flux from blood to tissue is K_1C_a, and the flux from tissue to blood is k_2C_t; therefore, the net tracer flux into tissue is [16]:

$$\frac{dC_t}{dx} = K_1C_a - k_2C_t \tag{2.73}$$

This equation can be solved for C_t to obtain:

$$C_t = K_1C_a \otimes \exp(-k_2t) \tag{2.74}$$

where the symbol $\otimes$ denotes one-dimensional convolution. If C_a and C_t are radioactivity concentrations, then k_2 implicitly includes a component for radioactive decay. For a PET scan, C_t is the radioactivity concentration that is measured in a given tissue region. Blood samples may be drawn during a PET scan in order to measure C_a. If the tracer distribution in a tissue region is adequately described by the one-tissue model, then with serial measurements of C_t and C_a, can be applied using standard nonlinear regression techniques to estimate the values of K_1 and k_2 for that region.

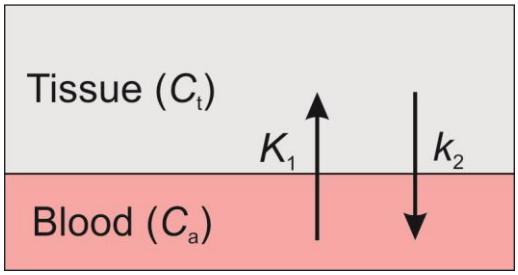

Figure 2.1. One-tissue compartment model describes the bidirectional flux of tracer between blood (C_a) and tissue (C_t).

The model for the measurement of glucose with [^{18}F]FDG in a homogeneous tissue includes two tissue compartments as shown in Figure 2.2 [16]. Tracer is taken up (K_1) from arterial plasma into compartment C_1. A fraction of it diffuses back to plasma (k_2), another fraction moves further to compartment C_2 (k_3). Unless tracer is trapped in the C_2 compartment (k_4=0), transfer back to the intermediate compartment is also going on. Therefore, the kinetic parameters: K_1, k_2, k_3 and k_4 reflect cellular influx, efflux, phosphorylation and de-phosphorylation of the tracer, respectively. So the differential equations for the two tissue compartment model are:

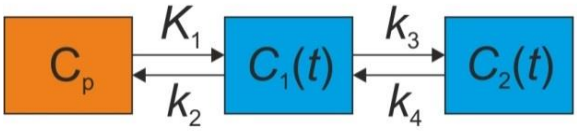

Figure 2.2. The two-tissue compartment model

$$\frac{dC_1(t)}{dt} = K_1 C_p - (k_2 + k_3)C_1(t) + k_4 C_2(t) \tag{2.75}$$

$$\frac{dC_2(t)}{dt} = k_3 C_1(t) - k_4 C_2(t) \tag{2.76}$$

The solution to these coupled differential equations is as follows:

$$C_1(t) = \frac{K_1}{\alpha_2 - \alpha_1}[(k_4 - \alpha_1)\exp(-\alpha_1 t) + (\alpha_2 - k_4)\exp(-\alpha_2 t)] \otimes C_p(t) \tag{2.77}$$

$$C_2(t) = \frac{K_1 k_3}{\alpha_2 - \alpha_1}[\exp(-\alpha_1 t) - \exp(-\alpha_2 t)] \otimes C_p(t) \tag{2.78}$$

$$C_{\mathrm{i}}(t) = \frac{K_1}{\alpha_2 - \alpha_1}[(k_3 + k_4 - \alpha_1)\exp(-\alpha_1 t) + (\alpha_2 - k_3 - k_4)\exp(-\alpha_2 t)] \otimes C_p(t) \tag{2.79}$$

where $C_{\mathrm{i}}(t) = C_1(t) + C_2(t)$ is the total FDG activity in tissue. $\otimes$ denotes the operation of convolution. α_1 and α_2 are functions of the model rate constant K_1, k_2, k_3 and k_4

$$\alpha_1 = (k_2 + k_3 + k_4 - \sqrt{(k_2 + k_3 + k_4)^2 - 4k_2 k_4})/2 \tag{2.80}$$

$$\alpha_2 = (k_2 + k_3 + k_4 + \sqrt{(k_2 + k_3 + k_4)^2 - 4k_2 k_4})/2 \tag{2.81}$$

2.4.2. Graphical analysis: Patlak plot

The two tissue compartment model for analyzing tracer kinetics is relatively complex and may be not suitable for certain human populations. Therefore, this model is simplified by model-based method [106-108]. The basic concept of this method is converting measured data into a straight-line plot whose slope and/or intercept has physiological meaning. The parameters in the method can be determined for functional imaging by non-iterative linear regression methods on a pixel-by-pixel basis. The graphical analysis is the most commonly used model-based method and usually uses the Patlak plot to deal with the two tissue compartment model with irreversible or nearly irreversible trapping step (k_4 is zero or small) [106, 107].

In the two tissue compartment model, the solution for the total tissue tracer concentration $C(t)$ with an arbitrary input function $C_p(t)$ is given by equation (2.79). If k_4 is zero and input function $C_p(t)$ is constant, the solution would be

$$C(t) = C_p\{\frac{K_1 k_2}{(k_2+k_3)^2}(1 - \exp[-(k_2 + k_3)t]) + \frac{K_1 k_3}{k_2+k_3}t\} \tag{2.82}$$

After an appropriate time, the exponential term of the above equation becomes sufficiently small, the ratio of tissue to blood activity becomes:

$$\frac{C(t)}{C_p} = \frac{K_1 k_2}{(k_2+k_3)^2} + \frac{K_1 k_3}{k_2+k_3}t \tag{2.83}$$

where $K = K_1 k_3/(k_2 + k_3)$ denotes the net uptake rate of tracer into the irreversibly bound compartment 2, and $k_3/(k_2 + k_3)$ is the fraction of the tracer in the tissue the reaches the irreversible compartment.

For the case when the input function $C_p(t)$ is not constant, the ratio of tissue to blood activity is:

$$\frac{C(t)}{C_p(t)} = V_0 + K(\frac{\int_0^t C_p(s)ds}{C_p(t)}) \tag{2.84}$$

where V_0 means the initial volume of distribution. $\int_0^t C_p(s)ds\,/C_p(t)$ is the stretch time and it distorts time based on the shape of the input function. By plotting the ratio of tissue to blood activity versus stretch time, the parameters K and V_0 are obtained. In order to use the Patlak plot, the linearity of the data over the range of time used should be verified. The parameters can also be estimated by multiple linear regressions to fit the measured tissue data directly:

$$C(t) = V_0 C_p(t) + K\int_0^t C_p(s)ds$$

2.4.3. Parameter estimation

Given the measurements of tissue activity and the input function and a proposed model configuration, one can produce estimates of the underlying rate constants. There are many ways to accomplish the estimation of model parameters and the most commonly used method of parameter estimation is called *least-squares estimation*. The goal of this technique is to find values for the model rate constants that, when inserted into the model equations, produce the "best" fit to the tissue measurements. Quantitatively, the goal is to minimize an optimization function, specifically the sum of the squared differences between the measured tissue concentration data and the model prediction.

$$\min \sum_{i=1}^{N} (C_i - C(T_i))^2 \tag{2.85}$$

where there are N tissue measurements, C_i, i=1,…,N, at times T_i, and $C(T_i)$ is the model prediction of tissue activity at each of these times.

Figure 1.3(b) and (c) present an example of kinetic constant estimation using pharmacokinetic model in our microfluidic chip protocol. The C_p is measured and corrected (the modeled medium chamber activity). The difference of measured cell chamber activity and modeled medium chamber activity is taken as C_i. By fitting the C_i curve with time, the K_1, k_2, k_3, k_4 are obtained. The constant k_3 indicating the FDG phosphorylation rate is estimated for the SkBr3 cells treated with and without low glucose supply. The SkBr3 cells incubated in low glucose condition has higher k_3 by least-square estimation, which involves the phosphorylation rate is up-regulated under low glucose situation.

3. Computational modeling of metabolism mechanism for molecular imaging of solid tumor

Molecular imaging such as PET detecting [^{18}F]FDG, hyperpolarized MRI detecting [^{13}C]lactate, or MRS assessing pH has been applied for the characterization of tumor phenotypes through measurement of the related metabolism of certain substrates. On the other hand, certain proteins such as cluster of differentiation 31 (CD31), GLUT1 or MCT1 are usually stained or analyzed in pathophysiology for the characterization of tumor phenotypes. However, the interpretation of substrate metabolism with regard to pathological understanding is not straightforward and less quantitative. Substrate metabolisms are usually regulated by several factors of the sophisticated tumor metabolome, such as enzymes of metabolic pathways and transporters. The higher levels of certain types of enzymes and transporters are considered to be correlated with tumor malignancy [28, 109-111] and consequently influence the tumor metabolism. Quantitative investigation of the relationship between enzyme (over)expression and the relevant metabolism may assist the development of corresponding diagnostic, therapeutic, and prognostic strategies.

Glycolysis followed by lactic acid formation (even in the presence of oxygen) is a predominant metabolic pathway of glucose in malignant cancer (Warburg effect). The production and metabolism of lactate are closely associated with glucose metabolism and involve a series of interactions between oxygenation status, enzymes and substrates. Glucose is primarily taken up (mediated by GLUT, in particular GLUT1) and metabolized (catalyzed by HK, especially HKII) in hypoxic tumor cells for glycolytic energy production and the provision of building blocks for anabolic pathways. The pyruvate produced is subsequently converted into lactic acid. The accumulation of lactate renders the tumor acidic, especially in hypoxic regions. Many tumor studies on lactate have predominantly focused on its presence, accumulation and possible triggering of tumor progression and metastasis [112]. However, it has been shown that lactate can also be utilized as an energy source [113]. The lactate generated in hypoxic/glycolytic cells can be exported, shuttled interstitially, taken up and used by normoxic tumor cells in some cancer types such as human cervix cancer or breast cancer MDA-MB-231 cells [43, 114].

MCT4 - which has a lower affinity for lactate - has been reported to be responsible for lactate export from cells, and MCT1 (which has a higher affinity for lactate) has been identified as the transporter for lactate uptake [42, 115]. Therefore, lactate is considered as being an “ambivalent” compound since hypoxic/glycolytic and normoxic tumor cells mutually regulate their access to energy metabolites [43]. However, detailed quantitative information on glucose metabolism and lactate oxidation in the sophisticated tumor microenvironment (TME) remains elusive.

This chapter will establish a platform to investigate the quantitative relationship between expressions of several transporters, a key enzyme and a transcriptional factor: GLUT, MCT1, MCT4, HK, HIF-1, and the metabolisms of glucose and lactate, and pH distribution (including FDG uptake). And the co-influence of multiple pathophysiological factors on the tumor microenvironment will be estimated. To reach these goals, computational models of glucose metabolism and lactate oxidation were established.

3.1. Model design

To investigate the relationship between imaging features (glucose, lactate and pH) and relevant pathophysiological factors (microvascular density, GLUT, HK, MCT1 and MCT4 expressions), a computational simulation model was set up on an artificial 2D TME [34, 82-86]. The simulation model takes into account the pathways of glucose metabolism and lactate oxidation. The considered substrates, regulating enzymes and transporters and their interactions are illustrated in Figure 3.1. The premature and chaotic tumor microvasculature causes heterogeneous distributions of oxygen and glucose [21]. In regions remote from the vessel, hypoxic cells have a high rate of glycolysis and take up great amounts of glucose through GLUT, producing lactate and increasing (extracellular) acidity. The excessive intracellular lactate produced by hypoxic cells is exported by the transporter MCT4, shuttled partly toward normoxic cells and then imported via MCT1 [42, 43]. In normoxic cells, lactate will be oxidized together with glucose turnover, which is a combination of glycolysis and respiration [80]. To model these procedures, the concentrations of substrates, including oxygen, extra- and intracellular glucose, extra- and intracellular lactate, carbon dioxide (CO_2), hydrogen (H^+) and sodium cations (Na^+), bicarbonate (HCO_3^-) and chloride (Cl^-) anions, are considered during the computational simulation. The flow chart of the model implementation is presented in Figure 3.3, where the analysis of the quantitative relationship between enzymatic, vascular phenotypes and substrate distributions as the aim of the study is highlighted by yellow box.

In addition, since HIF-1 is reported to regulate the expressions of key enzyme and transporters involved in the glucose and lactate metabolism, the above model can be driven by HIF-1. Therefore a model driven by HIF-1 is constructed to investigate HIF-1 influence on the tumor metabolism. As the glucose metabolism in tumors is usually reflected by FDG imaging, the FDG accumulation is integrated into the established TME with consideration of FDG competition with glucose for enzyme (HK) and transporter (GLUT). As shown in Figure 3.2, after cellular import, glucose and FDG are phosphorylated into glucose-6-phosphate (G6P) and FDG-6-phosphate (FDG6P), respectively. FDG6P cannot be further metabolized (the 2' hydroxyl group (-OH) in normal glucose is needed for further glycolysis, but FDG is missing this 2' hydroxyl) and trapped in cells, waiting for positron decay, while G6P may be used for further glycolysis and/or enter the mitochondria for TCA cycle and other applications. This FDG uptake (transport and phosphorylation) process is modeled with implementation procedure illustrated in Figure 3.4.

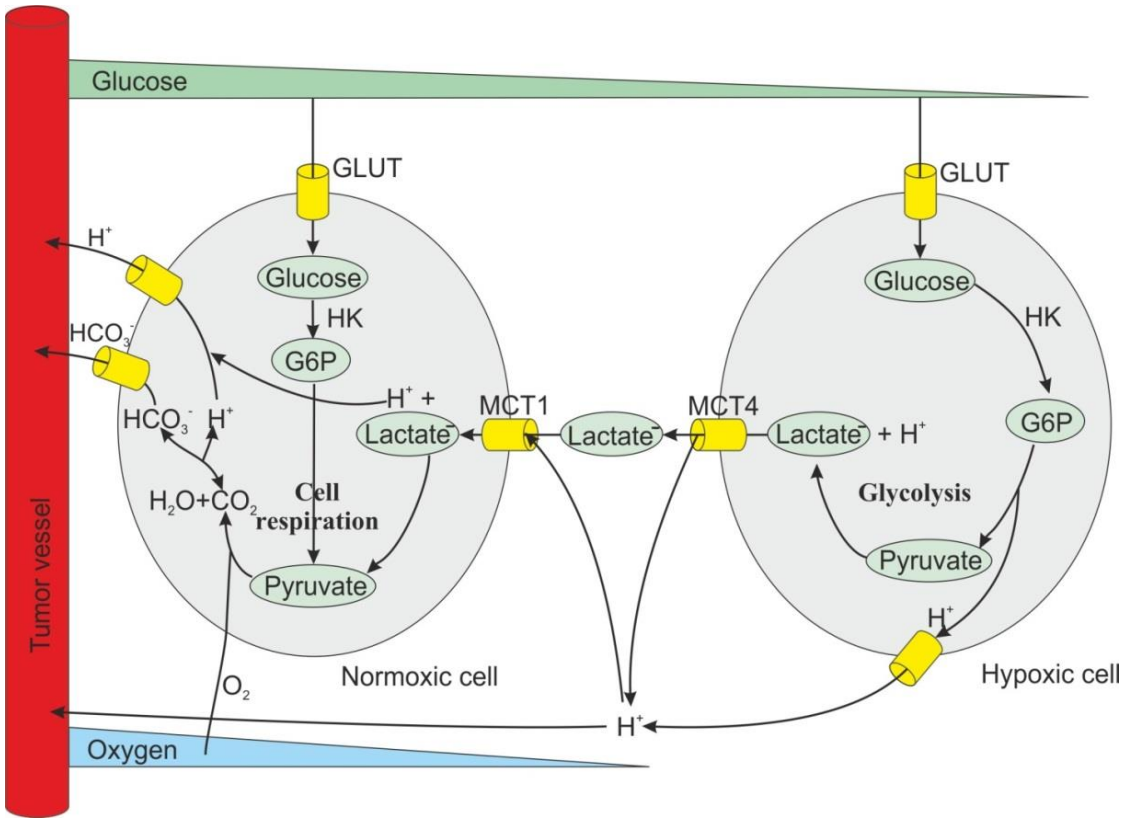

Figure 3.1. Schematic presentation of the physiological processes considered in the simulation. Only the glucose and lactate metabolic pathways and related transporters, and the key enzyme HK involved in the model are depicted.

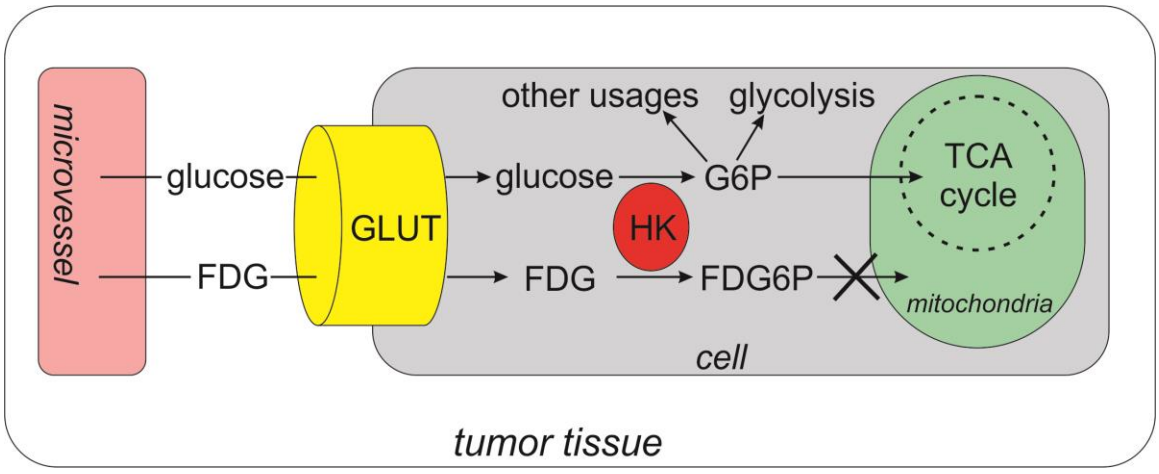

Figure 3.2. Schematic presentation of the physiological processes of FDG and glucose uptake by tumor cell. They compete for GLUT and HK for transport and metabolism.

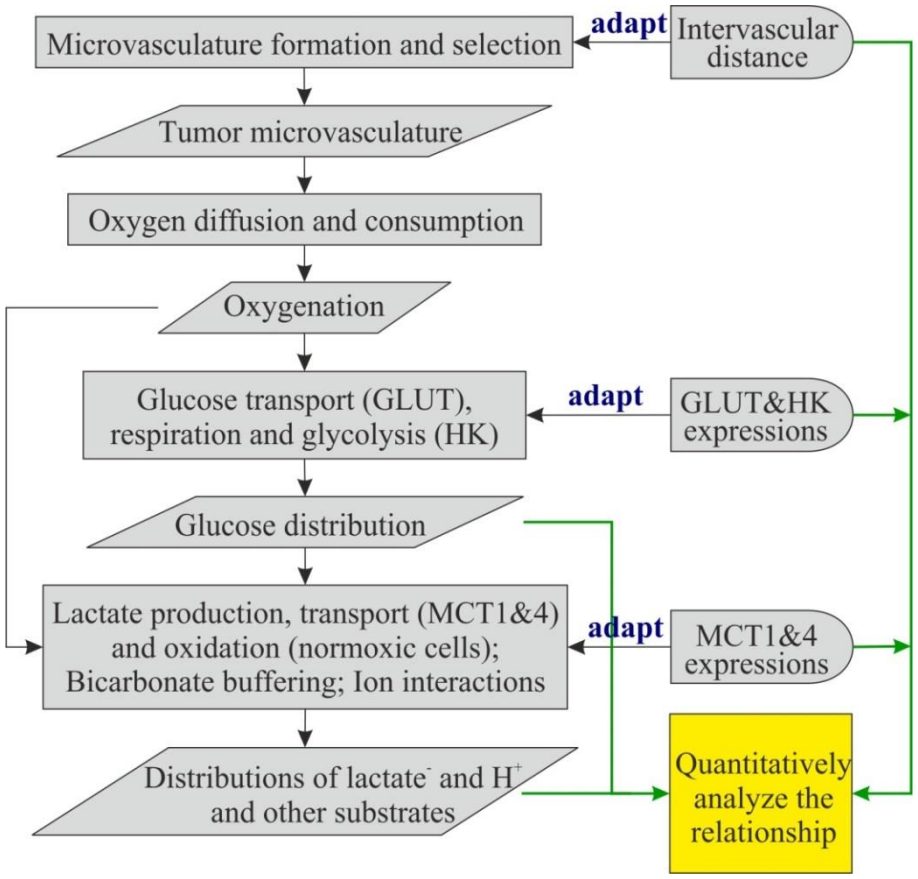

Figure 3.3. Flow chart of the model implementation. The analysis of quantitative relationship of enzymatic (expressions of GLUT, HK, MCT1&4), vascular phenotypes and substrate (glucose, $lactate^-$ and H^+) distributions as the study aim is highlighted by yellow box.

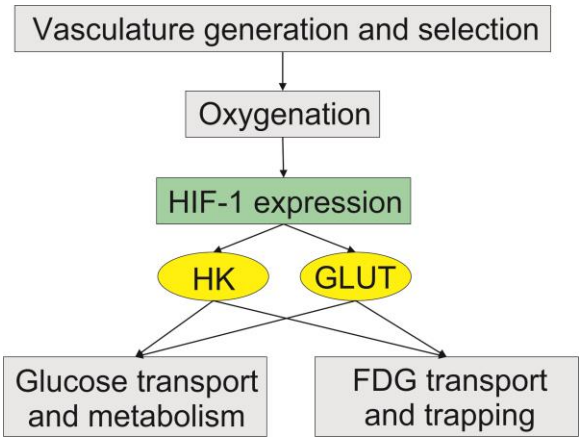

Figure 3.4. Flow chart of FDG model implementation. The glucose and FDG uptakes are mediated by GLUT and HK, which are regulated by HIF-1.

3.1.1. Tumor vasculature

For the artificial 2D TME in the current simulation model, the microvessels are assumed to be of a uniform dimension and to be randomly distributed in the 2D domain [82, 116]. The 2D domain of the simulation is tessellated into 35×35 grids with a grid size of 10 μm. Each microvessel occupies one grid in the 2D domain. The grids without mirovessels are assumed to be possessed by cells [83, 85]. Blood shunting and temporary collapsing/occlusion of tumor microvessels are not taken into account.

The intervascular distance was used to characterize the microvascular distribution in the artificial 2D simulation. The mean intervascular distance is used as a surrogate parameter of microvascular density. The intervascular distances of tumor microvessels were shown to have a log-normal distribution as seen in quantitative tumor microvascular corrosion casting [23, 24]. We formed a 2D vasculature, with the distribution of the intervascular distances following a statistically logarithmic normal distribution and extracted the parameters by fitting the data presented by [24]. To restrict the random distribution of 2D microvessels, the intervascular distances of the randomly distributed 2D microvessels were further controlled by adopting the Kolmogorov-Smirnov test to examine the log-normal distribution. Only if the intervascular distances of the randomly distributed microvessels satisfied the log-normal distribution was the 2D tumor microvasculature considered for the further simulation.

3.1.2. Oxygenation status

In this study, the glucose metabolism and lactate oxidation are assumed to be partly driven by the oxygenation status [79]. The spatio-temporal distribution of oxygen can be described by a reaction-diffusion equation [82, 83, 117]. Convective oxygen transport in the TME is not considered and a constant diffusion coefficient is employed for all of the tumor tissue, *i.e.*, oxygen can freely diffuse through tissue. Similarly, oxygen can traverse cell membranes freely due to low molecular mass and dimension and tumor vessel leakage. The oxygen concentration is therefore described by [82]:

$$\frac{\partial[\mathrm{O_2}]}{\partial t} = D_{\mathrm{O_2}}\nabla^2[\mathrm{O_2}] - P([\mathrm{O_2}]) \tag{3.1}$$

$$P([\mathrm{O_2}]) = \frac{V_{\mathrm{max,\,O_2}}\cdot[\mathrm{O_2}]}{K_{\mathrm{m,\,O_2}}+[\mathrm{O_2}]} \tag{3.2}$$

where $[O_2]$ is the local concentration of oxygen. $P([O_2])$ is the oxygen consumption rate (Michaelis-Menten term of oxygen), $V_{\max,\,O_2}$ represents the maximum oxygen reaction rate, $K_{\mathrm{m},\,O_2}$ is the oxygen concentration at half maximum consumption rate (*i. e.*, the Michaelis-Menten constant of oxygen consumption). $[O_2]$ (unit: mol/L) can also be converted into oxygen tension pO_2 (unit: mmHg) by Henry's law with the transfer constant for oxygen: 769.2 L atm/mol [83]. D_{O_2} is the diffusivity of oxygen (oxygen diffusion constant).

3.1.3. Glucose metabolism

Cellular glucose uptake is facilitated by the transporter GLUT. Subsequently, intracellular glucose is metabolized with catalyzation by HK and then transformed into glucose-6-phosphate (G6P) before being metabolized. In this model, glucose is divided into three physiological compartments: extracellular, intracellular and metabolized glucose. The spatio-temporal evolution of their concentrations is described by:

$$\frac{\partial[\mathrm{G_{ex}}]}{\partial t} = D_{\mathrm{G}}\nabla^2[\mathrm{G_{ex}}] - T([\mathrm{G_{ex}}] - [\mathrm{G_{in}}])_{\mathrm{GLUT}} \tag{3.3}$$

$$\frac{\partial[\mathrm{G_{in}}]}{\partial t} = T([\mathrm{G_{ex}}] - [\mathrm{G_{in}}])_{\mathrm{GLUT}} - P([\mathrm{G_{in}}])_{\mathrm{HK}} \tag{3.4}$$

$$\frac{\partial[\mathrm{G_{me}}]}{\partial t} = P([\mathrm{G_{in}}])_{\mathrm{HK}} \tag{3.5}$$

$$T([\mathrm{G_{ex}}] - [\mathrm{G_{in}}])_{\mathrm{GLUT}} = \frac{V_{\max,\,\mathrm{GLUT}} K_{\mathrm{m},\,\mathrm{GLUT}}([\mathrm{G_{ex}}]-[\mathrm{G_{in}}])}{(K_{\mathrm{m},\,\mathrm{GLUT}}+[\mathrm{G_{ex}}])(K_{\mathrm{m},\,\mathrm{GLUT}}+[\mathrm{G_{in}}])} \tag{3.6}$$

$$P([\mathrm{G_{in}}])_{\mathrm{HK}} = \frac{V_{\max,\,\mathrm{HK}}[\mathrm{G_{in}}]}{K_{\mathrm{m},\,\mathrm{HK}}+[\mathrm{G_{in}}]} \tag{3.7}$$

where $[G_{ex}]$, $[G_{in}]$, and $[G_{me}]$ are the concentrations of extracellular, intracellular and metabolized glucose, respectively. $T([G_{ex}]-[G_{in}])_{GLUT}$ is the transmembrane transport term of glucose, which is determined by the concentration difference and kinetic parameters of GLUT. $V_{max,GLUT}$ and $K_{m,GLUT}$ are the maximum transport rate and Michaelis-Menten constant of GLUT for glucose transport. In this study, the kinetics of GLUT are assumed to have identical parameters at both sides of the cell membranes [89]. This is based on the consideration that the transmembrane transport of glucose uses facilitated diffusion (*i.e.*, carrier mediated transport) in most cases rather than active (directly ATP-dependent) transport [47, 89, 118]. $P([G_{in}])_{HK}$ represents the metabolic rate of intracellular glucose; $V_{max,HK}$ and $K_{m,HK}$ are the maximum reaction rate and the Michaelis-Menten constant of HK for glucose phosphorylation.

3.1.4. Lactate oxidation

In the current model, the presence of lactate is distinguished as being extra- and intracellular lactate. The excessive intracellular lactate produced as a result of the high rate of glycolysis in hypoxic cells is exported by MCT4 [119], forming a positive gradient of extracellular lactate between hypoxic and normoxic regions and promoting extracellular lactate shuttling towards normoxic regions. In normoxic regions, the accumulated extracellular lactate is imported mainly by MCT1 and oxidized for energy production [43]. The movement of ions in the TME can be modeled with a reaction-diffusion scheme [79]. The diffusion of charged species is determined by both the concentration gradient and the electric potentials generated by interactive ions within the model. Based on the reaction-diffusion equations of ions, the evolvement of the concentration of extracellular lactate [L_{ex}] and intracellular lactate [L_{in}] can be described as:

$$\frac{\partial[\mathrm{L_{ex}}]}{\partial t} = D_{\mathrm{L}}\nabla^2[\mathrm{L_{ex}}] - z_{\mathrm{L}}\nabla[\mathrm{L_{ex}}]\cdot\frac{\vec{C}}{B} - \frac{z_{\mathrm{L}}[\mathrm{L_{ex}}](AB-\vec{C}\cdot\vec{D})}{B^2} - T([\mathrm{L_{ex}}]-[\mathrm{L_{in}}]) \tag{3.8}$$

$$\frac{\partial[\mathrm{L_{in}}]}{\partial t} = T([\mathrm{L_{ex}}]-[\mathrm{L_{in}}]) + P([\mathrm{L_{in}}]) \tag{3.9}$$

where A, B, $\vec{C}$, $\vec{D}$ - in relation to the electric potential effect - depend on the charges and concentrations of the interacting ions (H^+, HCO_3^-, Na^+ and Cl^-) involved in the model, whereby their specific expressions are listed in the Section 2.1.2. $T([\mathrm{L_{ex}}]-[\mathrm{L_{in}}])_{\mathrm{MCT}}$ is the transmembrane transport term of lactate by MTCs. MCT1 expression and hypoxia have been reported to be mutually exclusive in SiHa human cervix squamous carcinoma cells and WiDr human colorectal adenocarcinoma cells [43], and MCT4 is strongly expressed in glycolytic tissues and is upregulated by hypoxia [30]. Thus, it is possible to assume that MCT1 is prevalent in normoxic regions and is responsible for lactate import whereas MCT4 is expressed in hypoxic regions and is responsible for the export of excessive intracellular lactate. The overall transmembrane transport term of lactate is described by the following function:

$$T([L_{\mathrm{ex}}]-[L_{\mathrm{in}}])_{\mathrm{MCT}} = \begin{cases} T([L_{\mathrm{ex}}]-[L_{\mathrm{in}}])_{\mathrm{MCT1}}, & \text{in normoxic regions } (pO_2 > 2.5 \text{ mmHg}) \\ T([L_{\mathrm{ex}}]-[L_{\mathrm{in}}])_{\mathrm{MCT4}}, & \text{in hypoxic regions } (pO_2 \leq 2.5 \text{ mmHg}) \end{cases} \tag{3.10}$$

$$T([\mathrm{L_{ex}}]-[\mathrm{L_{in}}])_{\mathrm{MCT1}} = \frac{V_{\mathrm{max,\,MCT1}}K_{\mathrm{m,\,MCT1}}([\mathrm{L_{ex}}]-[\mathrm{L_{in}}])}{(K_{\mathrm{m,\,MCT1}}+[\mathrm{L_{ex}}])(K_{\mathrm{m,\,MCT1}}+[\mathrm{L_{in}}])} \tag{3.11}$$

$$T([\mathrm{L_{ex}}]-[\mathrm{L_{in}}])_{\mathrm{MCT4}} = \frac{V_{\mathrm{max,\,MCT4}}K_{\mathrm{m,\,MCT4}}([\mathrm{L_{ex}}]-[\mathrm{L_{in}}])}{(K_{\mathrm{m,\,MCT4}}+[\mathrm{L_{ex}}])(K_{\mathrm{m,\,MCT4}}+[\mathrm{L_{in}}])} \tag{3.12}$$

where $T([\mathrm{L_{ex}}]-[\mathrm{L_{in}}])_{\mathrm{MCT}}$ is the transmembrane transport term for lactate, equal to MCT1-facilitated transport $T([\mathrm{L_{ex}}]-[\mathrm{L_{in}}])_{\mathrm{MCT1}}$ in normoxic regions or MCT4-facilitated transport

$T([L_{ex}]-[L_{in}])_{MCT4}$ in hypoxic regions. $V_{max,\ MCT1}$ and $V_{max,\ MCT4}$ are the maximum transmembrane transport rates of MCT1 and MCT4. $K_{m,\ MCT1}$ and $K_{m,\ MCT4}$ represent the Michaelis-Menten coefficients of the transmembrane transport of lactate by MCT1 and MCT4, respectively [119-121].

In tumor tissue, the lactate distribution is the result of lactate production and lactate consumption and is determined by the availability of glucose and oxygen [42, 43]. Thus, the metabolic rate of lactate $P([L_{in}])$ is balanced by the consumption rates of oxygen $P([O_2])$ and glucose $P([G_{in}])_{HK}$ and is estimated by the following equation [79]:

$$P([L_{in}]) = 2P([G_{in}])_{HK} - P([O_2])/3 \tag{3.13}$$

This relation is derived by considering the overall effect of glucose metabolism and lactate oxidation. The production and oxidation of lactate follow the reactions:

$$C_6H_{12}O_6 \rightarrow 2C_3H_5O_3^- + 2H^+$$

$$2C_3H_5O_3^- + 2H^+ + 6O_2 \rightarrow 6CO_2 + 6H_2O$$

While the oxidation of glucose can be written as follows:

$$C_6H_{12}O_6 + 6O_2 \rightarrow 6CO_2 + 6H_2O$$

If the lactate production and oxidation were to take place entirely within the same cell, the overall metabolic rate of glucose vs. the overall metabolic rate of oxygen during lactate production and oxidation would fulfill the relative relation 1:6, which is equivalent to the relative relation during glucose oxidation. Thus, without the shuttling of lactate (export and import between the cells), the metabolic rate of glucose and the consumption rate of oxygen would be kept at a ratio of 1:6 (other pathways which consume oxygen are not considered here). The excessive production of lactate caused by the higher ("extra") glucose uptake in conjunction with the high-rate glycolysis, depends on the imbalance of the availability of glucose and oxygen. In hypoxic regions, more glucose is available than oxygen [21] and the ratio of the glucose metabolic rate vs. the oxygen consumption rate is larger than 1:6. The additional turnover of glucose leads to the production of lactate [80]. In normoxic regions, the glucose metabolic rate vs. the oxygen consumption rate is less than 1:6. The additional consumption of oxygen is due to the oxidation of lactate [43]. In the current simulation, a positive metabolic rate of lactate represents the production of lactate and a negative metabolic rate of lactate refers to its oxidation.

3.1.5. Distribution of extracellular pH

To model the distribution of extracellular pH, we only considered two pathways of the proton (H^+) metabolism in the simulation model. The first is the production and consumption of protons during lactate metabolism. The second is the interconversion of carbon dioxide (CO_2) and bicarbonate, which regulates tumor acidity [80]. The overall reversible reaction of CO_2 hydration can be written as:

$$CO_2 + H_2O \rightleftharpoons H^+ + HCO_3^-$$

The direction of this reaction is -inter alia- greatly dependent on the pH of the medium [122, 123]. The rate constant for the hydration reaction is k_f (k_f = 0.146 s^{-1}) and the rate constant for the dehydration reaction is k_r ($k_r = 17.3 \times 10^{-4}$ $(M\ s)^{-1}$) [124].

The extracellular distribution of the protons [H^+] can be described using the reaction-diffusion equation of an ion [79]:

$$\frac{\partial[H^+]}{\partial t} = D_{H^+}\nabla^2[H^+] - z_{H^+}\nabla[H^+]\cdot\frac{\vec{C}}{B} - \frac{z_{H^+}[H^+](AB-\vec{C}\cdot\vec{D})}{B^2} - P([H^+]) \quad (3.14)$$

$$P([H^+]) = P_1([H^+]) + P_2([H^+]) \quad (3.15)$$

$$P_1([H^+]) = 2P([G_{in}]) - P([O_2])/3 \quad (3.16)$$

$$P_2([H^+]) = P([O_2]) + k_f[CO_2] - k_r[H^+][HCO_3^-] \quad (3.17)$$

where [H^+], [CO_2] and [HCO_3^-] represent the extracellular concentrations of the protons, carbon dioxide and bicarbonate ions, respectively. D_H and z_H are the diffusion constant and the charge of protons. P([H^+]) is the production rate of protons which includes the rate accompanied by lactate metabolism P_1([H^+]) and the rate for the hydration of carbon dioxide P_2([H^+]).

Based on oxidation, glycolysis, lactate oxidation and buffering system, the production or consumption rates of the bicarbonate ion P([HCO_3^-]), the chloride ion P([Cl^-]) and carbon dioxide P([CO_2]) are given as follows [79, 80]:

$$P([HCO_3^-]) = P([O_2]) + k_f[CO_2] - k_r[H^+][HCO_3^-] \quad (3.18)$$

$$P([CO_2]) = k_r[H^+][HCO_3^-] - k_f[CO_2] \quad (3.19)$$

$$P\left(\left[Cl^{-}\right]\right) = 0 \tag{3.20}$$

where $[Cl^-]$ is the extracellular concentration of chloride ions.

The Na^+ concentration: $[Na^+]$ is obtained by the electro-neutrality principle:

$$\sum_{ion} z_{ion}[ion] = 0 \tag{3.21}$$

where the summation covers all the ions assumed in the TME. The product of $[Na^+]$ and Na^+ charge is represented by the minus summation of the products of the concentrations and charges of other ions (lactate, H^+, HCO_3^-, Cl^-).

The no-flux boundary condition is applied on the edge of the region of the simulated domain.

3.1.6. Regulation of HIF-1 on tumor metabolism

Tumor cells shift a large part of their metabolisms toward glycolysis, some of which are regulated by HIF-1. HIF-1 acts as a critical intermediator between tissue oxygenation and stimulation factors (*e.g.*, metabolic enzymes and transporters, signal proteins) [30, 125, 126]. The negative correlation with oxygen and HIF-1 concentration has been reported [127]. In the downstream of oxygenation (*e.g.*, glucose and lactate metabolism) HIF-1 regulates the expression of transport and catalyzing proteins in a positive (*e.g.*, GLUT1, HKII and MCT4) or negative way. To explore the effect of HIF-1 mediation, the preceding model is developed by introducing the HIF-1. The expressions of investigated enzyme (HKII) and transporters (GLUT1, MCT1 and MCT4) depend on HIF-1 level. Although the influence of HIF-1 on MCT1 has not been persuasive yet, the MCT1 expression is assumed HIF-dependent here. As to the upstream signaling pathway, HIF-1 level is assumed only dependent on local oxygen content. It has been reported that the HIF-1 levels change exponentially over a physiologically relevant range of oxygen tension in vitro [127]. HIF-1 protein has a half-maximal response between 1.5% and 2% oxygen and a maximal response at 0.5% oxygen. Here an oxygen-HIF curve is fitted to measured data to obtain the normalized HIF-1 level $[HIF]_n$ as the function of oxygen tension $f([O])$ as shown in Figure 3.5. For oxygen tension below 3.6 mmHg and above 42 mmHg, the HIF-1 responses have not presented in the literature, so the HIF-1 is assumed to be at highest expression (normalized value=1) and lowest expression (normalized value = 0.1), respectively.

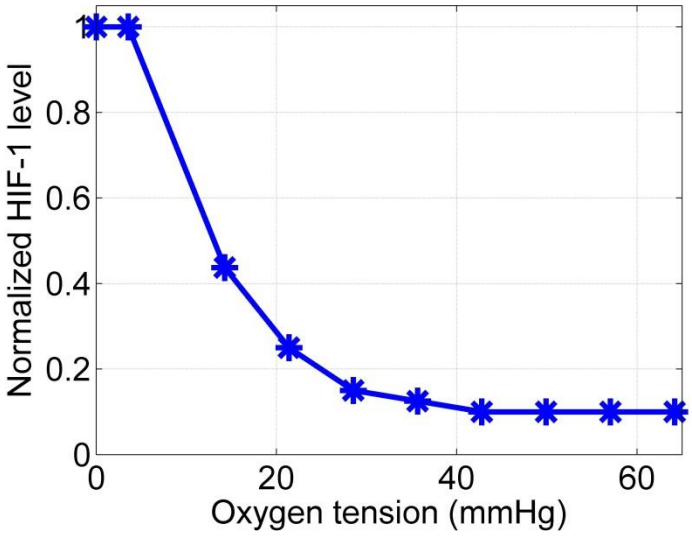

Figure 3.5. The normalized HIF-1 level ($\in [0,1]$) as the function of local oxygen tension.

Except for mapping method using experimental data, the HIF-1 distribution can also be given by an analytic model. Production of cellular HIF-1 is dependent on both the intrinsic capability to synthesis, which is assumed constant, and the degradation due to oxygen existence [128] [117]:

$$\frac{d[\mathrm{HIF}]}{dt} = r_{\mathrm{H}} - V_{\mathrm{max,\ HIF}}\left(\frac{[\mathrm{O_2}]}{[\mathrm{O_2}]+K_{\mathrm{m,\ HIF}}}\right)[\mathrm{HIF}] \tag{3.22}$$

where [HIF] is the cellular HIF-1 concentration. r_{H} is the HIF synthesizing rate. $V_{\mathrm{max,\ HIF}}$ and $K_{\mathrm{m,\ HIF}}$ indicate the maximum HIF-1 degradation rate and the HIF concentration at which the degradation rate is half-maximal. The equilibrium HIF-1 distribution can be acquired when $\frac{d[\mathrm{HIF}]}{dt} = 0$. In the model implementation, the spatial-varying [HIF] is normalized by the maximum value in the field of interest.

In order to include the HIF-1 regulation in the current model, the glucose transport and metabolic terms are adjusted by multiplying a HIF-1 regulation term:

$$T([\mathrm{G_{ex}}]-[\mathrm{G_{in}}])_{\mathrm{GLUT}} = \frac{V^0_{\mathrm{max,GLUT}}K_{\mathrm{m,GLUT}}([\mathrm{G_{ex}}]-[\mathrm{G_{in}}])}{(K_{\mathrm{m,GLUT}}+[\mathrm{G_{ex}}])(K_{\mathrm{m,GLUT}}+[\mathrm{G_{in}}])}\cdot(1+k_{\mathrm{GLUT}}[\mathrm{HIF}]_{\mathrm{n}}) \tag{3.23}$$

$$P([\mathrm{G_{in}}])_{\mathrm{HK}} = \frac{V^0_{\mathrm{max,HK}}[\mathrm{G_{in}}]}{K_{\mathrm{m,HK}}+[\mathrm{G_{in}}]}\cdot(1+k_{\mathrm{HK}}[\mathrm{HIF}]_{\mathrm{n}}) \tag{3.24}$$

where k_{GLUT} is the overexpression factor of GLUT, which indicates the maximum increased folds of transport rate promoted by HIF-1. $V^0_{\mathrm{max,GLUT}}$ and $V^0_{\mathrm{max,HK}}$ are the maximum GLUT transport and HK catalyzing rates in normal tissues. And k_{HK} is the overexpression factor of HK, representing the maximum enhancement of phosphorylation rate caused by HIF-1 upregulation. $T([\mathrm{G_{ex}}]-[\mathrm{G_{in}}])_{\mathrm{GLUT}}$ and $P([\mathrm{G_{in}}])_{\mathrm{HK}}$ are adjusted by $(1+k_{\mathrm{GLUT}}[\mathrm{HIF}]_{\mathrm{n}})$ and $(1+k_{\mathrm{HK}}[\mathrm{HIF}]_{\mathrm{n}})$ respectively, which are linearly correlated with HIF-1 level. Therefore, the expressions of transporters and enzymes are deemed as non-uniform over the field of simulation. HIF-1 expression can maximumly enhance the glucose transport and metabolic rates by k_{GLUT} and k_{HK} folds, respectively.

MCT4 is more expressed in hypoxic region and resposible for lactate export, and MCT1 is exclusive with MCT4 in expression and facilitates lactate import. The transport term of lactate $T([\mathrm{L_{ex}}]-[\mathrm{L_{in}}])_{\mathrm{MCT}}$ is assumed to be a superposition of MCT1 transport $T([\mathrm{L_{ex}}]-[\mathrm{L_{in}}])_{\mathrm{MCT1}}$ and MCT4 transport $T([\mathrm{L_{ex}}]-[\mathrm{L_{in}}])_{\mathrm{MCT4}}$, considering the adjustment of HIF-1:

$$T([\mathrm{L_{ex}}]-[\mathrm{L_{in}}])_{\mathrm{MCT}}=T([\mathrm{L_{ex}}]-[\mathrm{L_{in}}])_{\mathrm{MCT1}}+T([\mathrm{L_{ex}}]-[\mathrm{L_{in}}])_{\mathrm{MCT4}} \tag{3.25}$$

$$T([\mathrm{L_{ex}}]-[\mathrm{L_{in}}])_{\mathrm{MCT1}}=\frac{V^0_{\mathrm{max,\ MCT1}}K_{\mathrm{m,\ MCT1}}([\mathrm{L_{ex}}]-[\mathrm{L_{in}}])}{(K_{\mathrm{m,\ MCT1}}+[\mathrm{L_{ex}}])(K_{\mathrm{m,\ MCT1}}+[\mathrm{L_{in}}])}\cdot\{1+k_{\mathrm{MCT1}}(1-[\mathrm{HIF}]_{\mathrm{n}})\} \tag{3.26}$$

$$T([\mathrm{L_{ex}}]-[\mathrm{L_{in}}])_{\mathrm{MCT4}}=\frac{V^0_{\mathrm{max,\ MCT4}}K_{\mathrm{m,\ MCT4}}([\mathrm{L_{ex}}]-[\mathrm{L_{in}}])}{(K_{\mathrm{m,\ MCT4}}+[\mathrm{L_{ex}}])(K_{\mathrm{m,\ MCT4}}+[\mathrm{L_{in}}])}\cdot(1+k_{\mathrm{MCT4}}[\mathrm{HIF}]_{\mathrm{n}}) \tag{3.27}$$

where k_{MCT1} and k_{MCT4} are the overexpression factors for the transport by MCT1 and MCT4, respectively. $V^0_{\mathrm{max,\ MCT1}}$ and $V^0_{\mathrm{max,\ MCT4}}$ are the maximum MCT1 and MCT4 transport rate usually appeared in normal tissues.

3.1.7. FDG accumulation

[^{18}F]FDG, the most commonly used tracer for clinic and pre-clinic applications of positron emission tomography (PET), is essentially a kind of glucose analog and as a result, its transport and intracellular metabolism procedures are similar with those of glucose. [^{18}F]FDG and glucose are both absorbed by tumor cells with the help of GLUTs, among which GLUT1 has been documented elevating its expression in most cancers [129]. One of the factors responsible for the upregulation of GLUT1 in tumor cells is HIF-1, and a more than 2-fold increase of FDG uptake due to GLUT upregulation was observed [130]. After being transported inside cells, FDG and glucose are subsequently metabolized in a reaction mediated by enzyme HK and get phosphorylated, producing FDG-6-phosphate (FDG6P) and glucose-6-phosphate (G6P) [130].

G6P serves as the intermediate product of tumor respiration and glycolysis, while FDG6P undergoes very slow degradation compared in the time frame of PET imaging. HK I and II belonging to HK family are especially involved in tumor metabolisms and they have different kinetic properties. HK II are quite sensitive to oxygenations and its expression will be promoted almost 3-fold under hypoxic conditions [110], also resulting from the influence of HIF-1.

To simulate the uptake procedure, FDG is divided into extra- and intra-cellular FDG and trapped (or phosphorylated) FDG (FDG6P), whose concentrations are $[\mathrm{FDG_{ex}}]$, $[\mathrm{FDG_{in}}]$ and $[\mathrm{FDG_{tr}}]$, respectively. The FDG competition with glucose for GLUT and HK is integrated (glucose is almost not influenced by the addition of FDG since its concentration is normally several orders higher than FDG concentration). The evolutions of extra- and intra-cellular FDG and trapped FDG satisfy [89, 117]:

$$\frac{\partial[\mathrm{FDG_{ex}}]}{\partial t} = D_{\mathrm{FDG}}\nabla^2[\mathrm{FDG_{ex}}] - T([\mathrm{FDG_{ex}}] - [\mathrm{FDG_{in}}])_{\mathrm{GLUT}} \tag{3.28}$$

$$\frac{\partial[\mathrm{FDG_{in}}]}{\partial t} = T([\mathrm{FDG_{ex}}] - [\mathrm{FDG_{in}}])_{\mathrm{GLUT}} - P([\mathrm{FDG_{in}}])_{\mathrm{HK}} \tag{3.29}$$

$$\frac{\partial[\mathrm{FDG_{tr}}]}{\partial t} = P([\mathrm{FDG_{in}}])_{\mathrm{HK}} \tag{3.30}$$

$$T([\mathrm{FDG_{ex}}] - [\mathrm{FDG_{in}}])_{\mathrm{GLUT}} = (T_{cis} - T_{trans})(1 + k^{\mathrm{F}}_{\mathrm{GLUT}}[\mathrm{HIF}]_{\mathrm{n}}) \tag{3.31}$$

$$T_{cis} = \frac{K_{\mathrm{m,GLUT}}V^{\mathrm{F}}_{\mathrm{max,GLUT}}[\mathrm{FDG_{ex}}]}{K_{\mathrm{m,GLUT}}[\mathrm{FDG_{ex}}]+K^{\mathrm{F}}_{\mathrm{m,GLUT}}[\mathrm{G_{ex}}]+K_{\mathrm{m,GLUT}}K^{\mathrm{F}}_{\mathrm{m,GLUT}}} \tag{3.32}$$

$$T_{trans} = \frac{K_{\mathrm{m,GLUT}}V^{\mathrm{F}}_{\mathrm{max,GLUT}}[\mathrm{FDG_{in}}]}{K_{\mathrm{m,GLUT}}[\mathrm{FDG_{in}}]+K^{\mathrm{F}}_{\mathrm{m,GLUT}}[\mathrm{G_{in}}]+K_{\mathrm{m,GLUT}}K^{\mathrm{F}}_{\mathrm{m,GLUT}}} \tag{3.33}$$

$$P([\mathrm{FDG_{in}}])_{\mathrm{HK}} = \frac{K_{\mathrm{m,\,HK}}V^{\mathrm{F}}_{\mathrm{max,\,HK}}[\mathrm{FDG_{in}}]}{K_{\mathrm{m,\,HK}}[\mathrm{FDG_{in}}]+K^{\mathrm{F}}_{\mathrm{m,\,HK}}[\mathrm{G_{in}}]+K_{\mathrm{m,\,HK}}K^{\mathrm{F}}_{\mathrm{m,\,HK}}}\left(1 + k^{\mathrm{F}}_{\mathrm{HK}}[\mathrm{HIF}]_{\mathrm{n}}\right) \tag{3.34}$$

where $T([\mathrm{FDG_{ex}}] - [\mathrm{FDG_{in}}])_{\mathrm{GLUT}}$ and $P([\mathrm{FDG_{in}}])_{\mathrm{HK}}$ are the transport and metabolic rate of FDG with consideration of its competition with glucose. $T([\mathrm{FDG_{ex}}] - [\mathrm{FDG_{in}}])$ is determined by the difference between T_{cis} (import rate) and T_{trans} (export rate). $V^{\mathrm{F}}_{\mathrm{max,GLUT}}$ and $K^{\mathrm{F}}_{\mathrm{m,GLUT}}$ are the maximum transport rate and the Michaelis-Menten constant, respectively. The term implying the HIF-1 upregulation $(1 + k^{\mathrm{F}}_{\mathrm{GLUT}}[\mathrm{HIF}]_{\mathrm{n}})$ is applied on the FDG transport term with overexpression factor $k^{\mathrm{F}}_{\mathrm{GLUT}}$. $V^{\mathrm{F}}_{\mathrm{max,HK}}$ and $K^{\mathrm{F}}_{\mathrm{m,GLUT}}$ are maximum phosphorylation rate and Michaelis-Menten constant of FDG, respectively. $k^{\mathrm{F}}_{\mathrm{HK}}$ is the HK overexpression factor for FDG phosphrylation.

3.2. Modeling methods

3.2.1. Simulation settings and model parameters

All simulations are programmed in C++ (Microsoft Visual Studio 2008) and the reaction-diffusion equations were solved using finite-difference methods (FDM). The region of interest was a 350 μm × 350 μm micro-tissue-phantom, which is tessellated into 35×35 grids with a grid size of 10 μm. The matrix size and grid size of the tissue phantom are selected considering the compromise between the computation time and the capability to generate stable results. The temporal iteration step size was set to 1 ms. The partial differential equations were iterated until the system converged to equilibrium. Approximately, 5×10^6 (low heterogeneous phantoms with 60 μm mean intervascular distance) to 9×10^6 (high heterogeneous phantoms with 180 μm mean intervascular distance) iterations are required for result convergence. The no-flux boundary condition is applied on the edge of the region of the simulated domain.

The random distribution of tumor microvessels on a tissue phantom is the key reason for TME heterogeneity. The over-heterogeneous vasculature, whose standard deviation (SD) of intervascular distances beyond ±5% of the mean intervascular distance, is discarded. The 5% threshold is selected in consistency with the statistical experiment data [24]. The influences of heterogeneity on simulation results are largely reduced by averaging 20 repeated simulations with same parameters. With considering the heterogeneity control on tumor vasculature, the 20 repetition is tested to be sufficient to obtain constant result errors over a range of intervascular distances.

In the simulation of FDG uptake by tumors, the modeling results were compared with the dynamic PET measurements of 1 h of 2 nude mice with lymphoma xenograft tumors. The plasma input functions were extracted from left ventricle with partial volume correction and spillover correction using addition blood samples.

Substance concentrations and the pH value in the blood of tumor microvessels assumed in the simulation are listed in Table 3.1. The oxygen tension pO_2 is 75-100 mmHg at the arterial end [21, 131] and 10-30 mmHg at the venous end of microvessels [21, 132]. The plasma pO_2 used in the simulation was chosen to be 40 mmHg, a value halfway between the arterial and the venous end (more prone to the venous end). The substrate diffusivities (diffusion constants) in the tumor interstitial space are given in Table 3.1.

Table 3.1. Parameters used in the simulation

Symbol	Parameter	Value	References
Substance levels in the blood plasma of tumor vessels			
C_{O_2}	plasma O_2 concentration	6.8×10^{-2} mM* (40 mmHg)	[82]
C_G	plasma glucose concentration	5.5 mM	[21]
C_L	plasma lactate concentration	15 mM	[133]
C_{CO_2}	plasma CO_2 concentration	2 mM (45 mmHg)	[134]
$C_{HCO_3^-}$	plasma HCO_3^- concentration	25 mM	[134]
C_{Cl^-}	plasma Cl^- concentration	105 mM	[133]
C_{Na^+}	plasma Na^+ concentration	140 mM	[133]
pH	plasma pH	7.4	[80]
Substance diffusivities (diffusion constants) in the tumor interstitium			
D_{O_2}	O_2 diffusivity	1.75×10^{-5} cm^2/s	[80, 82]
D_G	glucose diffusivity	4.5×10^{-7} cm^2/s	[135]
D_L	lactate diffusivity	1.9×10^{-6} cm^2/s	[80]
D_{CO_2}	CO_2 diffusivity	8.9×10^{-7} cm^2/s	[80]
D_{H^+}	H^+ diffusivity	1.9×10^{-6} cm^2/s	[136]
$D_{HCO_3^-}$	HCO_3^- diffusivity	2.2×10^{-7} cm^2/s	[136]
D_{Cl^-}	Cl^- diffusivity	2.26×10^{-7} cm^2/s	[80]
D_{Na^+}	Na^+ diffusivity	3.14×10^{-7} cm^2/s	[80]
Kinetic parameters for substrate metabolism and transport			
K_{m,O_2}	Michaelis-Menten constant for O_2 consumption	2.5 mmHg	[83]
V_{max,O_2}	Max. consumption rate of O_2	15 mmHg/s	[83]
$K_{m,\,GLUT}$	Michaelis-Menten constant of glucose transport via GLUT	6.5 mM	[137-139]
$K_{m,\,HK}$	Michaelis-Menten constant for glycolysis catalyzed by HK	0.19 mM	[130, 140]
$K^F_{m,\,GLUT}$	Michaelis-Menten constant of FDG transport via GLUT	9.8 mM	[130]
$K^F_{m,\,HK}$	Michaelis-Menten constant for FDG phosphorylation catalyzed by HK	0.29 mM	[130]
$K_{m,\,MCT1}$	Michaelis-Menten constant for lactate transport via MCT1	6.8 mM	[30, 43, 141]
$K_{m,\,MCT4}$	Michaelis-Menten constant for lactate transport via MCT4	22 mM	[42, 43]
$\overline{V}_{max,\,GLUT}$	Max. glucose transport rate by GLUT (on average)	1.7 μM/s	[137-139]
$\overline{V}_{max,\,HK}$	Max. glucose glycolytic rate by HK (on	7.9 μM/s	[138, 142]

	average)		
$\overline{V}^{F}_{max,GLUT}$	Max. FDG transport rate by GLUT (on average)	1.7 μM/s	[137-139]
$\overline{V}^{F}_{max,HK}$	Max. FDG phosphorylation rate by HK (on average)	7.9 μM/s	[138, 142]
$\overline{V}_{max,\ MCT1}$	Max. lactate import rate by MCT1 (on average)	0.36 mM/s	[30, 43, 141]
$\overline{V}_{max,\ MCT4}$	Max. lactate export rate by MCT4 (on average)	0.20 mM/s	[121, 143]
Parameters for HIF-1 synthesis and degradation			
r_H	HIF-1 synthesis rate	1.2×10^{-4} s^{-1}	[117]
$V_{max,\ HIF}$	Max. HIF-1 degradation rate	2.3×10^{-3} s^{-1}	[117]
$K_{m,\ HIF}$	Michaelis-Menten constant for FDG degradation	2.5 mmHg	[83, 117]

* M: molar (unit), 1 M =1 mol/L.

The kinetic parameters for transporters and enzymes involved in the model are listed in Table 1.4. They are assumed as being uniform within the tissue phantom. For glucose transport facilitated by GLUT1, $K_{m,\ GLUT}$ has been reported to be 2.6-9.3 mM for 3 different tumor cell lines: T47D, HeLa and MCF7 [137-139, 144] and we have chosen a mean $K_{m,\ GLUT}$ of 6.5 mM in the simulation. $K_{m,\ HK}$ of glucose phosphorylation catalyzed by HKII has been reported as lying between 0.11 and 0.33 mM for T47D, A431 and human glioma cells [130, 144], so that we have chosen the average value of 0.19 mM as $K_{m,\ HK}$ in the simulation.

MCT1 has a higher affinity for lactate and is strongly expressed in the plasma membrane of oxidative muscle fibers. Its $K_{m,\ MCT1}$ =3.5-10 mM was found for the oocyte and mouse Ehrlich-Lettre tumor cells [42, 43, 141]. The $K_{m,\ MCT1}$ in this simulation is taken as being 6.8 mM. MCT4 has a lower affinity for lactate and exists in highly glycolytic cells, such as white muscle cells. It has been reported that $K_{m,\ MCT4}$ varies between 17 and 34 mM for heart and muscle fibers [42, 43, 115]. In the current simulation, the $K_{m,\ MCT4}$ value is chosen as being 22 mM.

The maximum transport rate of glucose via GLUT, $V_{max,\ GLUT}$ is considered to be based on the measurements of the cell lines T47D, HeLa and MCF7 [137-139, 144]. A range of 0.3 to 3.9 μM/s with an average of 1.7 μM/s has been reported. The V_{max} of the phosphorylation (catalyzed by HK) rate has been reported to lie within the range of 0.58 to 11 μM/s (mean 7.9 μM/s) for hepatocarcinoma AS-30D and HeLa cells [138, 142].

The maximum transport rate of lactate by MCT1 $V_{max,\ MCT1}$ was around 0.36 mM/s for mouse Ehrlich-Lettre tumor cells [120, 145]. The maximum transport rate of lactate by MCT4 $V_{max,\ MCT4}$

was reported as 0.11-0.32 mM/s (mean: 0.2 mM/s) for the bovine kidney cell line NBL1 and COS cells [121, 143].

3.2.2. Influence of different pathophysiological conditions on metabolism

To investigate the influences of the expressions of GLUT, HK, MCT1 and MCT4 on the distribution of glucose, lactate and extracellular pH, a series of different V_{max} values were tested. This was based on the consideration that V_{max} is linearly related to the concentration of enzymes/transporters [89]. In this study, we extended the adaptive range of V_{max} to half of the minimal and double the maximum of the range, as listed in the literature considering the possible existing biological/metabolic variability of the tumors. The test ranges of V_{max} for GLUT, HK, MCT1 and MCT4 are listed in Table 3.2. To the best of our knowledge, the range of V_{max} for MCT1 is scarcely available in the literature. In the current study, we have assumed a similar range compared to that of MCT4. Within the adaptive range, we assumed that V_{max} had an interval of 0.25 μM/s for GLUT and HK and an interval of 0.025 mM/s for MCT1 and MCT4.

The influence of microvessel density on the distribution of glucose, lactate and extracellular pH were explored by adjusting the mean intervascular distance of tumor microvasculature. It was adapted from 60 μm (corresponds to high microvessel density and may exist in tumor normoxic regions) to 180 μm (indicates low microvessel density and can be found in hypoxic tumor regions) [24].

Table 3.2. Adaptive parameters of V_{max} of enzymes and transporters assumed in the model

Adaptive Parameter	Meaning	Value scale	References
$V_{max,GLUT}$	Max. glucose transport rate for GLUT	0.15-7.8 μM/s	[137-139, 144]
$V_{max,HK}$	Max. glucose glycolysis rate for HK	0.3-22 μM/s	[138, 142]
$V_{max,MCT1}$	Max. lactate import rate for MCT1	0.05-0.64 mM/s	[121, 143]
$V_{max,MCT4}$	Max. lactate export rate for MCT4	0.05-0.64 mM/s	[121, 143]

In the adjusted model driven by HIF-1, the overexpression factors are defined for GLUT, HK, MCT1 and MCT4 and they are adapted from 1 to 10 to analyze the variations of substrate concentrations. In most cases, the mRNA and protein expressions of GLUT, HK and MCT4 are upregulated <10 folds with the mediation of HIF-1 in tumors (or in hypoxic condition) as reported [125, 146]. Although the MCT1 upregulation driven by HIF-1 has not been proven, MCT1 is overexpressed in hypoxia. It is assumed that MCT1 overexpression is generated by

HIF-1 and the influence of MCT1 overexpression on TME is also studied here. Therefore, the protein expressions (characterizing the transport and catalyzing rates) are determined by the V_{max} in normal tissues and the overexpression factors. Considering the range of V_{max} for each protein (Table 3.2), the V_{max}^0 are chosen: 2 μM/s, 2 μM/s, 0.2 mM/s and 0.2 mM/s for GLUT, HK, MCT1 and MCT4, respectively.

The Pearson correlation coefficient is calculated for the substrate concentration and the V_{max} of the enzyme/transporter in order to investigate the dependence of substrate concentrations on enzyme/transporter expressions.

For the quantification of the responses of glucose, lactate and pH to the different expressions of GLUT, HK, MCT1 and MCT4, we defined the response sensitivity (S) of a substrate as its concentration change ΔC (including the pH change ΔC_{pH}) in response to the adaption ΔV_{max} of V_{max} of a certain enzyme/transporter.

$$S = \frac{\Delta C}{\Delta V_{max}} \tag{3.35}$$

S has the dimension of [s] (ΔC dimension: [M], ΔV_{max} dimension: [M/s]) for glucose and lactate, and the dimension of [s/M] (ΔC_{pH} dimension: 1) for pH.

The response sensitivity to the mean intervascular distance S_v was also evaluated, which was defined as the substrate concentration variation ΔC (including the pH alteration) caused by changes in the intervascular distance ΔD_v:

$$S_v = \frac{\Delta C}{\Delta D_v} \tag{3.36}$$

S_v has the dimension of [M/m] (ΔD_v dimension: [m]) for glucose and lactate, and the dimension of 1/[m] for pH.

In order to quantify the influence of HIF-1 on tumor glucose metabolism, the sensitivities of glucose and FDG concentration/activity in responses to the unit change of overexpression factors ΔOF are proposed:

$$S_{OF} = \frac{\Delta C}{\Delta OF} \tag{3.37}$$

S_{OF} has the same unit with substrate concentration or activity.

4. Computational modeling of positron absorption in silicon detector for high resolution positron imaging

Positron imaging indicates the direct exposure of the silicon detector to positrons. It may suffer from resolution problems caused by multiple scattering of positrons in the silicon and its application in imaging tumor cellular metabolism is therefore constrained. The (spatial) resolution problem cannot be overcome satisfactorily by either hardware (due to limited time resolution) or principle-based modeling (exploiting measured information). Therefore, a supervised learning model and method are proposed with the attempt to improve the spatial resolution of positron imaging. As the Timepix silicon detector is used for the imaging and is capable of recording deposited energies resulting from positron multiple scattering in the detector, the energy information is integrated in learning the model to classify the primary incident position from multiple interaction positions for each positron.

4.1. Principles of positron imaging using Timepix detector

Positron imaging signifies capturing positrons directly before their annihilations and it is of increasing interest in many applications including intraoperative navigation, microfluidic radioassays, digital autoradiography and radioluminenscence microscopy [18-20, 64, 65]. Some technologies have been developed for real-time imaging of positron distributions, such as charged-coupled detector (CCD) with scintillator (and microscope) [19, 64, 65], position sensitive avalanche photodiode (PSAPD) [18], and complementary metaloxide semiconductor (CMOS) [20].

The high resolution imaging is realized by positron camera in our study, which encompasses the Timepix chip as main component (as shown in Figure 4.2(a)). This positron camera is featured by its high sensitivity and spatial resolution, enabling the imaging of dedicated biological structures in *in vivo* and *in vitro* applications.

4.1.1. Timepix detector

The hybrid silicon pixel device Timepix [147] has evolved from Medipix2 [148]. It shares many of the physical dimensions of the Medipix2 chip but has a different functionality at the level of the single pixel. Similarly with Medipix2, the Timepix device consists of a pixelated semiconductor detector chip bump-bonded to a CMOS readout chip. The detector chip contains a 300 μm sensitive layer whose backside is coated with a 5 μm passivation layer. The front-side sensor electrode is divided into a matrix of 256×256 square pixels with a pitch of 55 μm. Each sensor pixel is connected to its preamplifier, discriminator and digital counter integrated on the readout chip. The chip is designed to accept either positive or negative charge input in order not to restrict the choice of the sensor material (Si, GaAs, CdZnTe, etc.). The exposure times can be chosen arbitrarily. The counts are accumulated in a 13-bit counter per pixel. The pixel overflows at 11810 counts. In single particle counting mode each pixel can handle count rates of about 100 kHz of randomly arriving particles. Read-out is performed after exposure to avoid dead time.

Different from Medipix chip operated only in single photon counting mode, each pixel of Timepix chip can work in one of three modes: Medipix mode (counter counts incoming particles), Timepix mode (counter works as a timer and measures the time when the particle is detected) and Time over threshold (TOT) mode (counter is used as a Wilkinson type ADC allowing direct energy measurement in each pixel). In the TOT mode, Timepix measures the radiation-induced charge collected in the pixel via measurement of the width of the preamplifier

signal, which is proportional to the deposited energy [77]. The Timepix silicon detector has been applied for detection of ^{14}C electrons [63, 77], X-ray [149] and ultra-cold neutrons [150], *etc*.

In this study, our positron camera tests the imaging of ^{18}F positron signal (half-life 109.77 min, continuous beta energy up to 633 keV) of a typical PET tracer [^{18}F]FDG. The measurement results are compared with theoretical predictions using Monte-Carlo simulations with Geant4.

4.1.2. Monte-Carlo simulation of positron passing through Timepix detector

Monte-Carlo simulation utilizing Geant4 [151] was carried out for theoretical analysis of experimental results. It models the physical processes of a particle passing through the silicon detector. Its kernel encompasses tracking; geometry description and navigation; material specification; abstract interfaces to physics processes; management of events; run configuration; stacking for track prioritization; tools for handling the detector response; and interfaces to external frameworks, graphics and user interface systems. Geant4 physics processes cover diverse interactions over an extended energy range, from optical photons and thermal neutrons to the high energy reactions at the Large Hadron Collider (LHC) and in cosmic ray experiments. Particles tracked include leptons, photons, hadrons and ions. Various implementations of physics processes are offered, providing complementary or alternative modeling approaches. Moreover Geant4 provides interfaces to enable its users to interact with their application, and save their results. Visualization drivers and interfaces, graphical user interfaces and a flexible framework for persistency are included in the toolkit.

In the simulation of ^{18}F positron tracking in Timepix detector, simulation parameters and physical processes are set according to the experimental settings. The position and deposited energy of each interaction/hit in the sensitive layer after incidence of a positron are recorded. The interactions are then assigned to corresponding pixels and formed into a cluster. Simulated data are post-processed by considering the charge diffusion effect [152, 153] and energy threshold on the pixels. Timepix has one global discrimination threshold (THL) for all pixels, however its threshold energy will vary among all pixels. For every pixel the threshold energy can be shifted up or down within a small interval around the threshold energy calibrated from the THL. In the simulation, each pixel of the detector is assigned with a nonuniform energy threshold following normal distribution (mean=4 keV, variance=4 keV) to filter out the energy deposition below it.

4.2. Enhancing spatial resolution of ^{18}F positron imaging

The spatial resolution is a key property to characterize the detector performance. A beta camera is characterized by its high spatial resolution and sensitivity, which facilitates its applications in some delicate in-vivo and in-vitro experiments. Beta imaging systems with a CCD detector have spatial resolutions of a few tens of μm for several investigated radionuclides. For example, the spatial resolution of μ-Imager is reported to be 15 μm for ^{3}H imaging [69]; a lens-coupled CCD camera with a thin phosphor film placed next to the sample is estimated to have a spatial resolution of 60 μm (full width at half maximum, FWHM) for a ^{90}Y/^{90}Sr quasi-point source and 70 μm (FWHM) for a ^{99m}Tc disk source [19]; A radioluminescence microscope fitted with a CCD detector has been developed recently for ^{18}F positron imaging and has an excellent spatial resolution of 6.5 μm [64, 65]. The spatial resolution of a PSAPD detector for ^{18}F positron imaging was evaluated to be 0.4 mm (FWHM) for a line source [18].

As to CMOS detectors, ^{18}F positron imaging with a Medipix2 detector (a hybrid CMOS imaging chip) has been reported with the spatial resolution of ≈230 μm [20]. The Timepix detector, evolved from Medipix2, enables the acquisition of incidence deposited energy when working in the time-over-threshold (TOT) mode. Using acquired energy information, the spatial resolution of ^{14}C and ^{90}Sr/^{90}Y electron imaging has been reported to be improved by energy weighted centroid approximation (spatial resolution ≈79.6 μm for ^{14}C electrons and ≈27.5 μm for ^{90}Sr/^{90}Y electrons) [63, 77].

Due to consecutive inelastic interactions with atomic electrons of the detector sensitive layer, an incident beta particle may excite a number of successive pixels in the imaging plane. The energy weighted centroid approximation of each cluster (the collection of all pixels excited by one incidence) has been used as the readout position of the incident particle [63, 77]. However, it may not be effective for higher energy charged particles. The changes of energy deposition in long positron trajectories are not monotonic with their firing sequences and positrons do not necessarily deposit more energy in the first pixels fired during a track [48]. Thus, the exploration for appropriate surrogates of readout positions may enhance the spatial resolution. This study developed a data-driven method to find the primary positions of incident positrons in a Timepix detector based on a classification algorithm to improve the spatial resolution of ^{18}F positron imaging.

4.2.1. Computational modeling of positron absorption by machine learning

The incident positrons emitted from a radioactive source are scattered in multiple steps in the silicon detector before absorption or penetration. The 2D projection of a positron trajectory within the detecting layer on the pixelized imaging plane forms a 'cluster' (see Figure 4.1(b)), which may include several fired pixels. Multiple scattering is the reason for degraded spatial resolution of positron (in particular ^{18}F positrons) imaging. In order to improve the spatial resolution of an ^{18}F positron image, we propose a method, which selects the primary excited pixels from clusters (the pixels labeled with number "1" in Figure 4.1(b)). In this way, the influence of scattering can be reduced. The interactions of a positron within a silicon detector happen typically within 300 ps [154] and it is impossible to differentiate the primary pixels from other pixels with the current time resolution (≈10 ns) of Timepix. We suggest identifying the primary pixels using a classification algorithm. The classification utilizes the model learned by the training set to predict the class of testing set. The training set is built up by a Monte-Carlo simulation and includes the simulated energy and topological characteristics of successively fired pixels. The method was tested on both simulation and experimental data.

The SVM method is applied here to distinguish pixels fired by each incident positron into classes. The SVM constructs supervised learning models with associated learning algorithms that analyze data and recognize patterns. Given some training vectors $\boldsymbol{x_i} \in R^n, i = 1, \dots, l$, and an indicator vector $\boldsymbol{y} \in R^l$, the aim of SVM classification is to solve the following optimization problem [155]:

$$\min_{\boldsymbol{\omega},b,\xi} \ \frac{1}{2}\boldsymbol{\omega}^T\boldsymbol{\omega} + C\sum_{i=1}^{l}\xi_i \tag{4.1}$$

$$\text{subject to} \ \ y_i(\boldsymbol{\omega}^T\phi(\boldsymbol{x_i}) + b) \geq 1 - \xi_i, \xi_i \geq 0, i = 1, \dots, l$$

where, the vector (or the point in *n*-dimensional space) $\boldsymbol{x_i}$ contains the quantitative values of *n* features. $\boldsymbol{y_i}$ indicates the class to which the point $\boldsymbol{x_i}$ belongs. $C > 0$ is the regularization parameter; ξ_i is the variable which measures the degree of misclassification of point $\boldsymbol{x_i}$; $\boldsymbol{\omega}$ is the normal vector to the hyperplane in l-dimensional space, which maximally divides the training points, and the parameter $b/\|\omega\|$ determines the offset of the hyperplane from the origin along the normal vector $\boldsymbol{\omega}$; $\phi(\boldsymbol{x_i})$ maps $\boldsymbol{x_i}$ into a higher-dimensional space. SVM finds a linear separating hyperplane with the maximal margin in this higher dimensional space.

Due to the possible high dimensionality of the vector variable $\boldsymbol{\omega}$, the optimization problem described by above equation is usually transformed into solving its dual form problem:

$$\min_{\boldsymbol{\alpha}} \frac{1}{2}\boldsymbol{\alpha}^T Q\boldsymbol{\alpha} - \boldsymbol{e}^T\boldsymbol{\alpha} \tag{4.2}$$

$$\text{subject to } \boldsymbol{y}^T\boldsymbol{\alpha} = 0, 0 \le \alpha_i \le C, i = 1, \dots, l$$

where Q is an $l \times l$ positive semidefinite matrix, $Q_{ij} \equiv y_i y_j K(\boldsymbol{x_i}, \boldsymbol{x_j})$, and $K(\boldsymbol{x_i}, \boldsymbol{x_j}) \equiv \phi(\boldsymbol{x_i})^T \phi(\boldsymbol{x_j})$ is the kernel function. The radial basis function (RBF): $K(\boldsymbol{x_i}, \boldsymbol{x_j}) \equiv \exp\left(-\gamma \left\|\boldsymbol{x_i} - \boldsymbol{x_j}\right\|^2\right), \gamma > 0$ is chosen as the kernel function here. γ is kernel parameter. In order to realize the SVM classification, an integrated software LIBSVM is used in this study [102, 155].

The fired pixels of a cluster are classified into 4 classes in the proposed method: (1) the pixel primarily excited; (2) the second excited pixel if it exists (for clusters whose size ≥ 2 pixels); (3) the third excited pixel if it exists (for clusters whose size ≥ 3 pixels); (4) other following pixels if they exist (for clusters whose size ≥ 4 pixels). And they are labeled with class "1", "2", "3" and "4", respectively, which correspond to $y_i \in \{1, 2, 3, 4\}$ in equations 1 and 2.

Based on the observation made by the Monte-Carlo simulation and intrinsic differences among classes, 17 features of a pixel are considered for training the classification model:

(1) The number of nearest neighbors (distance ≤ 1 pixel): N_1, $N_1 \in [0, 4] \subseteq \mathbf{Z}$;
(2) The number of nearest neighbors (distance ≤ 1.5 pixels): N_2, $N_2 \in [0, 8] \subseteq \mathbf{Z}$;
(3) The relative energy E_1: the energy deposited on the pixel divided by the cluster energy (the cluster energy is the summation of deposited pixel energies belonged to a cluster);
(4) The relative energy E_2: the energy deposited on the pixel divided by the average pixel energy;
(5) The relative energy E_3: the total energy of the pixel and its neighbors (distance ≤ 1 pixel) divided by the cluster energy;
(6) The relative energy E_4: the total energy of the pixel and its neighbors (distance ≤ 1.5 pixels) divided by the cluster energy;
(7) The relative energy E_5: the total energy of the pixel and its neighbors (distance ≤ 1 pixel) divided by the average pixel energy;
(8) The relative energy E_6: the total energy of the pixel and its neighbors (distance ≤ 1.5 pixels) divided by the average pixel energy;
(9) The normalized pixel distance from the energy-weighted centroid of the cluster (normalized by cluster size);
(10) The 3-order moment of the fired pixel distribution over the pixel and its neighborhood (distance ≤ 1.5 pixels);

(11) The 3-order moment of the pixel deposited energy distribution over the pixel and its neighborhood (distance ≤ 1.5 pixels);
(12) The skewness of the fired pixel distribution over the pixel and its neighborhood (distance ≤ 1.5 pixels);
(13) The skewness of the pixel deposited energy distribution over the pixel and its neighborhood (distance ≤ 1.5 pixels);
(14) The kurtosis of the fired pixel distribution over the pixel and its neighborhood (distance ≤ 1.5 pixels);
(15) The kurtosis of the pixel deposited energy distribution over the pixel and its neighborhood (distance ≤ 1.5 pixels);
(16) The entropy of the fired pixel distribution over the pixel and its neighborhood (distance ≤ 1.5 pixels);
(17) The entropy of the pixel deposited energy distribution over the pixel and its neighborhood (distance ≤ 1.5 pixels).

The classification results are not proportional to the feature number. The classification performance may be saturated or even reduced with excessive features due to feature mutual dependence, so that the *principal component analysis* (PCA) was implemented before the learning procedure to choose the independent and principal features mostly determinant for the classifier. The principal feature sets with summed eigenvalues (of the covariance matrix of all feature sets) taking up more than 95% of total eigenvalues were selected for the learning process.

After preprocessing of the training and the testing set, the classification mainly follows 4 steps: (1) scale the training and testing set to avoid attributes in greater numeric ranges dominating those in smaller numeric ranges and avoid numerical difficulties during the calculation [102]; (2) identify the optimal parameters (C, ɣ) of radical basis function (RBF) kernel by cross validation so that the classifier can provide high accuracy for classification. (3) learn the classification model (*i.e.*, the classifier) based on the training set obtained by Monte-Carlo simulation; (4) apply the classifier to predict the classes of investigated pixels.

4.2.2. Monte-Carlo simulation for training data

The ^{18}F positron passing through and interacting with the Timepix chip is simulated by Monte-Carlo simulation using Geant4, a toolkit modeling the physical processes of particles passing through matter [151]. The training set of the proposed algorithm is built up using the simulation. A general source emitting ^{18}F positrons arbitrarily from a box region: 5 cm × 1.4 cm × 1.4 cm (H×L×W) directly on top of the detector surface in air is used. The energy of the emitted

positrons follows the theoretical ^{18}F positron energy spectrum (maximum energy E_{max}=633 keV). The general source is considered to cover a wide scenario of positron angle and energy of incidence. Other sources with different geometries and positions were tested to evaluate the robustness of the proposed algorithm for different training sets. The size of the training sets (different numbers of positron emissions) was tested to further study the stability of the classifier.

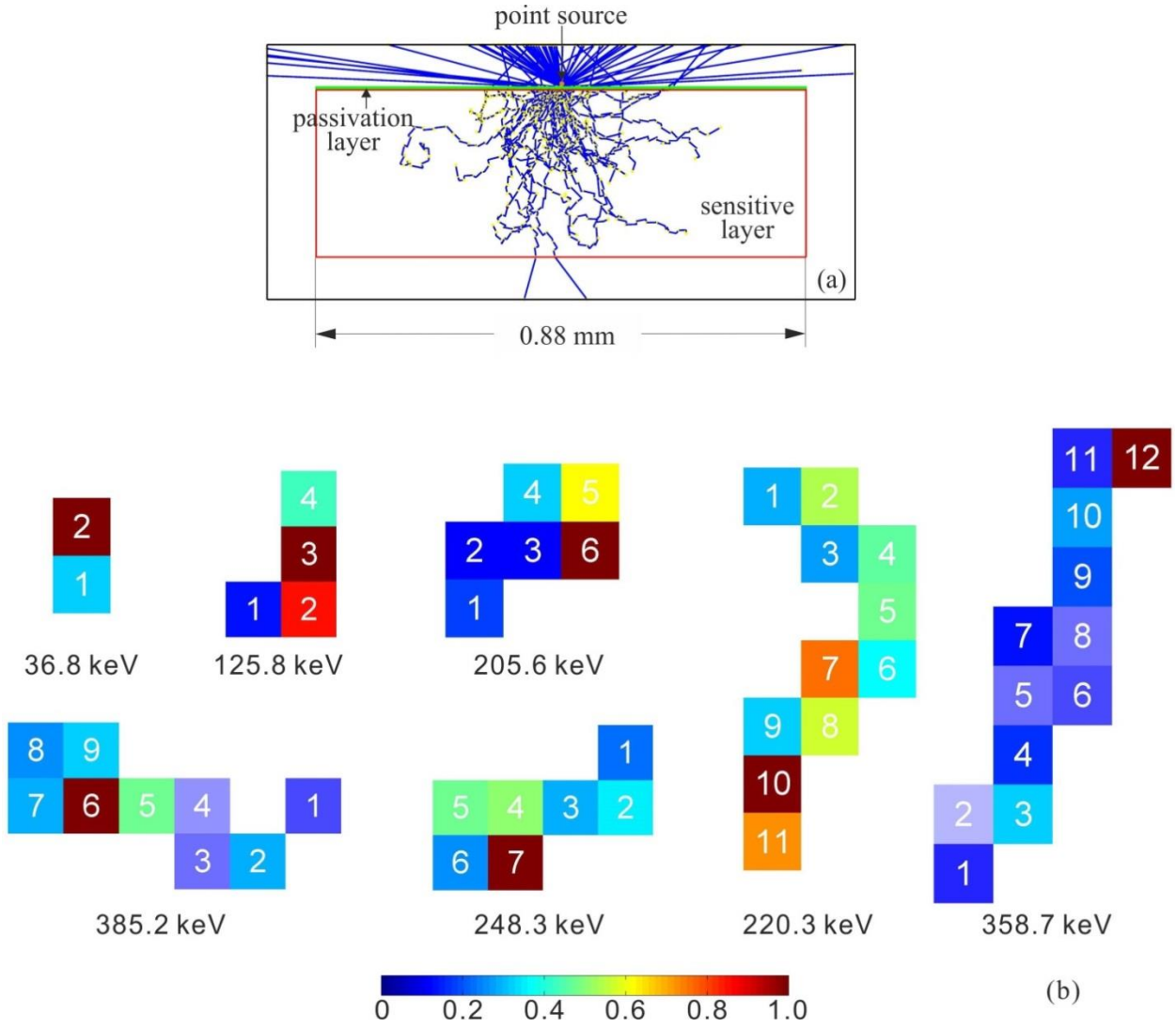

Figure 4.1. (a) The simulated positron trajectories generated by 100 positrons emitted from a specific ^{18}F point source (on the center of detector surface) in a Timepix detector; (b) Examples of simulated clusters of ^{18}F positrons. The pixel colors indicate the pixel deposited energy normalized by the corresponding maximum pixel energy within a cluster, and the numbers on the pixels represent the pixel firing sequence. The cluster energies are given beneath each cluster.

Figure 4.1(a) shows the positron trajectories from 100 ^{18}F positron emissions in the Timepix detector (only a part of the detector is shown here) simulated by Geant4. A specific source (a point source placed on the center of detector surface) is utilized here to demonstrate the positron trajectories. The sequences, positions and deposited energies of positron interactions within the detector sensitive layer were recorded by simulation. A cluster is composed of a set of successive pixels, which are the projection of the 3D particle trajectory on the 2D imaging plane [20, 77, 156]. Examples of clusters are displayed in Figure 4.1(b). The pixel colors indicate the pixel deposited energy normalized by the corresponding maximum pixel deposited energy within a cluster. The numbers labeled on the pixels represent the pixel firing sequence. The energy deposition of a positron is complicated and the energy changes along the long trajectories are not monotonic. Thus, the assumption of highest pixel energy deposition in first firing pixels by the energy weighted centroid method may be violated in some cases. Electronic noise of Timepix detection has been filtered by setting a threshold in the measurement. For the simulation, a randomly generated pixel-wise energy threshold following a Gaussian distribution is applied for consistency with measurements [157].

4.2.3. Experiments using Timepix for testing data

To estimate the spatial resolution of ^{18}F positron imaging, measurements were prepared using the Timepix positron camera (Figure 4.2 (a)) working in TOT mode. The bias voltage and sampling rate were chosen to be 100 V (the sensitive layer is over-depleted) and 9.6 MHz, respectively.

The absorbing edge method (AEM) was adopted to assess the spatial resolution [20, 63, 77]. As shown in Figure 4.2(b), a 300 μm thick aluminum plate covered half of the detector surface. A 10 μl droplet of [^{18}F]FDG (activity: 30 Mbq/ml) was pipetted on the Mylar placed 5 cm above the aluminum plate. Totally 36000 frames of 0.2 s (frame width) were acquired (about 2 hours data acquisition). The short frame width effectively reduced the overlap of clusters. The edge response function was determined by averaging 100 columns perpendicular to the edge of the positron image and the corresponding line spread function is derived by differentiation of edge response function. The spatial resolution was assessed by the FWHM of the line spread function. The maximum value of the line spread function was acquired by a parabolic fit using the peak point and its two nearest neighboring points respectively. FWHM was then determined by linear interpolation between adjacent pixels at half the maximum value of the response function. For the assessment of spatial resolution, the values assigned to the pixels in a positron image can be the cluster number or deposited energy.

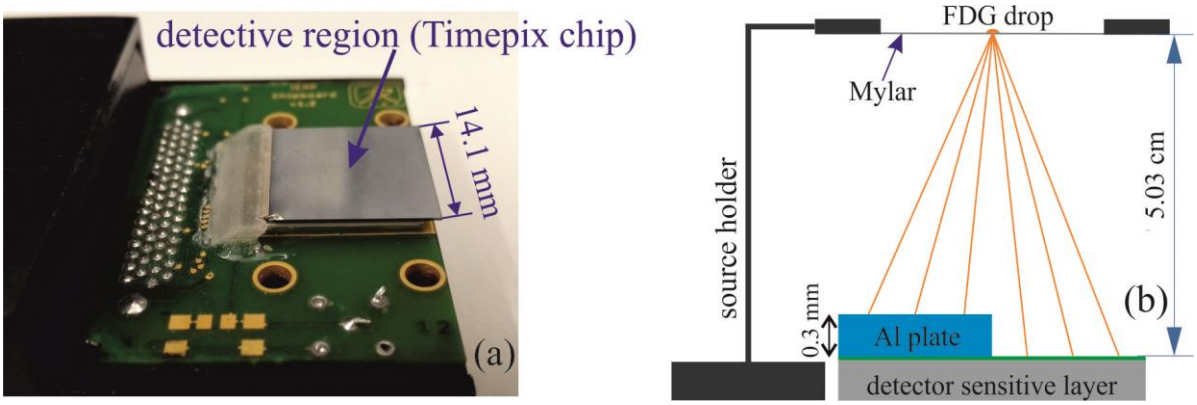

Figure 4.2. (a) the positron (beta) camera; (b) the sketch of the measurement of edge profile for spatial resolution.

The parallel alignment of the edge (edge parallel with the detector pixel columns) was evaluated on the acquired images [157]. Only the edge with parallel alignment (error < 0.5 degree) was considered for the estimation of spatial resolution (5 qualified edges selected). To determine the real energy deposited in each pixel, the energy calibration of the TOT signal was performed [158]. Due to fabrication limitations, the boundary pixels usually have larger dimensions than the other pixels, so that stronger signals are recorded there. Therefore, three rows and columns in the neighborhood of boundaries were not considered in the classification. The camera contains 10 defective pixels. They were removed from the data by preprocessing. A negligible influence of background was observed during the whole measurement: 3.1×10^{-6} cps/pixel and 1.3×10^{-4} keV/s/pixel in TOT mode.

4.2.4. Classification verification and classification error assessment

The feature spectra (*i.e.*, the feature distribution function) were compared with the measured ones to verify that the simulated features are suitable to serve as training data. The t-test was applied on simulated and measured spectra to estimate their similarities.

The classifier may fail for some clusters (*classifier failure*). They are explicitly classified with no primary pixel or more than one primary pixel. These clusters can be excluded before spatial resolution evaluation, leading to sensitivity loss. Instead, the sensitivity loss can be compensated by introducing the energy weighted centroid approximation for these clusters. However, the *sensitivity compensation* will sacrifice some enhancement of spatial resolution.

Misclassification may happen during the procedure and false primary pixels may be identified in

real measurements. Using the simulated data as testing set (the actual pixel firing sequences within clusters are known), the classification accuracies are assessed on cluster sets with different sizes: 2 pixels, 3 pixels, 4 pixels, 5 pixels and more pixels, respectively. For each cluster set, the accuracies of class j (j=1, 2, 3) pixel predicted as primary pixel are estimated. The second pixels or the third pixels are mixed in the primary pixels to some extent and their influences on spatial resolution are evaluated.

4.2.5. Imaging of a leaf sample uptake with [^{18}F]FDG

To test the application of the proposed algorithm, we applied it on the imaging of a leaf sample with fine veins. The image of a parthenocissus tricuspidata leaf with [^{18}F]FDG uptake was acquired with the positron camera. The acquired positron image was then processed with the proposed method to examine its performance on obtaining an image of the leaf vein network. The stem beneath the fresh leaf was immersed in a water solution of [^{18}F]FDG tracer (activities: 10MBq/ml) for 2 hours to take up tracer. The leaf was washed 3 times after stem immersion to eliminate the possible tracer contamination on the leaf surface. Then a part of leaf sample was put directly on top of the detector for measurement in the TOT mode for 1 hour (frame width = 0.2 s).

Afterwards, the same sample was transferred to an autoradiography cassette for storage phosphor screen (Fuji phosphor imaging plate, a film-like radiation image sensor) exposure of 6 hours for phosphor image (as the reference). The screen provides a spatial resolution of 100 μm or lower, and high image contrast. Then it was scanned by a CR 35 Bio Image Plate Scanner (Duerr Medical GmbH) for 10 min with 25 μm pixel resolution. An optical image was obtained as another reference by scanning the leaf with the scanner (EPSON Perfection 1650) at 1200 dpi.

5. Validation and applications of computational modeling in investigations of tumor metabolism

Molecular imaging can characterize tumor phenotypes by assessing the related metabolism of certain substrates. However, the interpretation of the substrate turnover in terms of a pathophysiological understanding is not straightforward and only semiquantitative. The model proposed in chapter 3 sets up a platform to explore the quantitative relationship between tumor metabolism and pathophysiological factors (such as expression levels of GLUT, MCT1, MCT4, HK, HIF-1 and microvessel distribution). The proposed model is validated in this chapter by comparing the simulation data with *in vivo* and *in vitro* literature data, and is then applied in assessing the quantitative relationship by analyzing parameters: the sensitivities of substrate with respect to the variations of pathophysiological factors and the correlation coefficients between the substrate concentrations and pathophysiological factor levels. This computational modeling may assist the generation of hypotheses to bridge the discrepancy between the tumor metabolism and the functions of transporters and enzymes. It has the potential to accelerate the development of multi-modal imaging strategies for assessment of tumor phenotypes.

5.1. Implementation and validation of HIF-independent model

The model independent of HIF-1 is implemented on a tumor tissue phantom. Figure 5.1 displays an example of the model implementation. The distributions of the parameters are investigated, including O_2 tensions, extra- and intracellular glucose concentrations, extra- and intracellular lactate levels, pH, CO_2 tensions and HCO_3^- concentrations. They are simulated by the proposed model for a tissue phantom with a mean intervascular distance of 160 µm. The black arrows point to the average values of the parameters investigated over the displayed simulation results. The concentrations (or partial pressures, respectively) of these parameters as a function of the distance up to 170 µm from a selected vessel (distribution-to-distance curve) are illustrated in Figure 5.2. Meanwhile, the indirect model verification is performed on the simulated parameter distributions by comparing with the *in vivo* and *in vitro* data reported in the literature in the following paragraphs.

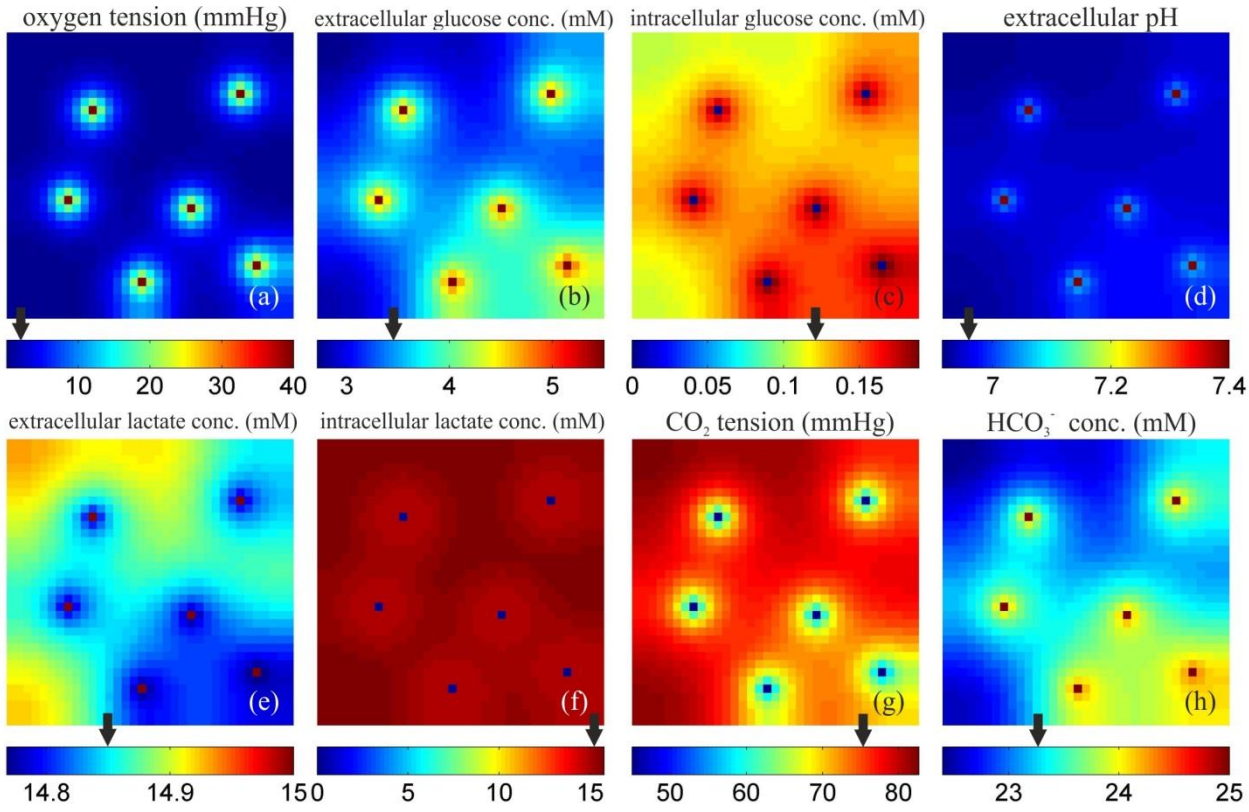

Figure 5.1. Substrate distribution maps of a tumor tissue phantom with an intervascular distance of 160 µm. Figure (a) to (i) are maps of O_2 tension (mmHg), extra- and intracellular glucose concentration (mM), extracellular pH, extra- and intracellular lactate concentration (mM), CO_2

tension (mmHg) and HCO_3^- concentration (mM), respectively. The black arrow points to the average value of each parameter. conc. = concentration.

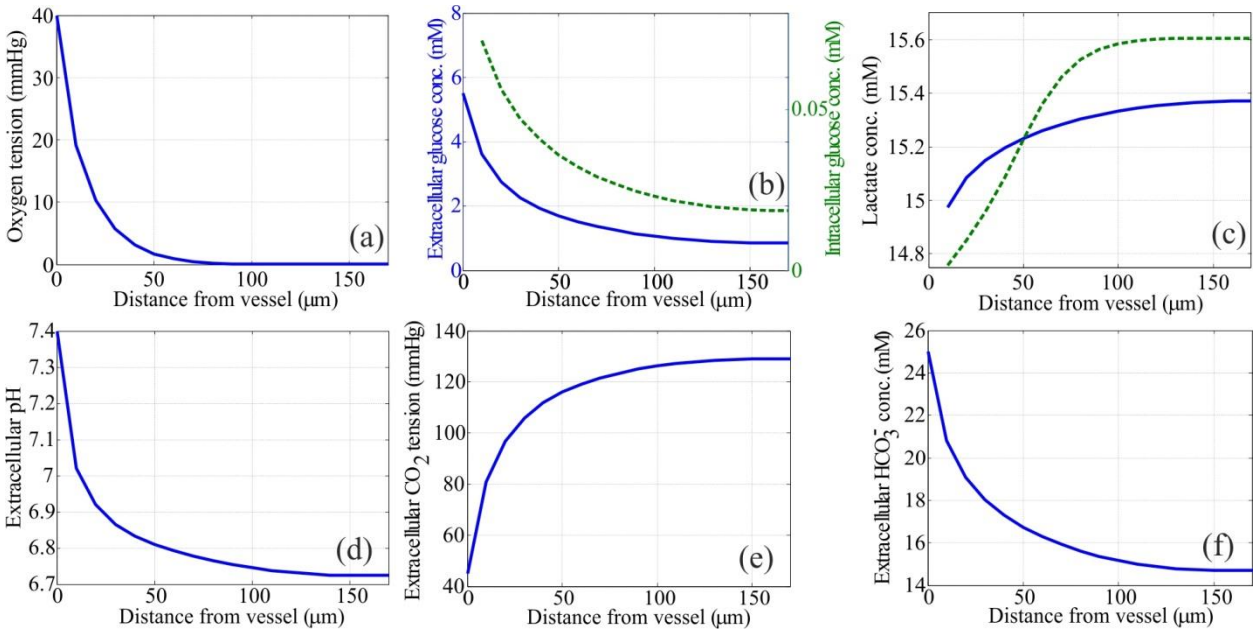

Figure 5.2. Substrate distribution curves as a function of distance from a single vessel. Parameter distributions: oxygen tension (figure a), extra- (blue solid curve) and intracellular (green dash curve) glucose concentrations (figure b), extra- (blue solid curve) and intracellular (green dash curve) lactate levels (figure c), extracellular pH (figure d), extracellular CO_2 tension (figure e) and extracellular HCO_3^- concentrations (figure f). conc. = concentration

As displayed in Figure 5.2a, the oxygen tension pO_2 decreases monotonically as the distance from the vessel increases, and the tissue reaches hypoxic levels (pO_2<2.5 mmHg [80]) at 45 μm from the vessel. The region farthest away (>70 μm) from the vessel becomes anoxic (pO_2<0.5 mmHg [81]). The average pO_2 over the whole phantom, with a 160 μm mean intervascular distance is 3.3 mmHg (Figure 5.1a), which is within the range of pO_2 Eppendorf data: 0-60 mmHg for tumors (the measured tumor pO_2 values) [159, 160]. The average pO2 (over the phantom) under different pathophysiological conditions assumed in this study varies from 0.8 to 34 mmHg, which means all simulated average pO_2 can fall in the range of Eppendorf data.

Figure 5.1e & f show the distribution of extra- and intracellular lactate levels and Figure 5.2c exhibits their concentrations as functions of the distance from the vessel. A higher intracellular lactate concentration than the extracellular lactate concentration was observed in hypoxic regions, which promotes lactate export from the cells. In normoxic regions, extracellular lactate is higher

than that of intracellular lactate, and interstitial lactate tends to be imported into the cells for oxidation. The "crossing point" of the extracellular and intracellular lactate curves occurs at 50 μm from the vessel, which is almost the boundary between hypoxia and normoxia. The mean extra- and intracellular lactate concentrations over the displayed tissue phantom are 14.9 and 15.3 mM, respectively. The experimental lactic acid content in rat tumor tissue using a millipore chamber was shown to be 17.5 mM [133]. The mean concentration of extracellular lactate in a cancer of the uterine cervix was 15 mM [21].

The distribution of extracellular pH is shown in Figure 5.1d and its distribution-to-distance curve is plotted in Figure 5.2d. The pH in this simulation decreases from 7.4 within the vessel to 6.75 at a distance of 170 μm. The average pH over the simulated tissue phantom is 6.95. In tumors *in vivo*, the extracellular pH normally ranges from 6.6 to 7.1 [161, 162].

The extracellular CO_2 tension (pCO_2) increases from 45 mmHg (blood) to 127 mmHg at a distance of 170 μm away from the vessel as shown in Figure 5.2e. The latter pCO_2 is up to 2.8 times that of the plasma pCO_2 in the simulation. The simulated average pCO_2 is 74 mmHg across the displayed tissue phantom (Figure 5.1g), which is 1.65 times that of plasma pCO_2. For tumors *in vivo*, the pCO_2 was reported to be more than twice as high as that in plasma [134]. The extracellular HCO_3^- levels decrease accordingly from 25 mM (blood) to 14.7 mM (Figure 5.2f).

The Henderson-Hasselbalch equation is an empirical equation used for estimating the pH in the bicarbonate buffering system [134, 162]:

$$pH = pK_a + \log_{10}\left(\frac{[HCO_3^-]}{S_{CO_2} \cdot pCO_2}\right) \tag{5.1}$$

where pK_a is the co-logarithm of the acid dissociation constant of carbonic acid, $pK_a \approx 6.15$, S_{CO_2} is the Henry's law solubility constant of carbon dioxide ($S_{CO_2} \approx 0.03$). We compared our simulation results with the results predicted by the Henderson-Hasselbalch equation. The distribution-to-distance curves of the simulated pH and the calculated pH values using the Henderson-Hasselbalch equation are shown in Figure 5.3. They generally follow the same tendency by paired t-test ($P<0.05$, $n=17$). The average pH obtained directly from the simulation is 6.84, and the average pH calculated by the Henderson-Hasselbalch equation is 6.86. The mean and the max difference of the two pH curves are 0.3% and 0.7% of the average pH from Henderson-Hasselbalch equation, respectively.

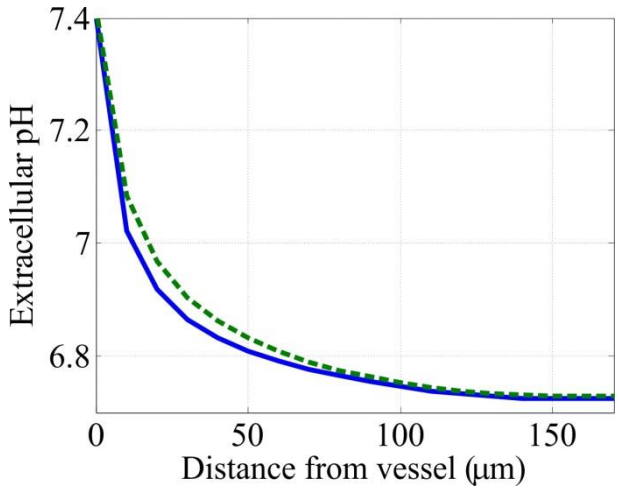

Figure 5.3. The curve (extracellular pH as a function of the distance from the vessel) comparison between pH values obtained by direct simulation (blue solid curve) and pH calculated by the Henderson-Hasselbalch equation (green dash curve).

5.2. Implementation of HIF-1 driven model

As HIF-1 has been reported to influence the tumor metabolism by regulating the expressions of certain enzymes and transporters, a developed model integrating HIF-1 has been put forward in section 3.1.6. The local expressions of GLUT, HK and MCT4 are assumed negatively correlated with HIF-1 level, while the local MCT1 expression is determined by HIF-1 level in a positive way. The 1D oxygen and HIF-1 distribution (oxygen-dependent) as the function of the distance from the vessel are plotted by blue solid and green dash curves in Figure 5.4(a), respectively. HIF-1 reaches and maintains the maximum since 50 μm from the vessel. Figure 5.4(b)-(h) show the 1D distributions of extracellular pH, extra- and intra-cellular glucose concentration, extra- and intra-cellular lactate concentration, extracellular HCO_3^- concentration and CO_2 tension based on the model driven by HIF-1. The overexpression factors of GLUT, HK, MCT1 and MCT4 are all supposed to be 4. Meanwhile, the substrate distributions obtained from the HIF-1 driven model (blue solid curves) are compared those from the HIF-1 independent model (green dash curve) in Figure 5.4. More lactic acid is produced (22.1% and 29.4% more extra- and intra-cellular lactate are produced and pH decreases 3.5% on average over the curves of Figure 5.4) and more glucose (47.0% and 51.0% more extra- and intra-cellular glucose are consumed) is consumed with the promotion of HIF-1. Due to the accumulation of protons and the bicarbonate buffering system, the CO_2 tension is forced to rise (25.9% CO_2 tension is raised) and HCO_3^- concentration decreases (26.6% decrease) accordingly in the HIF-1 driven model.

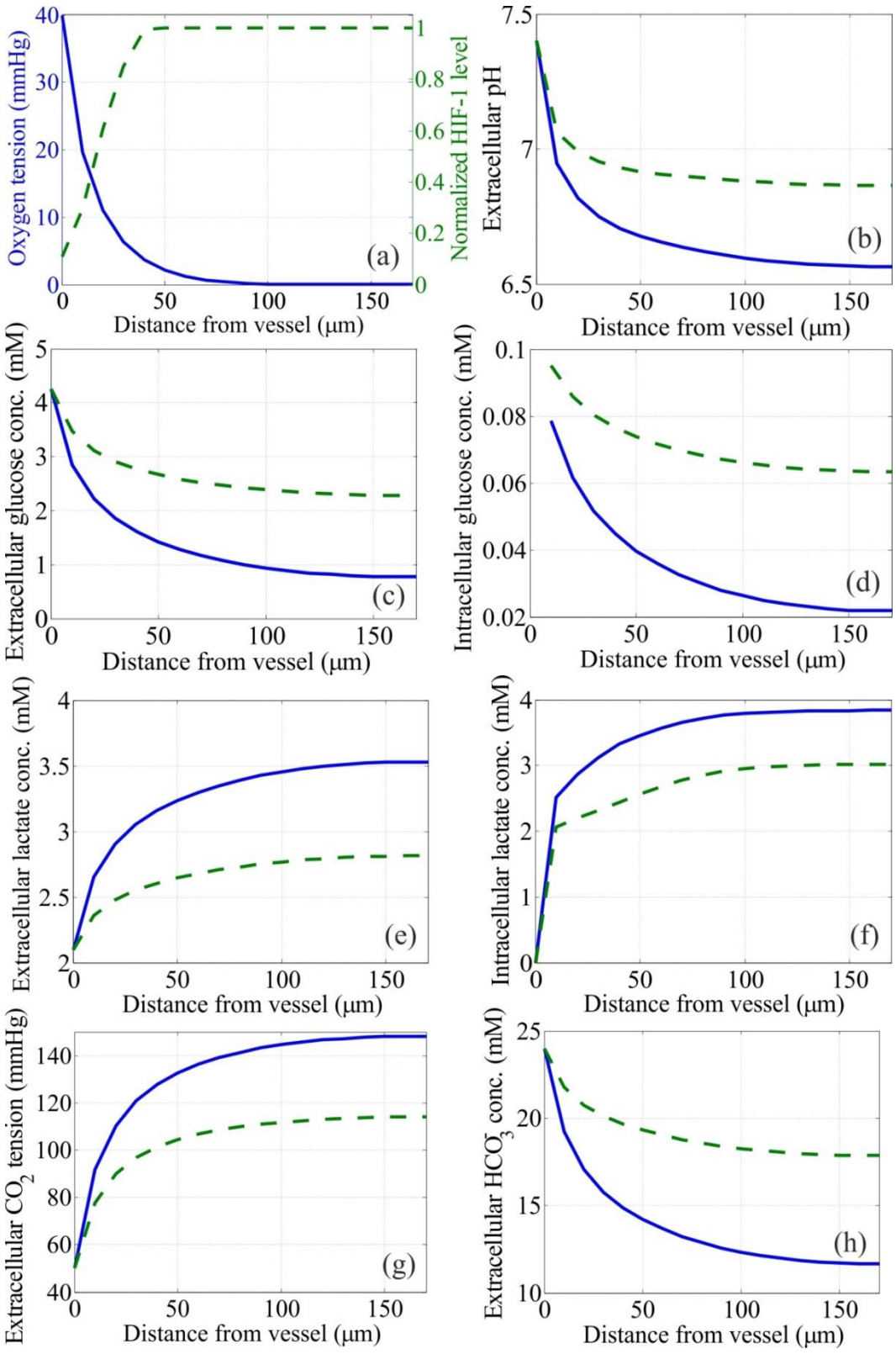
Oxygen tension (mmHg)
Normalized HIF-1 level
Distance from vessel (μm)
(a)
Extracellular pH
(b)
Extracellular glucose conc. (mM)
(c)
Intracellular glucose conc. (mM)
(d)
Extracellular lactate conc. (mM)
(e)
Intracellular lactate conc. (mM)
(f)
Extracellular CO_2 tension (mmHg)
(g)
Extracellular HCO_3^- conc. (mM)
(h)

Figure 5.4. The influence of HIF-1 on the substrate distributions. Figure (a) represents the 1D oxygen tension (blue solid curve) and corresponding HIF-1 (green dash curve) as the function of distance from the vessel. Figures (b) to (h) exhibit the extracellular pH, extra- and intra-cellular glucose concentration, extra- and intra-cellular lactate concentration, the extracellular HCO_3^- concentration and CO_2 tension as the functions of the distance from the vessel, respectively. The substrate concentrations emulated from the model driven by HIF-1 (blue solid curves in figures (b) to (h)) are compared with those from the model independent of HIF-1 level (green dash curves in figures (b) to (h)).

5.3. Implementation of FDG uptake model

The FDG uptake model driven by HIF-1 is implemented on tumor tissue phantoms with different microvessel densities, and expressions of GLUT and HK. An example of model implementation is shown Figure 5.5, where the phantom (1×1 mm^2, 100×100 pixels) has a microvessel density of 40 vessels/mm^2, and 3-fold maximum overexpressions for both GLUT and HK ($k_{GLUT} = k_{HK} = 3$). Figures (a) and (b) are the maps of oxygen (unit: mmHg) and normalized HIF-1 distributions, respectively. Figures (c) to (e) present the distributions of extra-, intra-cellular glucose (unit: mM) and glucose metabolic rate (unit: μM/s), respectively. The corresponding extra-, intra-cellular FDG (unit: mM) and FDG trapping rate (unit: μM/s) are exhibited in figures (f) to (h), respectively.

The average oxygen tension over the selected phantom is 3.5 mmHg, which fall in the range of published tumor pO2 values (Eppendorf data): 0-60 mmHg [159, 160]. Based on the proposed model, the average oxygen tensions simulated in different pathophysiological conditions vary from 1.6 to 23.5 mmHg, which also falls into the range of Eppendorf data. The average extracellular glucose concentration is 2.9 mM, which is much higher than the intracellular glucose concentration (0.02 mM on average). The extracellular glucose in tumor tissue has been reported within the range of 0.5-3.7 mM for several types of tumor cells [163].

In addition, the average values for normalized HIF-1, glucose metabolic rate, extra- ad intracellular FDG concentration and FDG trapping rate are 0.26, 0.75 μM/s, 4.6×10^{-9} mM, 7.0×10^{-11} mM and 2.8×10^{-8} μM/s, respectively. They are marked by black arrows pointing to the colorbars of each map in Figure 5.5.

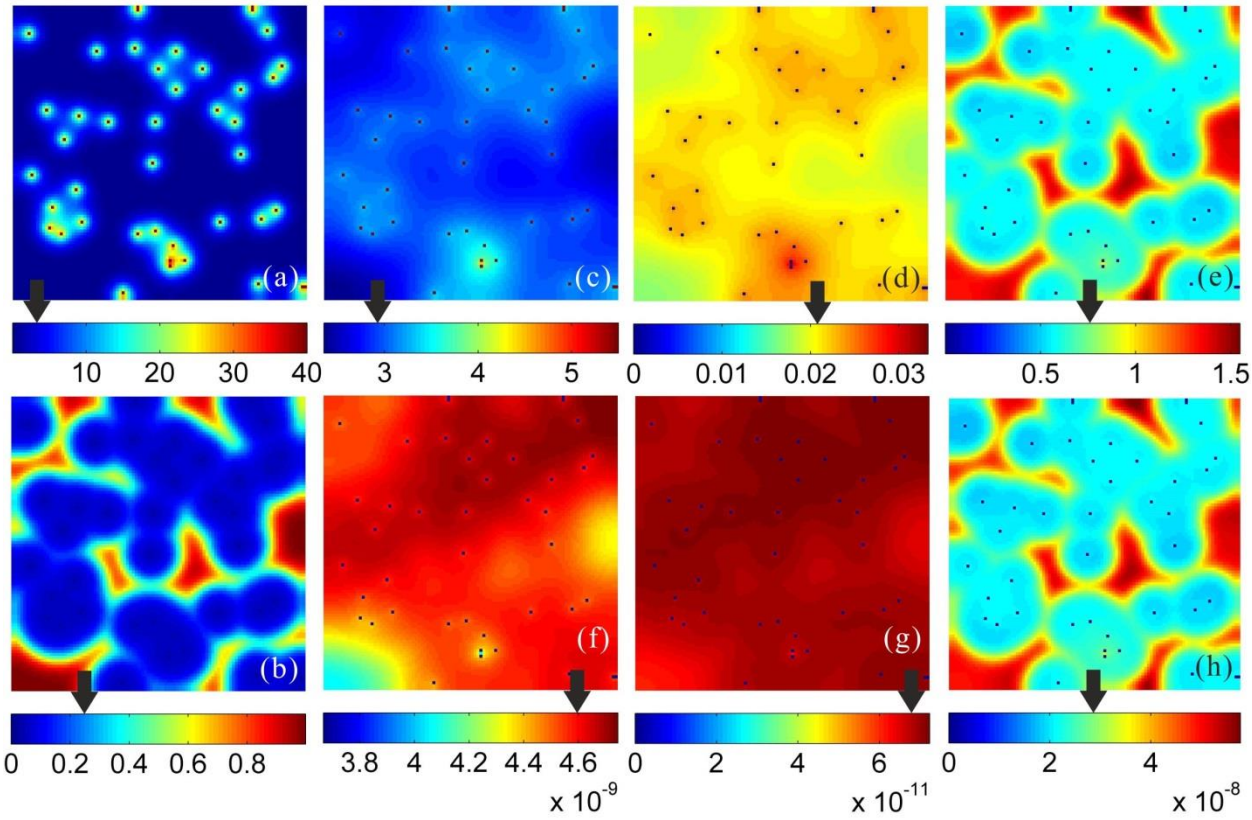

Figure 5.5. Substrate concentration maps. Figures (a) and (b) are the 2D oxygen (mmHg) and normalized HIF-1 distributions. Figures (c) to (h) present the 2D distributions of extra-, intra-cellular glucose (mM) and glucose metabolic rate (μM/s), and extra-, intra-cellular FDG (mM) and FDG trapping rate (μM/s), respectively. The average values of these parameters are marked by black arrows pointing to the colorbars of each map.

Figure 5.6(a) shows the simulated TACs (blue curves) of tumor tissue phantoms with different vascular densities (20-200 vessels/mm^2). They are compared with the measured curve (red curve), which shares the same plasma input function displayed in Figure 5.6(b). The tissue-to-blood (T/B) ratios for simulated TACs change from 1.4 to 4.6 as compared to 4.4 for measured TAC. Using other parameters (such as higher vascular density) promoting the FDG retention, the T/B can reach 6.5 in this model. The T/B measured in clinical and preclinical studies have been reported within the range of 1.3-17.2 for different types of tumors [164, 165].

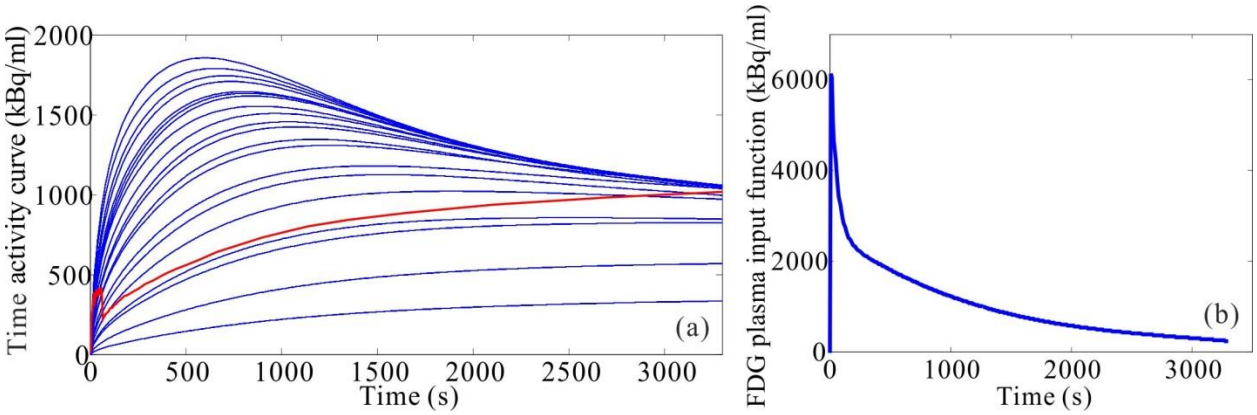

Figure 5.6. (a) simulated TACs (blue curve) under different vascular densities (20-200 vessels/mm^2) as a comparison with measured TAC (red curve) using the plasma input function displayed in figure (b).

5.4. Results of the HIF-1 independent model

5.4.1. The influences of pathophysiological conditions on substrate metabolism

The substrate metabolism is affected by pathophysiological conditions. Thus, the influences of pathophysiological parameters: the expressions of GLUT, HK, MCT1 and MCT4, and the mean intervascular distance on the substrate concentrations are quantitatively investigated for the HIF-1 independent model. Figure 5.7 illustrates the average concentrations of glucose and lactate, and the extracellular pH in relation to the adaption of V_{max} of GLUT and HK, and the adaption of mean intervascular distance. Each curve plots the parameter changes with regard to alterations of V_{max} for the tissue phantoms whose microvascular distributions have same mean intervascular distance. The different colors of the curves represent varying mean intervascular distances (from 60 to 180 μm) of the simulated tissue phantoms. Here, the glucose and lactate concentrations are the sum of extra- and intracellular concentrations. The glucose concentration and extracellular pH both decrease as the V_{max} values of GLUT and HK increase, whereas lactate concentration increases with higher V_{max}. On the other hand, the glucose concentrations and extracellular pH increase as the mean intervascular distances decrease (*i.e.*, when microvascular density increases). In contrast, the concentration of lactate drops with increasing microvascular density.

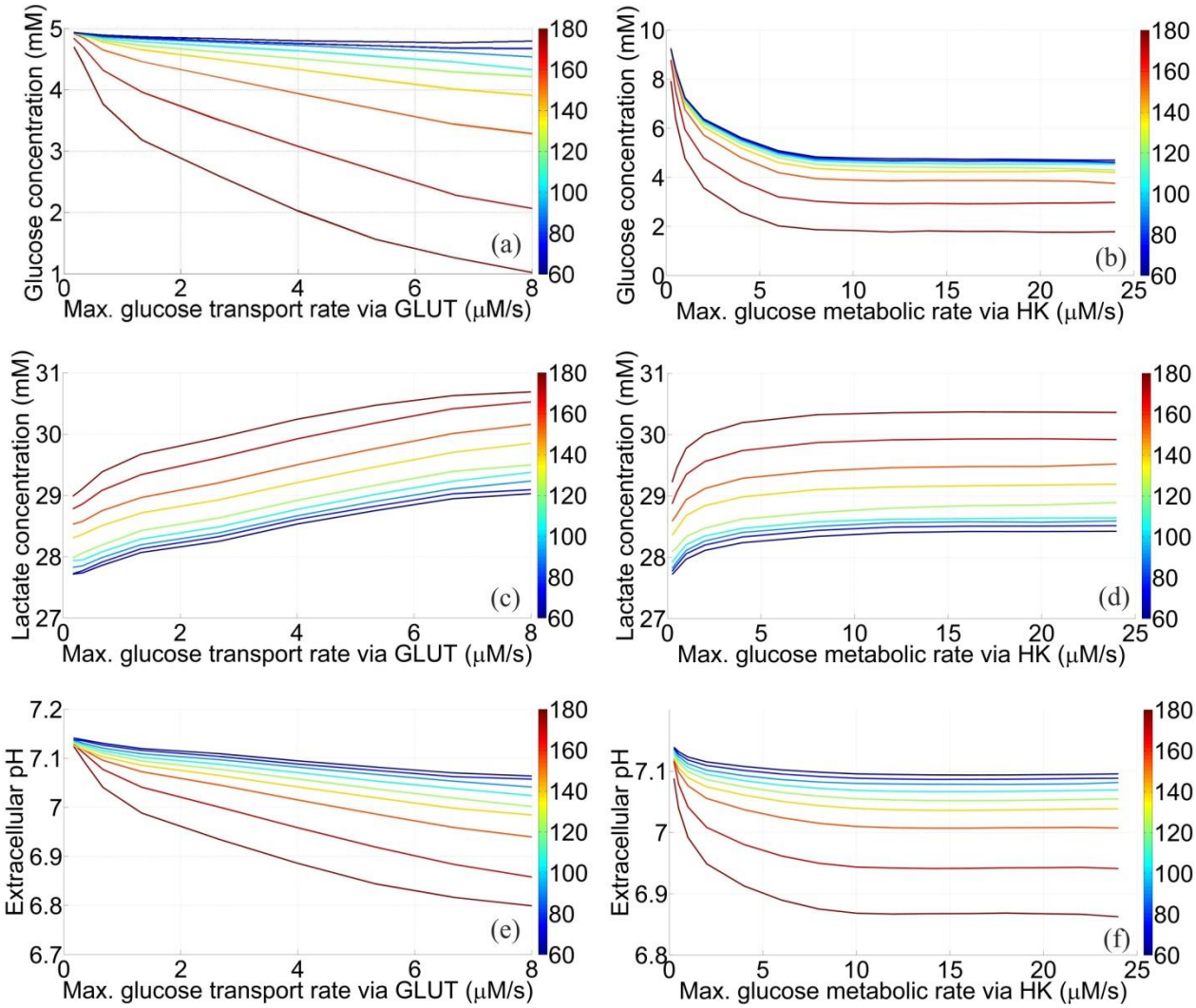

Figure 5.7. The response curves of glucose and lactate concentrations and extracellular pH to different $V_{max,\ GLUT}$, $V_{max,\ HK}$ and intervascular distances. Each curve has a certain intervascular distance (60 to 180 μm) which is color-coded. The color blue indicates a short intervascular distance; red corresponds to a larger intervascular distance.

In addition to the influence of GLUT and HK, lactate is also sensitive to MCT1 and MCT4. Figure 5.8 displays the average concentrations of lactate in relation to the adaption of V_{max} of MCT1 and MCT4, and the adaption of mean intervascular distance. Lactate concentration rises with the increase of V_{max} values of MCT1 especially for tissue phantoms at small mean intervascular distances. In an opposite way, lactate concentration diminishes with V_{max} values of MCT4 increase, and the tendency is more obvious for tissue phantoms at large mean intervascular distances.

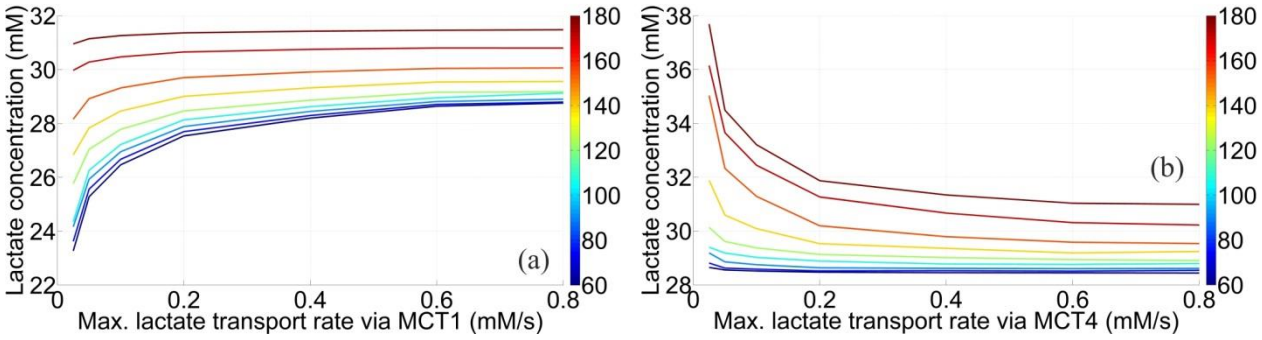

Figure 5.8. The response curves of the lactate concentration to different $V_{\text{max, MCT1}}$, $V_{\text{max, MCT4}}$ and intervascular distances. Each color-coded curve represents a selected intervascular distance (60 to 180 μm). Color transition from blue to red corresponds to an enlargement of intervascular distances.

5.4.2. The quantitative relationships between substrate metabolism and tumor phenotypes

The quantitative relationships between tumor metabolism and phenotypes (*i.e.* pathophysiological conditions) are characterized mainly by two parameters: the response sensitivity and the correlation coefficient. The response sensitivity to V_{max} values of GLUT, HK, MCT1 and MCT4 is estimated using equation $S = \Delta C/\Delta V_{max}$. The response sensitivities of glucose and lactate levels and extracellular pH to V_{max} of GLUT, HK, are displayed in Figure 5.9a-c as a function of mean intervascular distance. The errorbars of each curve point attributable to tissue phantom heterogeneities are exhibited in Figure 5.9. Moreover, the main results from the sensitivity analysis are compared with experimental findings. The absolute sensitivities of glucose, lactate and extracellular pH to V_{max} of HK and GLUT all increase with enlarging mean intervascular distance. The response sensitivities of lactate to V_{max} of MCT1 and MCT4 are presented in Figure 5.9d as a function of the mean intervascular distance. A negative influence was observed as to MCT1, indicating that lactate concentration of more oxygenated phantoms is more sensitive to MCT1 expression. While, the absolute sensitivity of lactate to V_{max} of MCT4 is positively influenced by mean intervascular distance, which implies the lactate concentration drops more steeply with increased MCT4 expression as to more hypoxic phantoms.

The overall sensitivity (average over different microvascular distributions/microvessel densities) of glucose and lactate concentrations and extracellular pH in response to V_{max} of GLUT and HK is listed in Table 5.1. Glucose is more sensitive to HK than GLUT (≈ 25% higher sensitivity), while GLUT has a 4.5-fold higher substrate sensitivity than HK for lactate and extracellular pH.

Although GLUT and HK are both functional in regulating glucose concentration, GLUT exerts a more dominant control on glycolytic flux (lactic acid production) than HK, which is consistent with the reported experimental results using cancer cells [138]. Extracellular pH shows almost no sensitivity to the expressions of MCT1 (S_{pH}=-0.001 s/mM) and MCT4 (S_{pH}=0.005 s/mM). The glucose and the lactate sensitivities (in response to the adaption of a certain V_{max}) are compared by t-test and the test results imply that the two sensitivities have no significant similarities.

The response sensitivity to the mean intervascular distance is estimated using equation $S_v = \Delta C/\Delta D_v$. The overall sensitivity to the mean intervascular distance (average of different enzyme and transporter expressions) is listed in Table 5.1.

Table 5.1. The average glucose, lactate and pH sensitivities (S_G, S_L and S_{pH}, respectively) to alterations of V_{max} of enzyme and transporters, and mean intervascular distance

	S_G*	S_L*	S_{pH}*
GLUT	-114.1 s	142.9 s	-14.2 s/mM
HK	-143.5 s	30.5 s	-3.0 s/mM
MCT1	≈0**	3.1 s	-0.001 s/mM
MCT4	≈0**	-2.1 s	0.005 s/mM
Mean intervascular distance	-0.02 mM/μm	0.14 mM/μm	-0.001 /μm

* S_G, S_L and S_{pH} represent the average glucose, lactate and extracellular pH sensitivities in response to the changes of V_{max} of GLUT, HK, MCT1, MCT4 or mean intervascular distance, respectively.

** The glucose metabolism is not dependent on the expressions of MCT1 and MCT4 based on the proposed model, so glucose sensitivity in response to changes of $V_{max,\ MCT1}$ and $V_{max,\ MCT4}$ equals to zero.

The average correlation coefficients between substrate concentrations and V_{max} of GLUT, HK, MCT1 and MCT4 (average of different microvascular distributions), and between substrate concentrations and mean intervascular distance (mean values over different enzyme and transporter expressions) are presented in Table 5.2. The substrate concentrations correlated better with V_{max} of GLUT (r=-0.97, p=0.0005) than with that of HK (r=-0.69, p=0.017). Lactate concentration has a relatively strong correlation with MCT1 (r=0.75, p=0.05) and a weak correlation with MCT4 (r=-0.64, p=0.13). In-vitro studies on tumor, heart and muscle tissues have reported a correlation between lactate concentration and MCT expression [115, 120]. Extracellular pH shows almost no correlation with MCT1 (r=-0.18, p=0.64) and MCT4 (r=0.15, p=0.39), a finding which is in line with the results reported for extracellular pH not primarily being attributed to lactate or the transport through MCTs within the tumor [42]. Moreover, the

substrate concentration shows a strong dependence on intervascular distance. A correlation between substrate concentration and tumor vasculature has been documented earlier [111, 166].

Table 5.2. The average correlation coefficients between substrate concentration (conc.), extracellular pH (pH_e), and V_{max} of enzyme and transporter expression and mean intervascular distance

	Glucose conc.	Lactate conc.	pH_e
V_{max} of GLUT	-0.97	0.97	-0.98
V_{max} of HK	-0.69	0.69	-0.70
V_{max} of MCT1	≈0*	0.75	-0.18
V_{max} of MCT4	≈0*	-0.64	0.15
Mean intervascular distance	-0.81	0.92	-0.88

* The glucose concentration is not correlated with $V_{max,\ MCT1}$ and $V_{max,\ MCT4}$ because the glucose metabolism does not depend on the expressions of MCT1 and MCT4 based on proposed model.

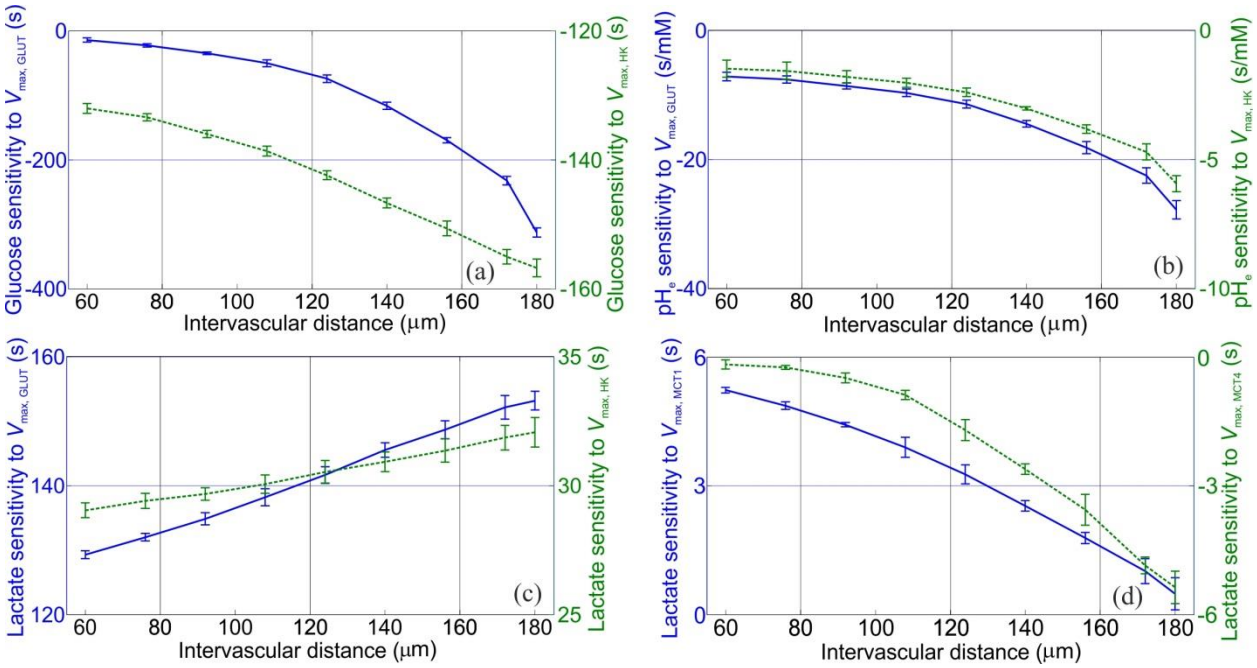

Figure 5.9. (a) Sensitivity of glucose in response to alterations of the V_{max} of GLUT (blue solid curve) and HK (green dash curve) as a function of the mean intervascular distance; (b) Sensitivity of extracellular pH in response to changes of V_{max} of GLUT (blue solid curve) and HK (green dash curve) as a function of mean intervascular distance; (c) Sensitivity of lactate to changes of V_{max} of GLUT (blue solid curve) and HK (green dash curve) as a function of mean intervascular distance; (d) Sensitivity of lactate to alterations of V_{max} of MCT1 (blue solid curve)

and MCT4 (green dash curve) as a function of mean intervascular distance. The error bars are given on each curve.

5.4.3. The influence of some parameters on the simulation

In the section, the influences of matrix size, plasma oxygen tension and the phantom pixel size on the simulation are investigated for the HIF-1 independent model. The matrix size of the tessellated phantom is selected by compromising the computational time and the representativeness of the results. Some tests of the influences of matrix size on the modeling results are performed. Three different matrix sizes 35×35, 50×50 and 100×100 are tested here. For the phantoms with same parameters (except matrix size), it is found that the matrix size weakly influence the results including the average substrate concentrations and substrate sensitivities for the investigated matrix sizes. The differences of results caused by different matrix sizes are less than 5% on average as observed in the Figure 5.10. Figure 5.10(a)-(c) presents the curves of glucose and lactate concentrations and extracellular pH as the function of HK expression. The curves are generated by the models implemented on the tissue phantoms with different matrix sizes and microvessel densities (MVDs) (40, 200, 400 vessels/mm^2), respectively. The phantom heterogeneity will influence the simulation results. However, it is largely reduced by averaging 20 repeated simulations to obtain each curve point in the Figure 5.10. Meanwhile, the number of iterations for result convergence is dependent on the matrix sizes. The dependences of iterations on matrix size and MVD are presented in figure Figure 5.10(d). The iteration decreases with MVD due to reduced phantom heterogeneity, while it generally increases with the matrix size. Therefore considering the matrix size and the area for iteration, the phantom of 100×100 matrix size is estimated to cost at least 10 times computation time more than the phantom of 35×35 matrix size.

The substrate sensitivities to the plasma pO_2 are also analyzed here. Based on the proposed model, the glucose concentration is not dependent on the oxygen tension, without considering the oxygen regulation on transporters and metabolic enzymes. So that the sensitivity of glucose concentration on plasma pO_2 is 0, as shown in Figure 5.11(a). While the lactate concentration and extracellular pH are sensitive to plasma pO_2, as displayed in Figure 5.11(b) and (c). The simulations are implemented on the phantoms with low, medium and high MVDs (40, 200, 400 vessels/mm^2) respectively. The sensitivities of glucose, lactate and pH are displayed in

Table 5.3. The absolute sensitivities of lactate and extracellular pH decrease with the MVD.

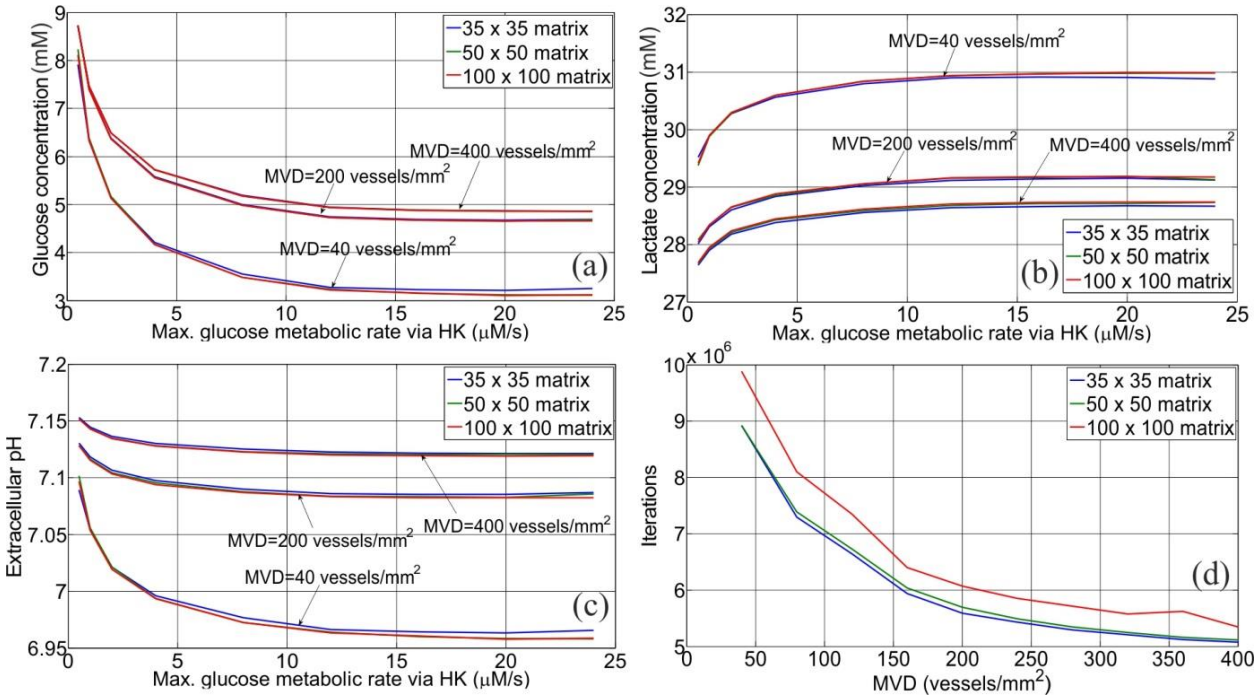

Figure 5.10. (a)-(c) Influence of matrix size (35×35 matrix, 50×50 matrix and 100×100 matrix) on the substrate concentrations as a function of MVD and HK expression; (d) Iterations required for result converge as a function of MVD and matrix size. Some curves in the figures may overlap.

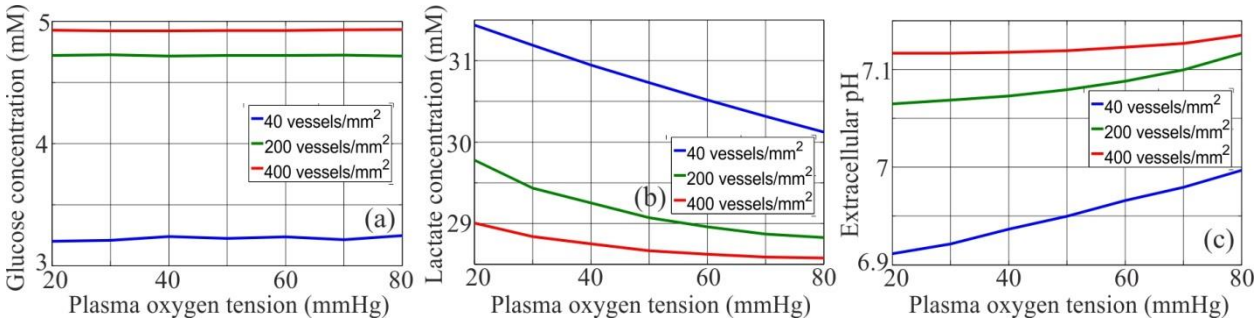

Figure 5.11. (a) glucose concentration as a function of plasma oxygen tension; (b) lactate concentration as a function of plasma oxygen tension; (c) extracellular pH as the function of plasma oxygen tension. The function curves under different MVDs (40, 200, 400 vessels/mm^2) of the tissue phantom are displayed here.

Table 5.3. The sensitivities of glucose and lactate concentration and extracellular pH in response to the plasma pO2 under different MVDs

	MVD=40 vessels/mm^2	MVD=200 vessels/mm^2	MVD=400 vessels/mm^2
Glucose	≈0 mM/mmHg	≈0 mM/mmHg	≈0 mM/mmHg
Lactate	-0.022 mM/mmHg *	-0.015 mM/mmHg	-0.007 mM/mmHg
Extracellular pH	0.0014 /mmHg*	0.0008 /mmHg	0.0003 /mmHg

* Sensitivity unit: [ΔConcentration]/[ΔTension]=mM/mmHg for glucose and lactate; [ΔpH]/[ΔTension]=1/mmHg for pH.

The sensitivity study investigating pixel size of the tessellated phantom has been conducted. It is found that the simulation results are influenced by phantom pixel size. Figure 5.12 shows the examples of the influences of pixel size (5 μm, 10 μm, 12.5 μm, 20 μm and 25 μm) on the 1D substrate (oxygen, extracellular glucose and lactate) distributions. Figure 5.13 presents the glucose and lactate concentrations and extracellular pH as the functions of the MVD (80, 120, 200 vessels/mm^2) and the pixel size (3.5-30 μm). The sensitivities of glucose and lactate concentrations and extracelluar pH to pixel size under different MVDs are listed in Table 5.4. Theoretically, the discrete results generated by more delicate grid partition are more approaching the desired simulation results, however brings more computation efforts. The selection of 10 μm pixel size results from the compromise between the simualtion accuracy and the computational time.

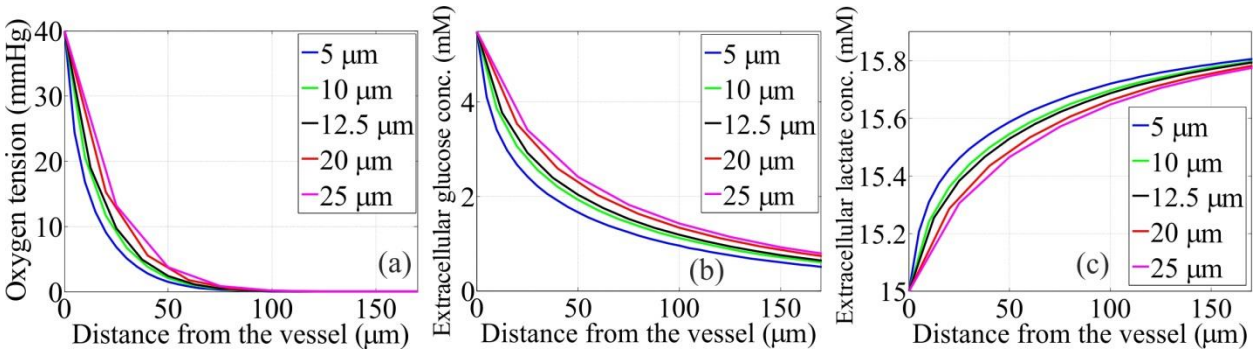

Figure 5.12. Examples of the influences of pixel size on the 1D substrate distributions. Figures (a)-(c) display oxygen, extracellular glucose and lactate as the functions of the distance from the vessel and the phantom pixel size (5 μm, 10 μm, 12.5 μm, 20 μm and 25 μm), respectively.

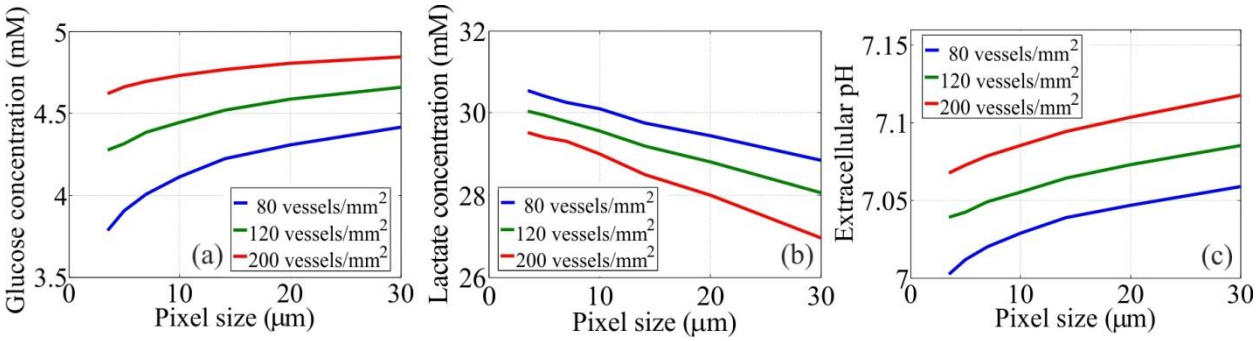

Figure 5.13. The average (over the phantom and different heterogeneities) glucose (figure (a)) and lactate (figure (b)) concentrations and extracellular pH (figure (c)) as the functions of the MVD (80, 120, 200 vessel/mm^2) and the pixel size (3.5-30 μm).

Table 5.4. The sensitivities of glucose and lactate concentration and extracellular pH to phantom pixel size under different MVDs

	MVD=80 vessels/mm^2	MVD=120 vessels/mm^2	MVD=200 vessels/mm^2
Glucose	0.022 mM/μm*	0.014 mM/μm	0.008 mM/μm
Lactate	-0.064 mM/μm	-0.077 mM/μm	-0.099 mM/μm
Extracellular pH	0.002 /μm*	0.0019 /μm	0.0017 /μm

* Sensitivity unit: [ΔConcentration]/[ΔPixelSize]=mM/μm for glucose and lactate; [ΔpH]/[ΔPixelSize]=1/μm for pH.

5.5. Results of the HIF-1 driven model

The overexpression factors proposed indicate the maximum folds of the investigated enzyme and transporter expressions that can be upregulated by HIF-1 particularly in hypoxic region. Their influence on the substrate distributions and concentrations are investigated by adapting them from 1 to 10 as to each enzyme or transporter. In the conditions of different mean intervascular distances and overexpression factors, enzyme and transporters get overexpressed to different extents. From the evaluation of their average levels over the tumor tissue phantom in relative to the levels in normal tissue, they are largely overlapped with the ranges reported by the literature as shown in Table 3.2.

The glucose and lactate concentration and extracellular pH as the functions of overexpression factors of GLUT and HK, and mean intervascular distance are displayed in Figure 5.14. The Figures (a), (c) and (e) present the concentrations of glucose and lactate and extracellular pH change with the GLUT overexpression factor and mean intervascular distance, respectively;

figure (b), (d) and (f) exhibit the variation of glucose and lactate concentrations and extracellular pH as the HK overexpression factor and mean intervascular distance.

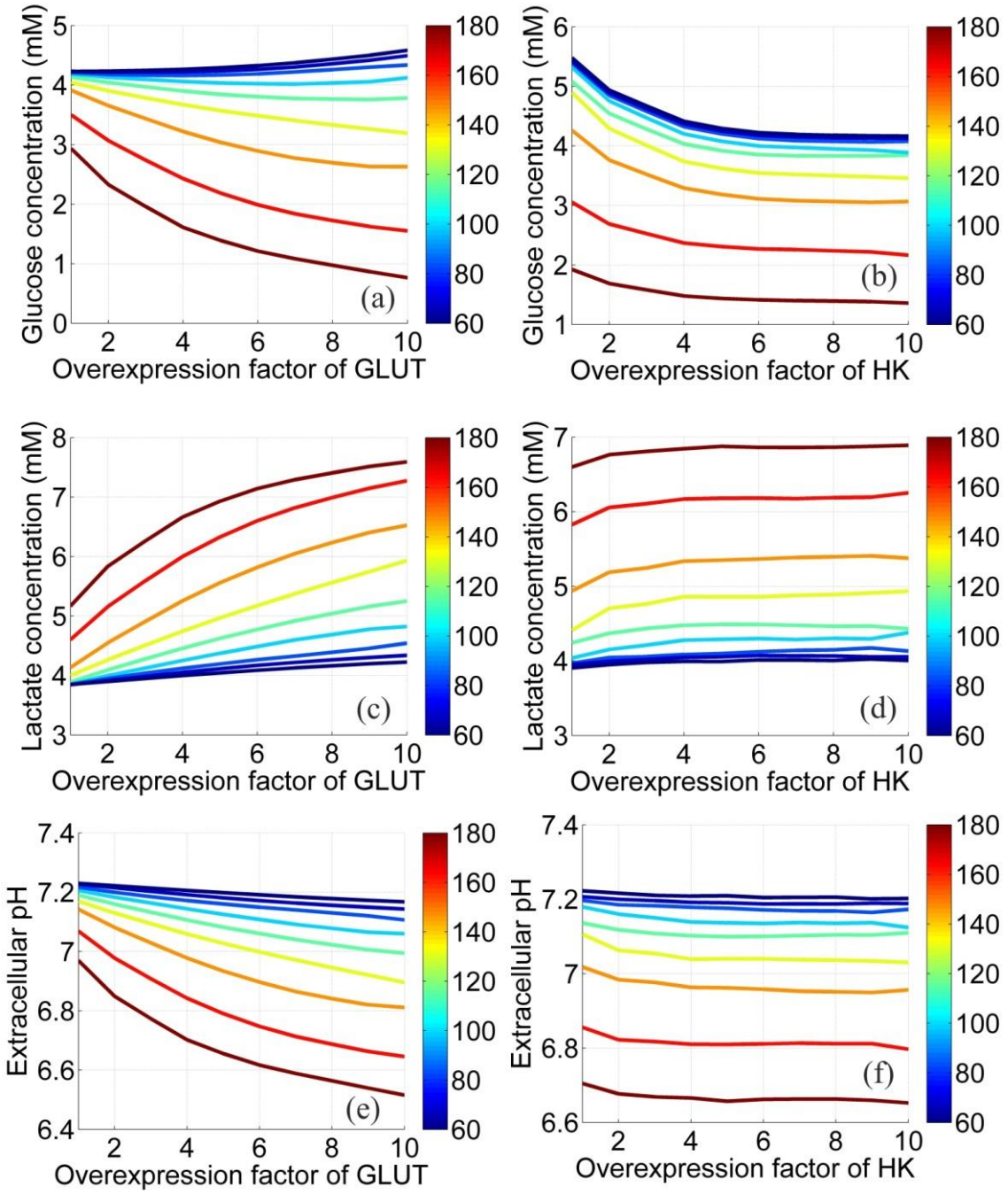

Figure 5.14. The substrate concentration as the functions overexpression factors of GLUT and HK and mean intervascular distance in the HIF-driven model. Figures (a), (c) and (e) present the concentrations of glucose and lactate and extracellular pH change with the GLUT upregulation and increased mean intervascular distance, respectively; figure (b), (d) and (f) exhibit the

influences of HK overexpression and mean intervascular distance on the glucose and lactate concentrations and extracellular pH, respectively.

Figure 5.15 exhibits the lactate concentration as the functions of overexpression factors of MCT1 and MCT4. The lactate concentration is raised by MCT1 expression for the phantom with higher microvessel density, while for the phantom with sparse microvessels, the lactate concentration is not affected significantly as the MCT1 expression level is low and less sensitive to the MCT1 overexpression factor (Figure 5.15(a)). As shown in Figure 5.15(b), the lactate concentration decreases with MCT4 expression at higher mean intervascular distance, while less sensitive to MCT4 expression at lower mean intervascular distance.

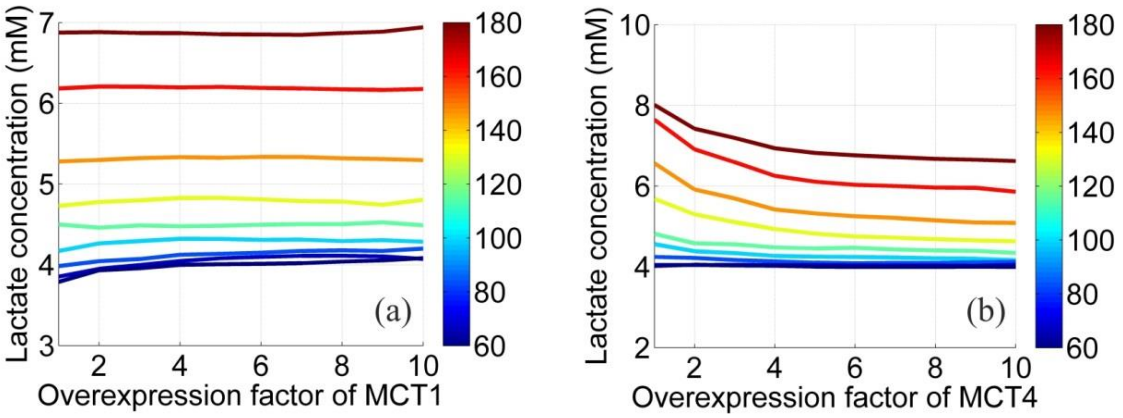

Figure 5.15. The lactate concentration as the function of MCT1 (a) and MCT4 (b) overexpression factor and mean intervascular distance

The substrate (glucose, lactate and extracellular pH) sensitivities in response to the unit alterations V_{max} of transporters and enzymes are evaluated (Table 5.5). Glucose concentration was found with similar sensitivity to the expression levels of GLUT and HK, while lactate and extracellular pH are more ($\approx$8 folds) sensitive to GLUT than HK in the HIF-1 driven model. Compared with the results concluded from the HIF-1 independent model, the introduction of HIF-1 increases the GLUT effect on the glycolytic flux with respect to HK.

The influences of GLUT and HK overexpressions in terms of overexpression factor adaptions on the glucose concentration and FDG activities are investigated using the tumor tissue phantoms containing different vascular densities, as shown in Figure 5.16. The FDG activity indicates the tissue activity that can be imaged by PET and contains the extra- and intra-cellular FDG activities and FDG activity that are accumulated in tumor cells over the time span of plasma

input function [3300 s; the plasma input function is displayed in Figure 5.6(b)]. Similar with FDG, the glucose concentration encompasses the extra- and intra-cellular glucose concentrations and the integral concentration of glucose that are metabolized during the past 3300 s. Each curve point takes the average of 20 repeated simulations to decrease the heterogeneity of microvasculature. The error-bars are added on each data point in the figures. The glucose concentrations and FDG activities as the functions of the overexpression factors are presented in the conditions of low, medium and high vascular densities: 20 (blue curve), 60 (green curve) and 100 (red curve) vessels/mm^2.

Table 5.5. The sensitivities of glucose and lactate concentration and extracellular pH to the alterations of V_{max} of GLUT, HK, MCT1 and MCT4 and the mean intervascular distance in the HIF-1 driven model

	S_G*	S_L*	S_{pH}*
GLUT	-13.4 s	31.5s	-4.9 s/mM
HK	-16.3 s	3.9s	-0.6 s/mM
MCT1	≈0**	0.07 s	-0.001 s/mM
MCT4	≈0**	-0.62 s	0.004 s/mM
Mean intervascular distance	-0.019 mM/μm	0.020 mM/μm	-0.004 /μm

* S_G, S_L and S_{pH} represent the average glucose, lactate and extracellular pH sensitivities in response to the unit changes of V_{max} of GLUT, HK, MCT1, MCT4 or mean intervascular distance, respectively.

** The glucose metabolism is not dependent on the expressions of MCT1 and MCT4 based on the proposed model, so the glucose sensitivity in response to changes of $V_{max, MCT1}$ and $V_{max, MCT4}$ equals to zero.

Both glucose concentration and FDG tissue activity are more activated by altered overexpression factors of GLUT than that of HK. HK upregulation exerts little influence on glucose and FDG uptake using the current pathophysiological parameters. The sensitivities of glucose concentration and FDG tissue activity in response to the unit adaption of GLUT and HK overexpression factors are presented in Table 5.6. The sensitivity values are also associated with vascular densities. In particular for GLUT, higher response rate is found for phantoms with higher vascular densities.

As the transport and metabolic kinetics of glucose and FDG are very similar in tumors, we evaluate the correlations between glucose metabolism and FDG uptake to validate the efficacy of FDG PET images in reflecting the glucose metabolism. The Pearson correlation coefficient between FDG tissue activity and glucose concentration that are accumulated over a same period

is 0.97 (P<<0.05) with consideration of various pathophysiological conditions (such as different GLUT and HK upregulating levels, and vascular distributions).

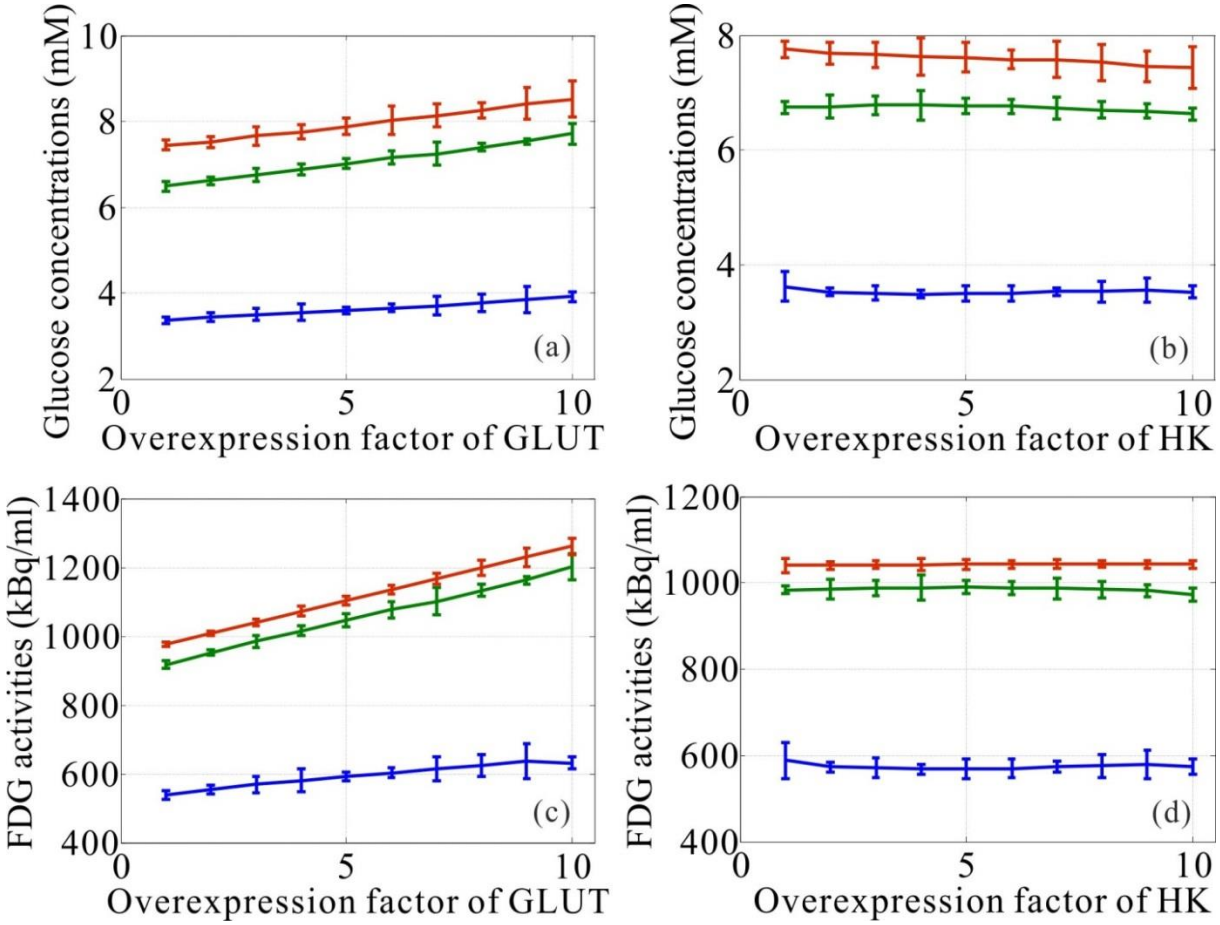

Figure 5.16. Glucose concentrations as the functions of GLUT (figure (a)) and HK (figure (b)) overexpression factors, and FDG activities as the functions of GLUT (figure (c)) and HK (figure (d)) overexpression factors. The curves are plotted in different vascular densities (blue curves: 20 vessels/mm^2; green curves: 60 vessels/mm^2; red curves: 100 vessels/mm^2). The error bars for each data point are added on each curve.

Table 5.6. The sensitivities of glucose and FDG with respect to the GLUT and HK upregulations in terms of overexpression factors (OF) under different vascular densities

Metabolite	Glucose			FDG		
Vascular density (vessels/mm^2)	20	60	100	20	60	100
Sensitivity to GLUT OF (mM)	0.06	0.12	0.13	11.2	30.0	31.6
Sensitivity to HK OF (kBq/ml)	0.003	-0.01	-0.03	0.48	-0.71	-0.51

5.6. Discussions

Alterations in metabolism and modified expressions of several enzymes and transporters are two hallmarks of malignant tumors [21]. They can be detected using molecular imaging (*e.g.*, PET, hyperpolarized MRI) and analyses of molecular biology (*e.g.*, staining of CD 31, GLUT, MCT1), respectively. Within the reaction-diffusion scheme, we established a mathematical model to link the substrate metabolism to the regulating enzymes, transporters involved and microvascular densities. The simulated substrate concentrations in the tumor tissue phantoms can fall into the ranges of experimental data reported in the literature. Using this model, we analyzed the influence of GLUT, MCT1, MCT4, HK and mean intervascular distance on the metabolism of glucose and lactate, and extracellular pH. The main findings from the relationship analysis are supported by *in vivo* and *in vitro* experiments. This quantitative investigation may add to our knowledge for the interpretation of the discrepancy between the tumor metabolism (reflected by substrate images) and the underlying tumor pathophysiological conditions (*e.g.* transporter and enzyme expressions).

5.6.1. Lactate-fueled respiration

The accumulation of lactate in tumors has been reported to correlate with tumor malignancy and can have an influence on therapy outcome [46, 167]. Recent studies revealed that lactate in tumors can also be utilized for energy supply [43]. This mechanism is possible due to the shuttling of lactate via MCT transporters [43]. In turn, shuttling and metabolism of lactate can impact tumor acidity. This study constructed a reaction-diffusion model to describe this complex procedure involving several interactions. From the simulated results (Figure 5.2c), the lactate shows higher intracellular than extracellular concentration in hypoxic regions due to high-rate glycolysis ($P([L_{in}])=2P([G_{in}])-P([O_2])/3>0$). The lactate gradient between the two sides of the cell membrane promotes excessive lactate to be exported via MCT4. As a consequence, lactate primarily accumulates in hypoxic regions and is then shuttled towards oxygenated (normoxic) areas. In oxygenated regions, shuttled extracellular lactate (as a result of diffusion from hypoxic to normoxic subvolumes) can be imported via MCT1 for oxidation ($P([L_{in}])<0$). These findings are consistent with previous experimental results [43, 114].

5.6.2. Regulation of enzymes and transporters

The expressions and activities of enzymes and transporters (*e.g.* GLUT, HK) are controlled by a series of molecular pathways (*e.g.*, HIF-1α, PI3K/mTOR) and can be upregulated during

carcinogenesis and tumor progression [29, 38, 110, 168-170]. For example, the activation of hypoxia-inducible factor 1α (HIF-1α) under hypoxic conditions (and a series of other factors) has been reported to correlate with the overexpression of GLUT1, HKII and MCT4 [171, 172]. In the current model, the influence of upstream processes on the upregulation of the investigated enzymes and transporters was not considered.

The current study focused on the influences of enzymes or transporters by adapting V_{max}. The function of enzymes or transporters is influenced by both their expressions and activities. In the Michaelis-Menten formulation, K_m reflects more of the enzyme/transporter activity. The concentration of the enzyme/transporter explicitly relates to V_{max} rather than K_m [47, 89]. Furthermore, the covariation of K_m and V_{max} depends on many unknown factors and its quantification remains elusive. Thus, V_{max} was only adapted for the investigation of the influence of enzymes/transporters on the substrate metabolism. Nevertheless, the analysis can be extended to investigate the influences of adapting K_m on metabolism with the proposed simulation model.

It has been found that the intra- and extra-cellular glucose concentrations positively and negatively correlate with GLUT expression (V_{max} of GLUT), respectively. And because of rapid glucose turnover, glucose has quite lower concentration in cells than in interstitium as shown in Figure 5.1(c) and Figure 5.2(b). Thus, glucose concentration (composed of intra- and extra-cellular parts) presents a negative correlation with GLUT expression as displayed in Figure 5.7a. The expression of HK (V_{max} of HK) has negative impact on intra- and extra-cellular glucose concentrations simultaneously, so that the decrease of glucose concentration as HK expression was observed in Figure 5.7b. The high expressions of GLUT and HK both promote the glucose supply for glycolysis, which is the reason for lactic acid production. Therefore the lactate concentration is positively correlated with GLUT and HK expressions, while the extracellular pH performs an opposite relation with GLUT and HK expressions as exhibited in Figure 5.7c-f.

In the current simulation model, the actions of GLUT and HK on glucose metabolism, and MCTs on lactate shuttling and metabolism were considered. Although GLUT and HK have several subtypes, which are expressed in different tumor types and have distinctive kinetics, they were configured generally without specifying the subtypes, tumor types and experimental conditions. The adaptive range in the current simulation may not mirror exactly the *in vivo* situation in all instances, although the results should be able to represent the *in vivo* situation in general. In addition, the model presented here can be extended to specified types of enzymes or transporters within the proposed framework.

5.6.3. Regulation of microvessel distribution

In the artificial 2D simulation, the distribution of microvessels may not represent the 3D microvasculature *in vivo*. In particular, it is difficult to directly translate the 2D microvascular density (number/mm^2) to 3D conditions (number/mm^3). In the present study, the mean intervascular distance (µm) was used as a surrogate parameter of the microvascular density.

Tumor metabolism is strongly influenced by the poor supply conditions which occur due to premature, chaotic microvessels [21]. From the pathophysiological point of view, tumor microvasculature may also have indirect impacts on metabolism by creating subvolumes exhibiting hypoxia which - through changes of the genome and proteome - can influence the expression of related enzymes and transporters [28, 109, 173, 174]. In this study, the microvessel distribution correlated strongly with substrate concentrations. The influences of enzymes and transporters on the substrate distribution are also dependent on the microvascular density. The absolute sensitivities of glucose and lactate, and extracellular pH to HK and GLUT decrease as the microvascular density increases. The transport and metabolism of a substrate were co-influenced by two factors: (i) the supply via the microvasculature and (ii) the activities of the enzymes and transporters. For a phantom with a higher microvascular density, an optimal microvascular supply may suppress the action of enzymes and transporters on regulating substrate concentration. Thus, the substrate concentrations are less dependent on the enzyme and transporters at high microvascular densities.

Our results show that the lactate concentration correlates positively with the MCT1 expression, but negatively with MCT4. This phenomenon can be explained by lactate shuttle and uptake. Tumors with a poor vascular supply contain more hypoxic regions and express more MCT4. This promotes the cellular lactate export, and meanwhile, the extracellular lactate concentrations maintain relatively constant. Therefore, higher MCT4 expression leads to more lactate reduction in more hypoxic regions. In well-vascularized tumor tissues areas, most of the cells are oxygenated (normoxic). In this case, higher expressions of MCT1 facilitate lactate (shuttled from normoxic regions) uptake by oxygenated cells, so that the lactate concentration correlated positively with MCT1 expression especially for more oxygenated regions.

5.6.4. Molecular imaging versus underlying pathophysiological features

In this study using computational simulation, we were able to map metabolic situations described earlier on the basis of experimental in vivo data. The tumor microvasculature was found to play a crucial role for the microregional distribution of glucose, lactate and extracellular pH. Lactate

levels are influenced to a greater extent by the microvascular density than by glucose concentration. The governing factors of the tumor microvasculature on the metabolism of glucose and lactate, and pH distribution have been reported in many studies [111, 163, 175-177]. The tumor microvasculature directly determines the substrate supplies to tumor tissue. Meanwhile, the imbalance between demand and supply due to malfunction of the premature tumor microvasculature indirectly influences the function of transporters and enzymes. In the TME the two effects may counter-act with each other, such that the tumor metabolism may pivot between balance and imbalance. For instance, the supply of glucose to tumor tissue with low microvasculature density is limited. On the other side, (even normoxic) tumor cells can switch to glycolysis coupled with enhanced expression/activities of related enzymes and transporters (the 'Warburg effect'). The counteraction of two aspects may reduce the effect of the microvascular distribution on glucose metabolism. Lactate is not supplied by the microvasculature. Its metabolism is strongly influenced by the imbalanced tumor oxygenation due to the inhomogeneous supply through the chaotic microvasculature. In this situation, the lactate concentration is mainly influenced by one of the counteracted effects, thus it is more sensitive to the TME than glucose.

The results presented here show that GLUT expression correlated significantly with concentrations of glucose and lactate, and extracellular pH. GLUT has a greater influence on glucose metabolism than HK. GLUT function is a critical factor in cellular glucose supply, i.e., before the intracellular breakdown of glucose occurs. It can influence the further reactions during glucose metabolism and may form a bottleneck for the downstream metabolic steps. Studies on FDG (a glucose analogue) uptake have confirmed that glucose metabolism is more determined by GLUT than by HK [178, 179]. For lactate and pH, studies usually focus on the regulation of MCT1 and MCT4. Our results show that the lactate metabolism and the extracellular pH are also influenced by the "upstream regulators" GLUT and HK, in addition to MCT1 and MCT4.

Tumor metabolism is co-regulated by many factors. Our results indicate that the interpretation of molecular imaging results is not straightforward. For example, the interpretation of lactate imaging may also need a consideration of the microvascular density and the expression of GLUT and HK. In practice, multi-modal imaging may provide a full spectrum of underlying pathophysiological features.

This model is expected to provide a tool for the development of multimodal imaging strategies. This is a hypothesis at the current stage and certainly needs more efforts with the support of other experiments and tests to make this development promising. As an assumption, the regression is made to relate the pathophysiological factors (response observations) to substrate concentrations (predictor variables). Using the simulation data, the regression results indicate

that the expression of GLUT depends on glucose and lactate concentrations and pH. The HK expression is only a function of glucose concentrations. Both MCT1 and MCT4 expressions are strongly dependent on lactate concentrations. The MVD (or intervascular distance) can be reflected by the combination of glucose and lactate concentrations. In addition, in view of the results of sensitivity analysis, glucose is obviously sensitive to both GLUT and HK expressions; whereas lactate and pH are 4.5-fold more sensitive to GLUT than HK. GLUT expression may be assessed by the combination of glucose and lactate concentration and pH, which is consistent with the regression findings. Based on regression and sensitivity analysis, the phenotypes on a microscopic scale may be reflected by one or a combination of substrate distributions imaged on a macroscopic scale.

A basic assumption of molecular imaging is that the distributions of the applied detection substrates (tracer, probe or contrast agent) correlate with the investigated intrinsic property. In reality however, their relation is not straightforward. In these studies, we have not only considered the in-system distributions of metabolites, but extended to model the distributions of imaging probes, such as ([^{18}F]FDG) by introduction of the modulation of HIF-1 and competition with metabolites (*e.g.*, glucose) for enzymes (*e.g.*, HK) and transporters (*e.g.*, GLUT).

5.6.5. Regulation of HIF-1

HIF-1, as one of the critical mediators between tumor hypoxia and metabolism, is introduced in the model to investigate its influence on the tumor microenvironment. The spatial distribution of HIF-1α is partially regulated by the oxygen content (HIF-1β is a constitutively expressed subunit). It is accepted that HIF-1α is rapidly degraded under normoxia, whereas hypoxia leads to stabilization and accumulation of HIF-1α [180]. In the proposed HIF-1 driven model, the HIF-1 distribution is mapped from the oxygen distribution based on the experimental relationship between oxygen and HIF-1 exhibited in Figure 3.5 [127] or is obtained by solving the evolution equation of HIF-1. Although the relationship between HIF-1 level and oxygen content may not be unique due to diversified tumor types and experiment conditions, the simulated HIF-1 distribution derived from the measurements or model equation can reflect its tendency in tumors. In the simulation of enzyme/transporters response to HIF-1 level, the ideal approach is plotting the curve of measured enzyme/transporter expression as the function of measured HIF-1 level. However, there is limited quantitative information reported about the spatial relationship between the two aspects. In the simulation, the expressions of enzyme and transporters are assumed to correlate linearly with local HIF-1. Although the assumed relationship may not be ideal, it reflects the basic relationship tendency in tumors. More specific relationship between enzyme/transporter expression and HIF-1 level will be explored to approach the simulation to the

measurement.

5.6.6. Model complexity and limitations

In contrast with the ordinary differential equation (ODE) based imaging analysis models [25], the proposed model is relatively complex by modeling the three synergistically functioning pathways hypoxia, glycolysis, and lactate fueled respiration. These investigated pathways are strongly related to several emerging molecular imaging methods. For the interpretation of these molecular imaging to pathophysiological phenotype and the development of corresponding quantitative strategies, it is necessary to include the relevant substrates and the influencing pathophysiological factors for the understanding of their interactive relations. Nevertheless, only the major factors can be included in the current simulation model after compromising between the computational efficiency and fidelity. The current model only considers the intracellular concentrations of glucose and lactate and describes the intracellular and extracellular distributions of these substrates and the respective transporters (GLUT and MCT) involved. It does not include the intracellular concentrations of the relevant anions, cations and CO_2, which are also transported across the cell membranes (passively or actively) and which form concentration gradients across membranes. Some of the ions involved in the current model are symported (lactate$^-$/H^+, Na^+/HCO_3^-) and antiported (HCO_3^-/Cl^-). For example, lactate$^-$ and H^+ are co-transported via MCT across the membrane. The H^+ and lactate$^-$ are subsequently bound to MCT on both sides of the cell membrane and the substrate-bound MCTs on both sides exchange until equilibrium is reached. The kinetic parameters for H^+ and lactate$^-$ co-transport are determined by the concentrations of H^+ and lactate$^-$ simultaneously [47]. However, the quantitative knowledge of these co-transport procedures is limited and has not been considered for the co-transports in the model. Nevertheless, the distributions of extracellular substrates in the current simulation reflect the *in vivo* situation.

In the current simulation, oxygen is assumed to be only used for glucose and lactate oxidation. This may not represent the realistic *in vivo* condition and oxygen consumption may also be used in other metabolic pathways. Consequently, the metabolic rate of lactate determined by oxygen and glucose consumption rates may be under- or over-estimated. However, it is reported that 90% of the oxygen consumption is used for glucose breakdown [181] . As a result, we did not consider any other metabolic pathways in this study.

The tumor hypoxia includes the chronic and the acute hypoxia. In the proposed model, we only consider the chronic hypoxia as the objective of the model is to investigate the relationship between the imaging signals and the expressions of the relevant enzymes and transporters at the

imaging time. Although the transient hypoxia can happen even within the imaging period, the influence of the acute hypoxia can hardly be detected in hypoxia imaging [34]. Also several pathophysiological factors (e.g. the expressions of GLUT, HIF-1) have been reported to be stable under acute hypoxia [28, 33]. Due to the restriction of complexity, the acute hypoxia is not considered in the current model.

Continuing as the previous studies [83, 85], a square phantom is considered for the modeling, and the vessel and cell shapes are assumed to be square. Nevertheless, our aim is to assist the development the strategies of imaging analysis strategies, which is expected to not to be influenced from the phantom geometry. The simplified geometries make the exploration and analysis of the underlying relations more straightforward.

To verify a simulation model, it would be ideal to simulate from realistic tumor geometry with onsite calibrated physiological and biochemical parameters and compare the simulation results with real measurements. However, it is difficult to achieve this with the restriction of current measurement technologies. It is very challenging to get all the required data from the same intact *in vivo* tissue. Also a direct comparison between macroscopic molecular imaging and microscopic tumor imaging such as immunohistochemical (IHC) is limited by the bottleneck of co-registration. Although several co-registration methods have been developed, there still exists a large deformation during the tumor resection and cutting and a large resolution gap between microscopic feature and macroscopic feature. In addition, the interpretation of *ex vivo* staining data (*e.g.* IHC) to quantitative values of kinetics of the proteins is still difficult. Therefore, the direct comparison of the modeling data with clinical or preclinical imaging data is not achieved in this study. At the moment, the modelled data is validated by indirect comparisons with the empirical data in the literature. Although not all the investigated properties has quantitative values in the limited availability of literature data, we try our best to verify that most simulated substrate concentrations fall in the range of experimental data reported in the literature, and the main simulation findings (*e.g.* GLUT controls the glycolytic flux in tumors, and extracellular pH has little correlation with MCT levels) are consistent with the experimental results in the literature.

5.7. Conclusions

In this study, computational simulation models are proposed to investigate the quantitative relationship between glucose and lactate metabolism and pathophysiological features in the microenvironment of solid tumors. The main simulation results are in agreement with the *in-vivo* and *in-vitro* literature data. The influences of several physiological factors (*e.g.*, expression

levels of HIF-1, GLUT, HK, MCT1 and MCT4, plasma oxygen tension, vascular distribution) and simulation factors (*e.g.*, pixel size of tumor tissue phantom, iterations) on the simulation results are evaluated. The FDG uptake is also integrated in the proposed model. The FDG model is validated by comparing simulated TACs with the measured one. And the influences of pathophysiological factors (*e.g.*, vascular density and perfusion, GLUT and HK expressions) on the FDG uptake are assessed. The quantitative relationship established by the proposed models may allow the theoretical interpretation of the co-influence of multiple factors and the systematic understanding of principles behind molecular imaging. The computational simulation may assist the hypothesis generation to bridge the discrepancy between the substance imaging on the macroscopic scale and the tumor pathophysiological factors on the cellular scale. It has the potential to accelerate the development of multi-modal image analysis strategies for tumor phenotype estimation.

6. Validation and applications of positron imaging: imaging characterization and spatial resolution improvement by classification algorithm

To improve the spatial resolution of positron imaging, a classification model is proposed in chapter 4 by learning the advanced features of simulated positron trajectories in a silicon detector. This chapter validates the method on the [^{18}F]FDG imaging using an absorbing edge protocol and a leaf sample. The positron imaging characteristics are evaluated by both measurements and Monte-Carlo simulations in advance of model validation to have a comprehensive understanding of the imaging system, which can assist the classification method implementation and imaging setup optimization.

6.1. Positron camera characterization: a comparison between measurements and Monte-Carlo simulation

The Timepix chip is operated with a global discrimination threshold (THL) corresponding to digital-to-analog converter (DAC), which is obtained by threshold equalization over pixels. The THL is individual for each Timepix chip. The DAC number in TOT model is calibrated to real energy [158]. In both modes, the bias voltage and clock are chosen to be 100 V and 9.6 MHz, respectively.

The key characteristics of the positron camera are evaluated in this section. The simulated and measured characteristics are compared. Figure 6.1(a) displays simulated trajectories (yellow dots) in the Timepix detector of 100 positrons emitted from an ideal point source (orange dot on top of passivation layer). Figure 6.1(b) compares the simulated energy spectrum of energy deposition in the Timepix detector after incidence of a positron compared with measurement.

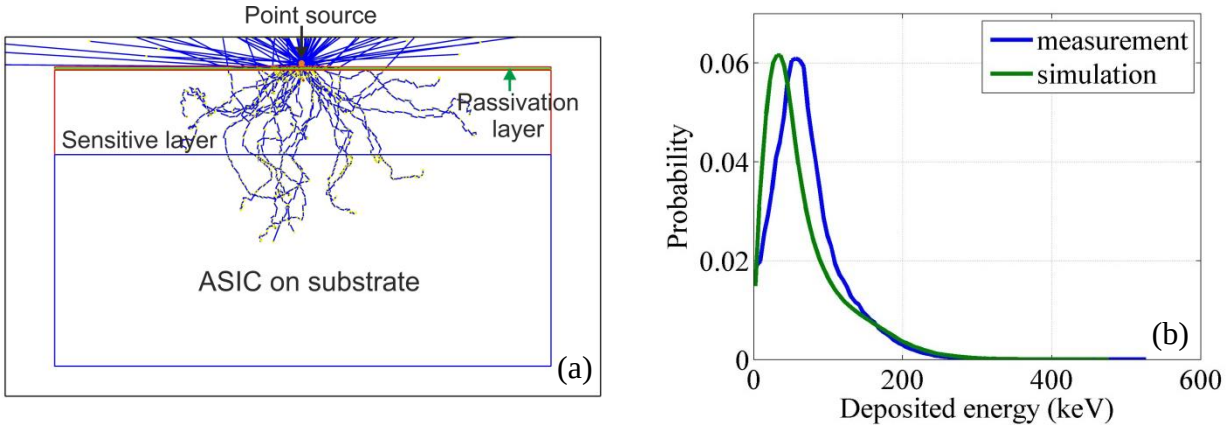

Figure 6.1. (a) The trajectories of 100 positrons passing through Timepix simulated by Geant4; (b) The measured and simulated deposited energy spectrum of ^{18}F positrons.

In most cases, adjacent pixels excited by one incident particle in a single short frame compose a cluster. Figure 6.2 displays the histogram of cluster sizes. The average experimental cluster size is 5.2 pixels. The average simulated cluster size is 5.1 pixels (without energy threshold, without charge diffusion) and 4.7 pixels (with energy threshold, without charge diffusion), 4.8 pixels (with energy threshold, with charge diffusion). The experimental settings and simulation parameters for energy spectrum and cluster size distribution are consistent with those for spatial resolution.

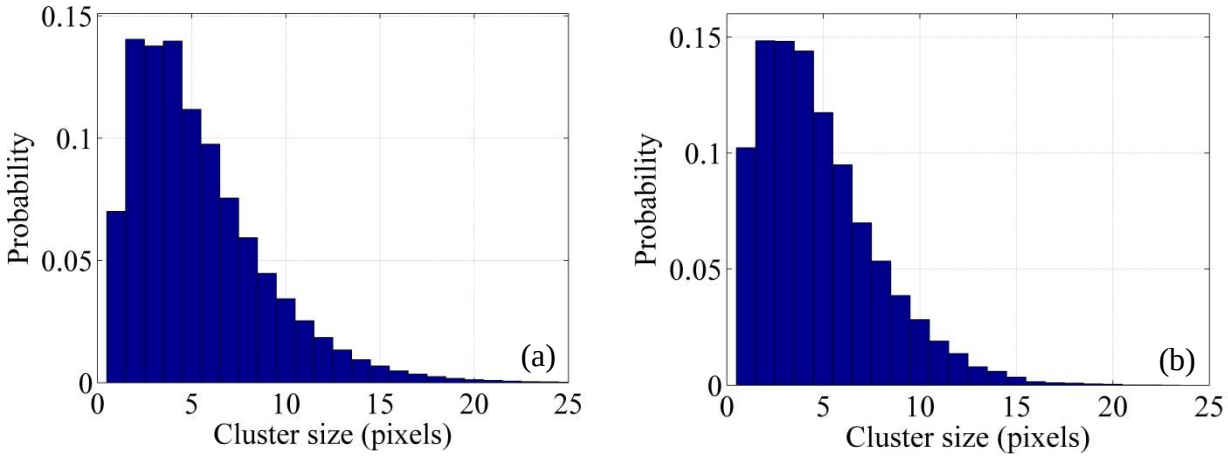

Figure 6.2. The experimental (a) and simulated (b) cluster size distribution

6.1.1. Sensitivity and linearity

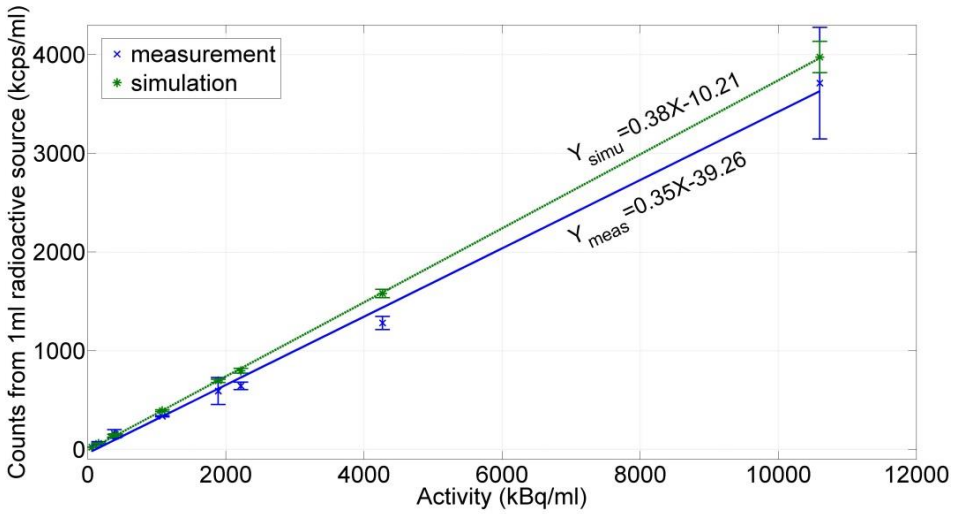

Figure 6.3. The linearity of the ^{18}F positron detecting system. Counts detected (blue '×') and simulated (green '*') with respect to 9 different activities of a 1 ml radioactive source are fitted linearly (blue solid and green dashes line).

In order to test sensitivity and linearity, nine FDG samples with different radioactivities: 0.1, 0.3, 0.6, 1, 3, 6, 10, 30, and 60 MBq/ml were prepared and measured. The exact radioactivities at the moment of measurement were calibrated by reference to a measurement in a gamma counter (WALLAC 1480 Wizard). A 10 µl droplet taken from the FDG samples by pipette was dropped on the detector surface. The detector surface is protected by a 6 µm thick Mylar foil (Pütz GmbH

+ Co. Folien KG). Positron interactions with the detector were recorded for each sample by the positron camera operated in TOT mode. All the pixels excited by one incident particle compose a cluster, which we regard as one count received by detector. The detecting frame width was chosen short and adapted to the source activities to avoid cluster overlap. The frame widths of 10 ms, 5 ms, 1 ms, 0.5 ms, and 0.1 ms were tested before the experiment with the source of highest activity and a frame width of 1 ms was selected for the acquisition of the data. Figure 6.3 shows the measured counts (blue) of 9 ^{18}F samples of different activities as well as the theoretical prediction from simulation (green). The sensitivity for measurement and simulation is 0.35 cps/Bq and 0.38 cps/Bq from linear fitting, respectively. The linearity and sensitivity of the measurement is close to the simulation.

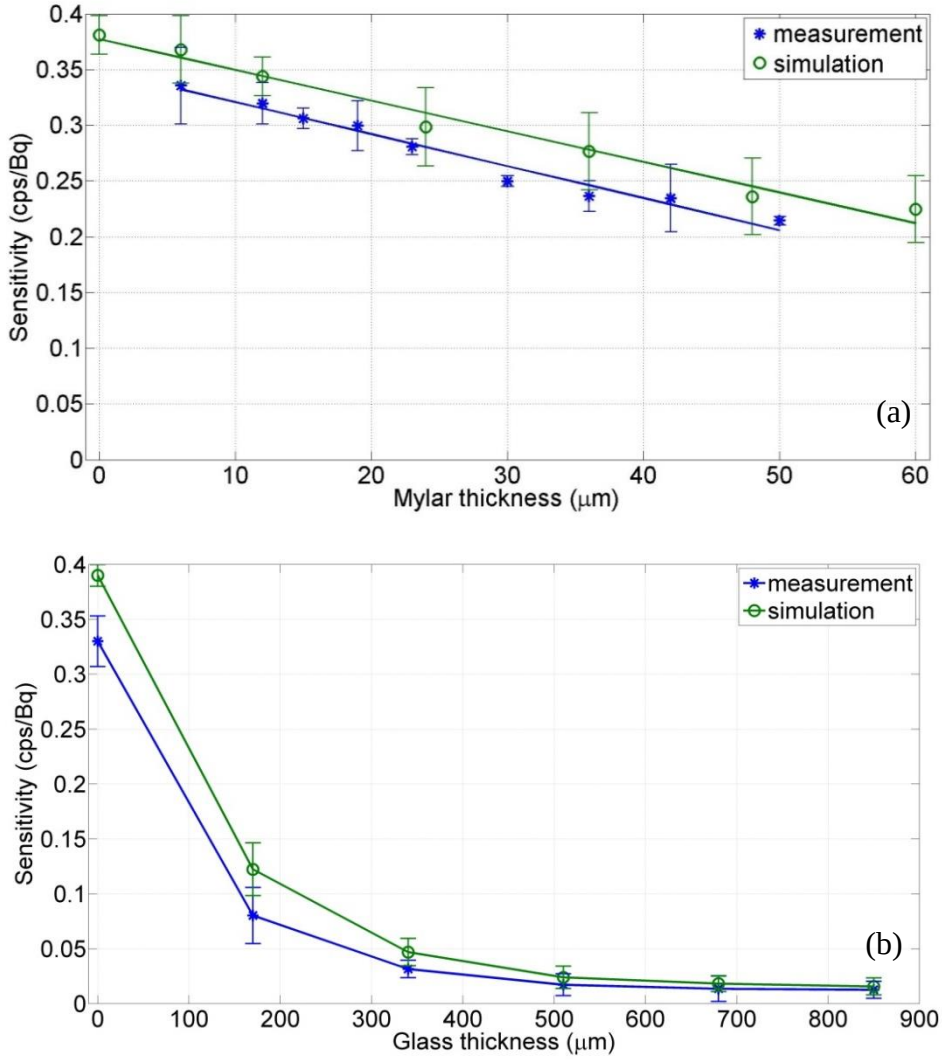

Figure 6.4. The sensitivity affected by the Mylar (a) and glass slide (b) between sensor and sample. The measured sensitivity curves (blue) are compared with simulated ones (green).

The detector is sealed with a thin layer of aluminum (thickness 1μm) and a layer of Mylar (thickness 6 μm) for detective surface protection and the sensitivity of the detector was defined with all the covers. However, the imaging of positron is strongly influenced by the medium between the imaging object and the detector The influence of medium between detector and sample on sensitivity is evaluated. Various layers of glass slides (thickness 170 μm, 0~5 layers) and Mylar with different thicknesses (6, 12, 15, 19, 23, 30, 36, 42, 50 μm) as the medium are inserted between the detector and the source to assess the influence of additional medium on sensitivity. The sensitivity curves in relation to medium thickness are plotted in Figure 6.4, where measured and simulated sensitivity curves are compared. Every 10 μm increase of Mylar or glass will lead to 0.025 and 0.015 cps/Bq sensitivity loss, respectively (the range out of the quasi-linear region is not considered for sensitivity loss evaluation).

6.1.2. Spatial resolution

The spatial resolution for positron measurements is affected by multiple scattering of positrons, charge diffusion effect of generated electrons in detector crystals, and system noise [68, 152]. The spatial resolution was obtained by absorber edge method (AEM) [20] and its measuring process is shown in Figure 6.5. Half of the detector surface was covered by a 300 μm thick aluminum whose edge is straight and sharp to reduce border scattering (Figure 6.5(b)). A 10 μl droplet of FDG (activity: 30 Mbq/ml) was dropped on the Mylar held 5cm above the detector (Figure 6.5(c)). 30000 frames with 0.1 s width were detected in TOT mode, which records the energies deposited in pixels. Before calculating spatial resolution, the edge alignment was controlled by estimating the edge on the acquired image. This was achieved by fitting a line on the gradient image obtained using a Sobel operator.

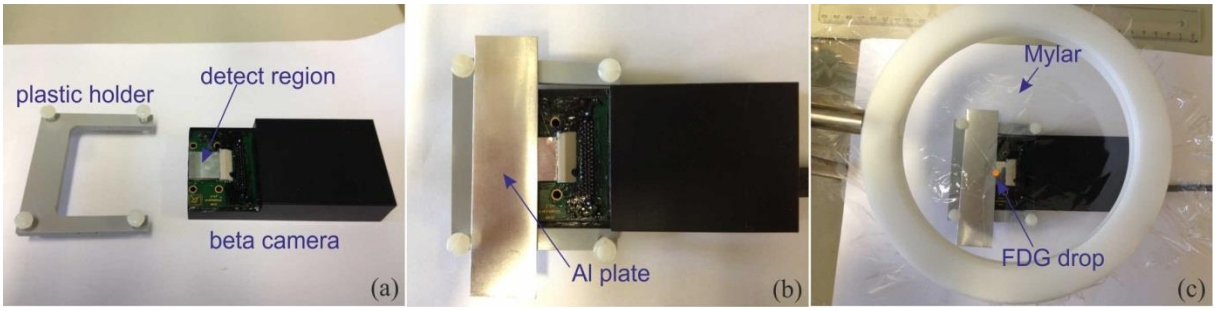

Figure 6.5. The process of measurement for spatial resolution.

The energy weighted centroid approximation has been demonstrated to improve the spatial resolution in the imaging of other radio-isotopes (such as $^{90}Sr/^{90}Y$ and ^{14}C electrons) [63, 77].

This method is tested here for its ability to enhance the spatial resolution of 18F positron imaging. The centroid of the cluster was calculated to assess the incident position of the positron. The recorded energy deposited in each fired pixel within a cluster was taken as weight for the estimation of the centroid of the cluster. The cluster energy is the summed energy of all pixels involved in the event. It is not equivalent to the energy of the incident positron, since the positron may not be completely absorbed in the detector's sensitive layer.

An image of an ^{18}F positron edge profile for the measurement for spatial resolution is shown in Figure 6.6(a). The edge response function (ERF) is determined by averaging 100 columns perpendicular to the edge and the corresponding line spread function (LSF) is derived by differentiation of ERF as shown in Figure 6.6(b) and (c). The system spatial resolution was estimated by the FWHM of the peak of the LSF at the edge region. The spatial resolution based on the measurement shown in Figure 6.6(a) is 155.5±3.1 μm (with energy centroid approximation) and 177.1±4.1 μm μm (without energy centroid approximation).

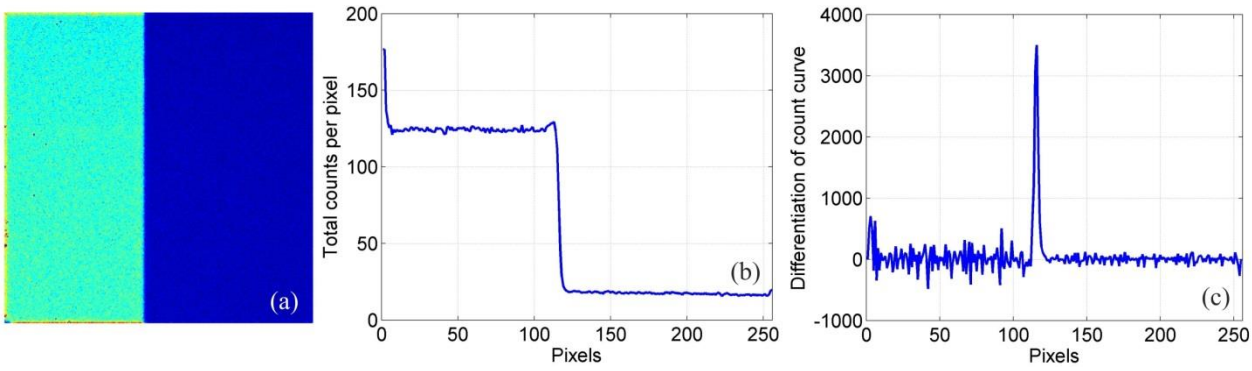

Figure 6.6. The process of obtaining the spatial resolution using AEM: (a) the image of FDG edge profile; (b) the ERF of positron image; (c) the LSF: the differentiation of ERF.

6.1.3. Influence of background

Although Timepix is sensitive to charged particles, it can still capture some gamma rays of positron annihilation. To evaluate the ratio between positrons and gamma rays, measurements with and without a covering Cu plate (500 μm thick) of detector surface are performed. A 10 μl FDG droplet source (activity: 10 MBq/ml) was dropped on the center of detector. The Cu plate is expected to block positrons without influencing gamma rays. In Medipix and TOT mode 100,000 frames (width 1 ms) are recorded. A 50 pixels × 50 pixels region in the center was chosen to count the clusters and calculate the ratio between the signals covered and not covered by the Cu plate.

To investigate the background from electronic noise and other possible surrounding radioactive sources, the background signals were recorded for 8 hours with 2880 frames (width 10 s) in Medipix and TOT mode, respectively. The background is supposed to be homogeneous over field of view of the detector. The signal-to-noise ratio (SNR) of detecting system is evaluated by selecting a region of interest (ROI) and an equivalent background area [156, 182]. The SNR=μ/σ_0, where μ is the mean value of counts in ROI and σ_0 is the standard deviation of counts in background region.

The ratio between detected gamma rays and positrons is ~1.9% for both Medipix and TOT mode, and it's consistent with simulated ratio. A negligible influence of background was observed during the whole measurement (Medipix mode: 3.1×10^{-6} cps/pixel, TOT mode: 1.3×10^{-4} keV/s/pixel).

6.1.4. Ex-vivo mouse tissue sample imaging

FDG uptake images of a heart tissue slice of a C57B1/6 mouse was measured by the positron camera. The mouse experiments described here have been approved according to German animal welfare regulations. The 17 weeks old mouse received T-NHL cells intravenously 18 days before imaging. It was fasted overnight before the injection of FDG (activity: ~4 MBq). After sacrifice, the heart was taken out, rinsed for three times, frozen and then cut into slice of 20 μm thickness (Leica CM1950 freezing microtome).

After the preparation of the heart tissue cyro-sliced sample, it was measured by the positron camera in TOT mode for 20 min by placing it 1mm above the camera surface. Afterward, to compare the difference between heart tissue slice images acquired in TOT mode and in Medipix mode, we detect a phosphor image as reference. The same sample was transferred to an autoradiography cassette for film (Kodak phosphor imaging plate) exposure of 16 hours. Then it was scanned by CR 35 Bio Image Plate Scanner (Duerr Medical GmbH) for 10 min with an intrinsic resolution of 25 μm spatial resolution.

Figure 6.7(a) and (c) are the results of positron imaging of a mouse heart tissue slice in Medipix mode: normalized hits and normalized counts (without energy weighted centroid approximation) respectively. Figure 6.7(b) and (d) show the same heart images obtained in TOT mode: normalized deposited energy and normalized counts (with energy weighted centroid approximation) respectively. An incident positron traverses the detector depositing energy in each inelastic collision, which is defined as a hit here, and all the pixels excited by deposited energies compose a count. For the comparison with the phosphor reference image, the absolute

pixel values of Figure 6.7(a)-(d) are normalized by the global mean (mean value over all image pixels). The RMSE of Figure 6.7(a)-(d) relative to reference image is evaluated. Before RMSE evaluation, phosphor image were firstly interpolated and sampled to the same pixel size (55 μm) as positron camera images and then co-registered using a mutual information algorithm (Fiji Image J).

To compare the positron images in Figure 6.7(a)-(d), the geometry of the heart is identified in the reference phosphor image and the outline is displayed in the figure. The mean normalized hits and normalized deposited energy over the outlined region are 7.6 (Figure 6.7(a)), 7.7 (Figure 6.7(b)), 6.7 (Figure 6.7(c)) and 6.8 (Figure 6.7(d)) in comparison with the mean of normalized particles 9.7 in reference image. The RMSE to the reference phosphor image of outlined heart region is 2.9, 2.8, 3.8 and 3.7 for images Figure 6.7(a)-(d).

For the purpose of evaluating the SNR of positron imaging, two regions of interest (ROIs) of the same size (45 × 30 pixels) were chosen in the heart region as well as in the background region distant from the heart. We obtained SNR (between ROI and background area): 103.6, 115.7, 39.0 and 39.7 for Figure 6.7(a), (b), (c) and (d) respectively.

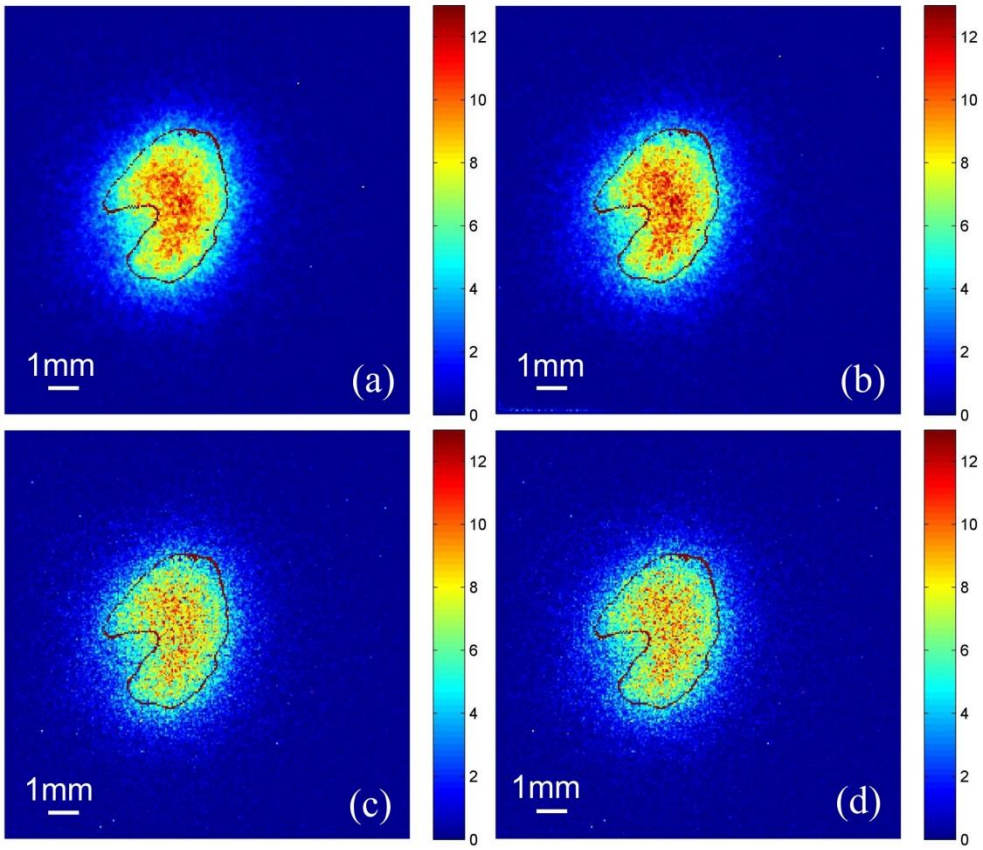

Figure 6.7. Positron camera images of a mouse heart tissue slice with [^{18}F]FDG uptake. The amplitude in image (a) and (c) is normalized hits and normalized counts (without energy weighted centroid approximation) obtained in Medipix mode, and the amplitude in image (b) and (d) is normalized deposited hit energies and normalized counts (with energy weighted centroid approximation) obtained in TOT mode. The heart region composed of pixels with normalized amplitudes above 5 in reference image is outlined in image (a), (b), (c) and (d) by red curves respectively.

6.2. Validation of classification algorithm on spatial resolution improvement for ^{18}F positron imaging

6.2.1. Verification of Monte-Carlo Simulation

The simulated pixel energy spectrum and cluster size distribution has presented similar tendencies with the measured ones as exhibited in Figure 6.1(b) and Figure 6.2 [157]. The average cluster size for measurement and simulation were 5.2 and 4.7 pixels, respectively, under the setting of absorption edge protocol.

Seventeen selected classification features were analyzed with PCA. Five independent features (the newly formed features after PCA) were found with highest contributions to the classifier. By testing, the classification results generated by them turned out to be consistent with the results obtained by only using the features of E_1, E_2, N_1, N_2 and the normalized pixel distance from the cluster energy-weighted centroid. These 5 features also bring the highest classification sensitivity. This phenomenon indicates that E_1, E_2, N_1, N_2 and the normalized pixel distance are the most functional features within the current feature selections. The simulated spectrum of features: E_1, E_2, N_1 and N_2 were compared with the measured ones as shown in Figure 6.8. The differences between simulated and measured features are not significant (H=0, P=1). The simulated features have similar behavior as the measured ones, thus we can transfer the simulation data to the learning procedure.

6.2.2. Verification of the classification using simulated data

10^5 positrons emitted from the ^{18}F general source were simulated to pass through the detector and generate the training data. This number of positrons was found to generate stable results within the tested range of 5×10^3 to 10^6 emitted positrons.

The classification accuracies were estimated and listed in Table 6.1. Three types of accuracies were assessed on each set of clusters (2-pixel cluster, 3-pixel cluster, 4-pixel cluster, 5-pixel cluster and more-pixel cluster): Accuracy 1 — correctly classified primary pixels / the classified primary pixels; Accuracy 2 — secondly fired pixels misclassified as primary pixels / the classified primary pixels; Accuracy 3: thirdly fired pixels misclassified as primary pixels / the classified primary pixels.

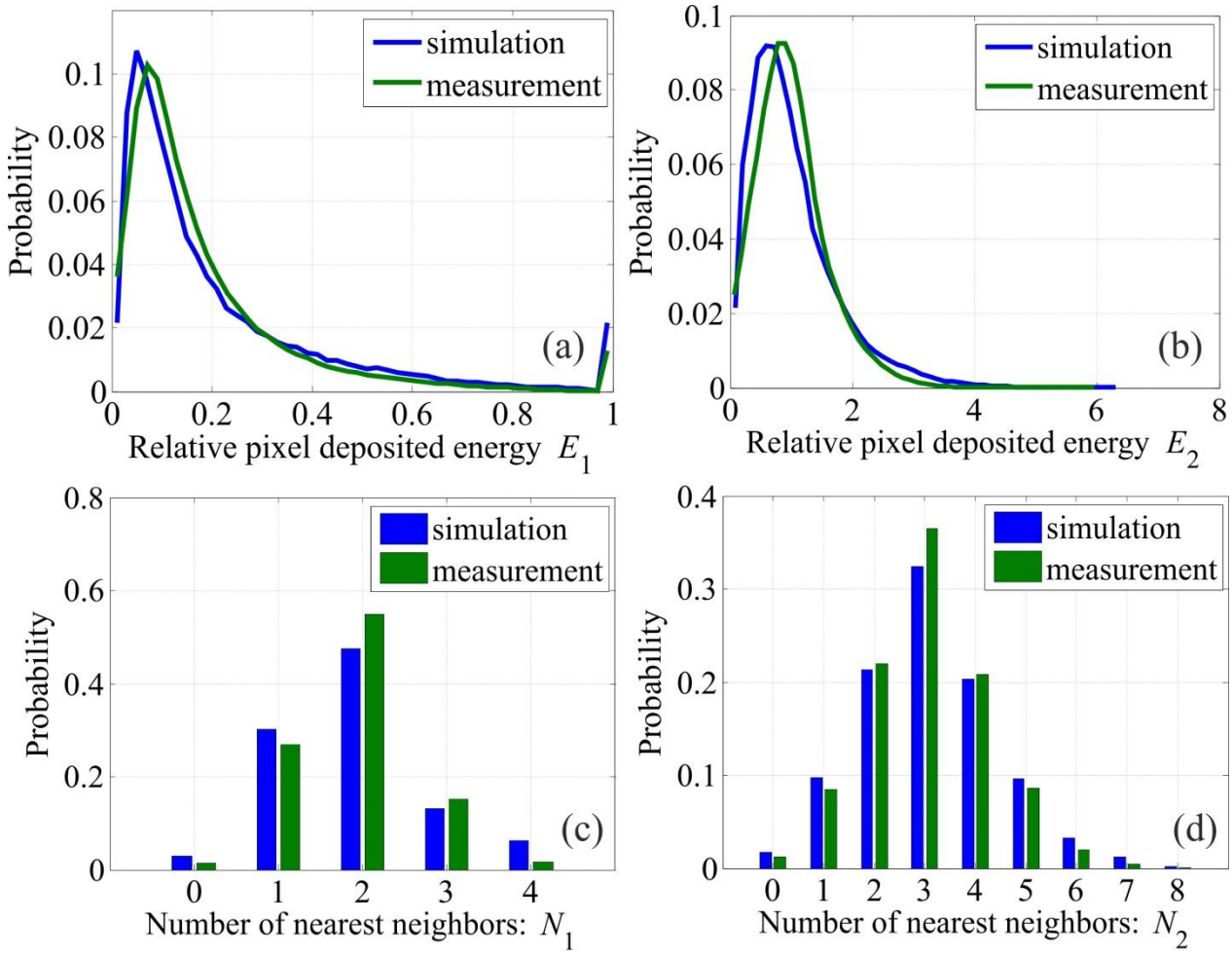

Figure 6.8. The comparison of feature spectrum between simulated and measured data.

Table 6.1. The classification accuracies using simulated testing data

	2-pixel cluster	3-pixel cluster	4-pixel cluster	5-pixel cluster	more-pixel cluster
Accuracy 1 (%)	64.5±1.7	74.2±2.3	80.8±1.9	75.9±2.4	76.2±2.2
Accuracy 2 (%)	35.5±1.7	17.4±1.3	8.1±1.0	9.7±1.1	1.7±0.2
Accuracy 3 (%)	0	8.4±0.9	6.5±1.0	4.3±0.3	0.7±0.1

Cluster percentage*	19.5 ±1.3	15.5 ±0.7	12.5 ±0.9	9.8 ±0.8	32.9 ±1.1

*cluster percentage: proportion of a certain type of clusters within the total clusters.

Figure 6.9 shows an example of a classification result using simulated data as testing set. The classified map of clusters is compared with the original map (ground truth) with pre-knowledge of the pixel sequences in clusters (field of view, FOV: 60×60 pixels). The classes 1 to 4 are marked by color red, orange, green and blue, respectively. In the FOV, 19 clusters are ready for classification, within which 4 clusters are misclassified with primary pixels (red circle) or suffer from classifier failure (green circle).

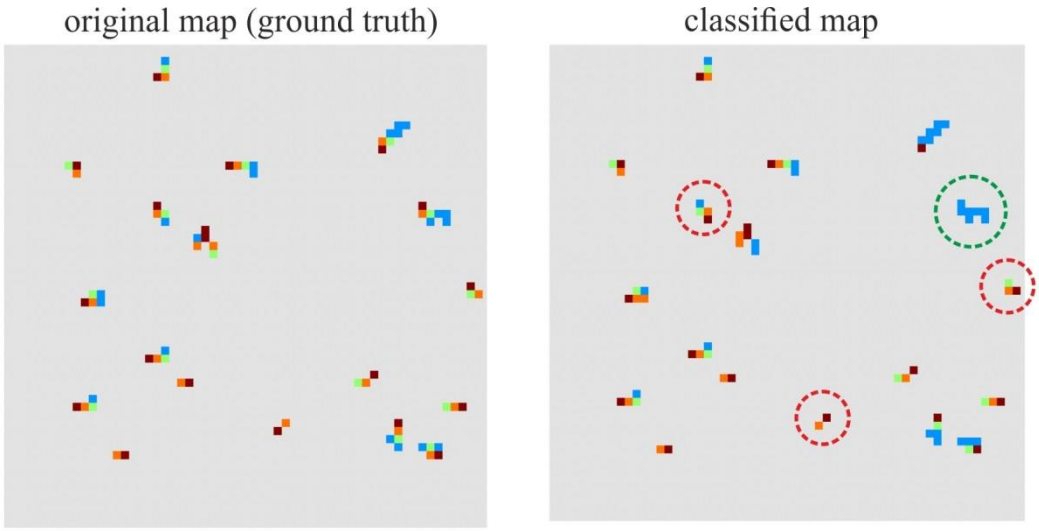

Figure 6.9. An example test on the simulation data: the left is the ground truth of the simulation and the right is the result of the classification. The classes 1 to 4 of both ground truth and classification results are labeled with colors red, orange, green and blue, respectively. The misclassification and classifier failure are marked with red circle and green circle, respectively.

6.2.3. Verification of the algorithm in measurements using absorbing edge method

The spatial resolution of ^{18}F positron imaging is evaluated by AEM. Uniform and energy weighted centroid approximations were applied to the positron edge image, respectively, as shown in Figure 6.10(a) and (b). Figure 6.10(c) is the classified image considering the sensitivity loss compensation. While the classified image without the sensitivity loss compensation is shown in Figure 6.10(d). For Figure 6.10(a) to (d), the amplitude of the images is the number of counts, which can be the clusters (Figure 6.10(a) and (b)) or primary pixels (Figure 6.10(c) and (d)). The red box in figure (d) outlines the columns (as to all images) on the edge which was used

for averaging the edge response function. Figure 6.10(e) shows the edge response function of the 4 images above. The spatial resolution is obtained by calculating the FWHM of the line spread function given in Figure 6.10(f). The spatial resolution for the edge image applying the classification algorithm is 136.3±1.6 μm with sensitivity compensation and 128.4±3.8 μm without sensitivity compensation, as compared with that of edge images processed with uniform and energy weighted centroid approximation: 160.0±3.1 μm and 156.6±4.0 μm, respectively. The current method enhances the spatial resolution by 24.2%. This spatial resolution improvement is accompanied by 23.8% sensitivity decrease. With sensitivity loss compensation, the spatial resolution improves by 17.6% compared with the energy weighted centroid method.

Using cluster energy or primary pixel energy as the image values instead of counts in Figure 6.10(a) to (d), the spatial resolutions of the corresponding images are 151.9±5 μm, 147.7±5 μm, 135.0±4 μm, and 126.9±4 μm, respectively, which are slightly higher compared to the cases in which the image amplitudes are the counts.

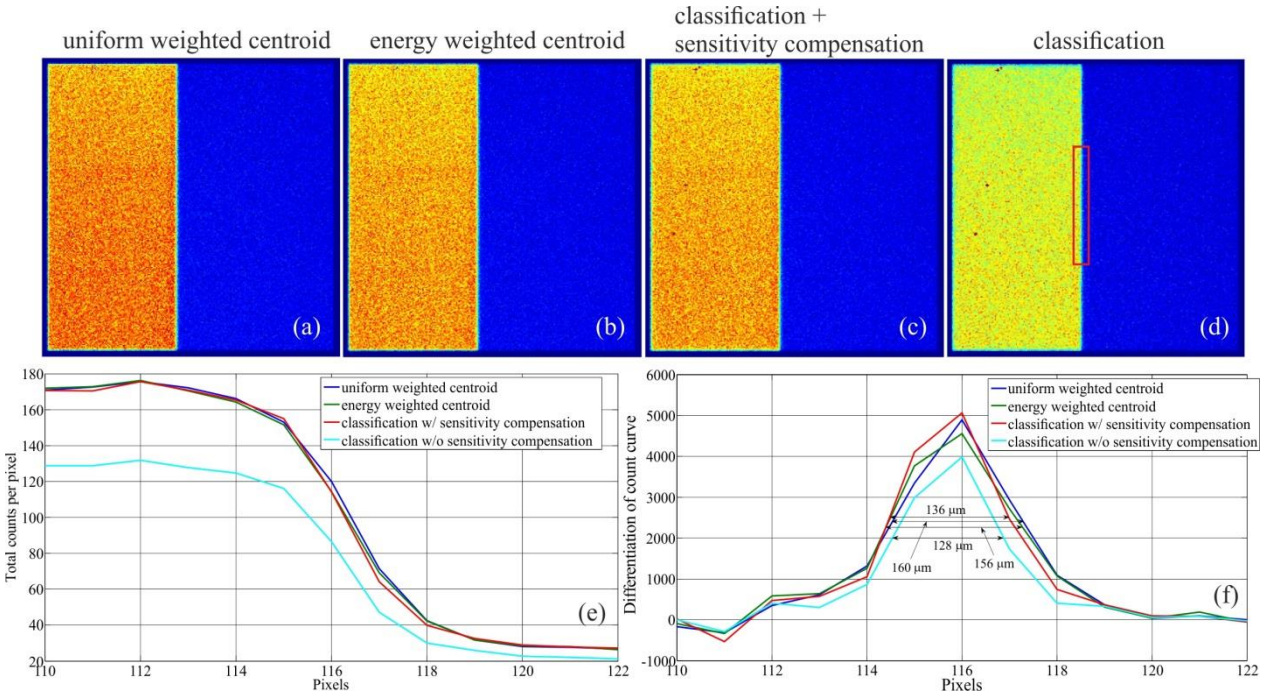

Figure 6.10. An example of obtaining spatial resolution by AEM. Figures (a) and (b) are the edge images with uniform and energy weighted centroid approximation respectively; figures (c) and (d) are the edge images obtained by classification method with and without consideration of the sensitivity compensation respectively; Figures (a) to (d) have same amplitude color scale. Figure (e) shows the edge response function curves of figures (a) to (d); figure (f) presents the corresponding curves of line spread function and the spatial resolution are marked on each curve.

The red box in figure (d) outlines the columns on the edge to be averaged for the edge response function.

6.2.4. Verification of the algorithm for positron imaging

The positron images of the leaf sample were assessed by calculating the root mean square error (RMSE) relative to the phosphor image and the Dice coefficient relative to the optical image. Since the pixel size of the positron image from the Timepix detector (55 μm) is not consistent with that of the phosphor image (25 μm) and the optical image (21.2 μm), the phosphor and the optical image were resampled to have the same pixel size as the positron image for quantitative assessment. Then the phosphor and the optical image were registered to the positron image by Fiji Image J.

The positron and the phosphor images were then normalized by their global means, respectively. For a positron image, RMSE in relation to the phosphor image is given by:

$$RMSE = \sqrt{\sum_{i\in\Omega}(A_i - P_i)^2 / n} \tag{6.1}$$

Where, A_i and P_i are amplitudes of pixel i, $i \in \Omega$ in the normalized positron image and normalized phosphor image. The Ω denotes the leaf vein region (*i.e.*, the region of interest), which is segmented by Otsu thresholding in the phosphor image.

The leaf vein structure was segmented by k-means clustering (5 clusters) in the optical and the positron images. The Dice coefficient, which characterizes the similarity of two images [183], was then calculated using the segmented images over the region with the major part of the leaf vein structure (150 × 150 pixels).

The positron image of a part of a leaf sample after applying the proposed method was compared with that based on energy weighted centroid method (Figure 6.11). Figure 6.11(a) is the positron image processed with energy weighted centroid method. Figure 6.11(b) is the image processed with the proposed method. Figure 6.11(c) shows the phosphor image as a reference. The amplitudes of all images are normalized by the global mean. The global mean for Figure 6.11(a) and (b) is 22.2 counts, compared with 178.4 counts in Figure 6.11(c). The region with highest amplitudes of Figure 6.11(c) presents the main vein containing the tracer. The RMSEs of Figure 6.11(a) and (b) are calculated relative to the phosphor image over the main vein region. The RMSE for Figure 6.11(b) is 1.59 compared with 1.83 for Figure 6.11(a). Figure 6.11(d) is the optical leaf image. The Dice coefficients of the segmented vein structure of Figure 6.11(a) and 6(b) in relation to Figure 6.11(d) were: 0.60 and 0.65, respectively.

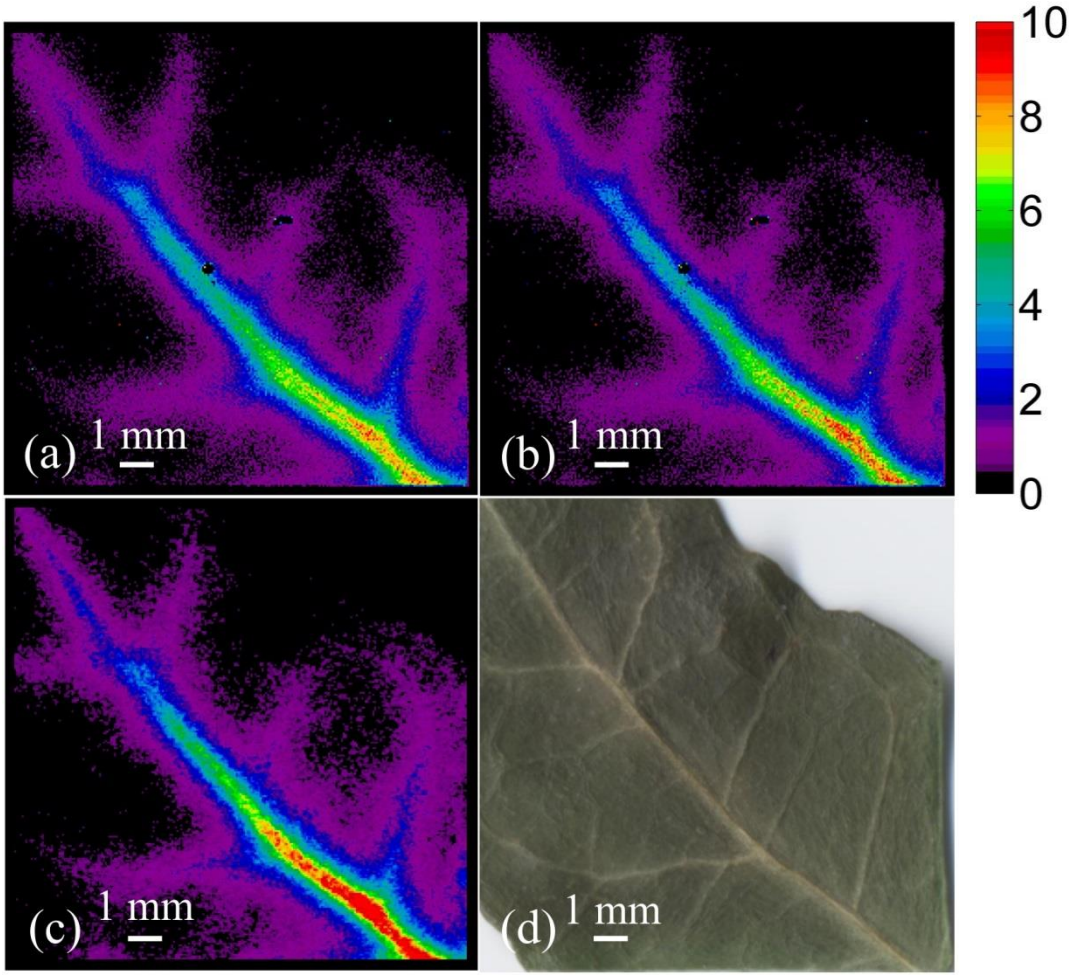

Figure 6.11. Imaging of the vein network of a leaf sample with [^{18}F]FDG uptake. Figure (a) is the positron image applied with energy weighted centroid method applied; figure (b) is the positron image using classification method; figure (c) is the reference phosphor plate image; figure (d) is the optical image of the leaf sample. Figures (a) to (c) are normalized by the global mean and have the same amplitude display limits [0, 10].

6.3. Discussions

A data-driven classification algorithm is put forward to improve the spatial resolution of ^{18}F positron imaging. The proposed algorithm has been tested on the imaging of absorbing edge protocol and a leaf sample. In the absorbing edge protocol designed for observing delicate alterations of spatial resolution, our proposed method can enhance the spatial resolution by 24.2% maximally compared to the former methods. The positron leaf image processed with the proposed algorithm is more similar with the reference images, which have high spatial resolution

and contrast. The proposed method may extend to other particles with similar long trajectories as ^{18}F positrons in the detector, while the advantage of this method may diminish as for particles with relatively short trajectories (*e.g.*, ^{3}H and ^{14}C electrons).

6.3.1. Camera characterization

Several characteristics of ^{18}F positron detection were evaluated by simulation and measurement. The system sensitivity, linearity, energy spectrum and cluster size from the measurements are consistent with the theoretical expectation from simulations. The comparison between experiment and simulation can serve as a valuable tool to improve both the experimental condition and simulation setting.

The Timepix device running in the TOT mode measures the charge collected by individual pixels via the measurement of the width of the preamplifier signal, proportional to the deposited energy [63]. The Timepix operated in the TOT mode outputs a DAC value. As the device contains 65536 independent spectrometric channels and their response is not uniform, energy calibration for each pixel is necessary and implemented. The dependence of DAC value on energy can be modeled by a surrogate function with four parameters, which are determined by measurement and evaluation of the response of each pixel in at least four calibration points [158].

The energy weighted centroid approximation depends on the assumption that more energy is absorbed in the first steps of a particle interacting with the detector than in the later steps, so that the energy weighted centroid can approach to the initial incident position. However, this assumption does not hold for all of the particles, especially for higher energy particles with long track in the detector. The relation of average energy loss of an ionizing particle and the traversed distance in a material made of independent atoms is described by the Bethe-Bloch formula [48]. Based this equation, positrons may also lose their energy mainly in the late steps due to varying incoming angles and velocity. Although it's more appropriate to process the data based on Bethe-Bloch equation, it is not possible to identify the sequence of the fired pixels along the track. Thus this method is not feasible in current measurements.

The sensitivity of positron imaging system is strongly influenced by the medium between the imaging object and the detector. The ability of positron traversing medium is severely limited (up to 2.4 mm in water) due to energy absorption. However, in practice, medium such as Mylar or glass need to be included to protect the detector or to fix the imaging objects. For the analysis of positron imaging or detector properties, the influence of the intermediate medium must be considered. The sensitivity decreases linearly as the thickness of medium increases within a

certain range. According to the simulation, this linear range is up to ~140 μm for Mylar and up to ~100 μm for glass. The decrease of the sensitivity slows down as the thickness of medium increases further. Thus, it is necessary to carefully consider these influences before designing a positron imaging protocol.

6.3.2. The classification feature selection

The training and classification procedures are sensitive to selected features. Improper selection of the features may limit the performance of the algorithm. In this study, seventeen features were selected based on the observable and intrinsic differences of energy and topology among classes.

Positrons lose their energy through inelastic collisions with the atomic electrons when traversing the detector [48]. The average energy lost per distance traversed by an ionizing particle in a material made of independent atoms and due to only inelastic processes (ionization and excitation), is given by the Bethe–Bloch formula. It is found that the speed of energy loss increases as the ionizing particle slows down by analyzing the Bethe-Bloch formula and therefore more energy will deposit in last steps along particle tracking. In this condition, it can be predicted that more pixels excited later can have higher relative energy E_1 and E_2 instead of front pixels (see Figure 4.1(b)).

The topologies of different classes show distinctions as well. A higher energy positron can generate a cluster with the end containing 2×2 groups of pixels, which is caused by the Bragg peak in the energy deposition curve versus track path length [156]. The primary pixels usually appear in the opposite end to the 2×2 groups and are observed with fewer excited neighbors. The primary and the later pixels tend to have different distributions of neighborhood numbers. Thus, the distributions of pixel neighborhood numbers: N_1 and N_2 are chosen as features. Similarly, the features E_3, E_4, E_5, E_6, characterizing the combination of deposited energy and neighbor number, are also selected for learning the classifier. Moreover, considering the Bethe-Bloch formula and Bragg peak, the primary pixels tend to be more distant from the energy weighted centroid of the clusters. Therefore, the normalized pixel distance from the energy-weighted centroid of the belonged cluster is also considered as a classification feature.

In addition, some texture and descriptive indices such as the moment, skewness, kurtosis and entropy of the energy and fired pixel distribution over the neighborhood of the investigated pixels (pixel itself included), which integrate the energy and topology information of the investigated pixels, are adopted to characterize the pixels.

The features selected in this thesis are descriptive indices which have some physical meaning in practice. However, they are still far away from the physics-relevant features. Ideally these features should be derived from the energy scattering principles of positrons in a semiconductor detector. However, such principles can be only described statistically and it is very difficult to find a suitable and quantifiable feature. Although we have selected the features with our best efforts, other suitable features or feature combinations should be explored in future studies. The improvement on the feature selection can further enhance the performance of the proposed algorithm.

6.3.3. Influence of training set on the results

The classification accuracy is affected by the construction of the classifier, which is influenced by the training set. The training set is determined by several factors: the feature selection (as discussed above in section 4.1), the source and the size of training set. A general box-shaped source (dimension: 5 cm × 1.4 cm × 1.4 cm), from which the positrons are emitted randomly, was chosen in the current study to generate the training set. The general source thickness (5 cm) is selected with the consideration that the detector is normally set less than 5 cm from the source due to the short range of beta particles in the medium in most cases of beta imaging. Other sources have been tested to investigate their influences on the classification results, such as box sources (*e. g.*, dimension: 2.5 cm × 1.4 cm × 1.4 cm), plane sources (ultra-thin cubic, parallel to the detector) and point sources. The results have shown that they can generate similar feature spectra and classification results as the proposed general source. Therefore the classifier originating from the proposed source can provide relatively stable results and can be applied to variable measurement protocols.

The classifier stability depends on the size of the training set. The detected clusters should be over-sampled due to sensitivity loss. Different numbers of positron emissions (5×10^3, 10^4, 5×10^4, 10^5, 5×10^5 and 10^6) have been tested by simulation. The simulated detection sensitivity is assessed to be ≈0.056 cps/Bq using the general source proposed. It is found that the classifier reaches equilibrium (*i.e.*, obtain stable results) starting at $\approx5\times10^4$ positrons emissions. In this study, the classifier is learned by topological and energy information induced by 10^5 incident positrons.

The classification model built in the current study covers a wide scenario of beta imaging. For some special applications (*e.g.*, positron traversing another medium before entering the positron camera), the training set can be adapted for the specific situation.

6.3.4. Charge diffusion effect

The electron-hole pairs, generated by deposited energy in the detector, diffuse before their collection by the electrodes. The deposited energy diffusion is a surrogate of the diffusion of electron-hole pairs. For a fired pixel, the detector output energy does not indicate the energy deposited completely within this pixel, but also includes partial energies deposited in neighbor pixels, which diffused into the current pixel. The charge diffusion effect may change the pixel energy spectrum and pixel topology. Its influence on the classification has been evaluated [152].

Timepix is operated under high bias voltage (100 V) and the sensitive layer is over-depleted. The electron-hole pairs generated in the sensitive layer can be collected by electrodes within a short time. The maximum possible collection time of the Timepix detector is estimated to be 36.8 ns by simulation (suppose the interaction happens at 300 μm from the collection electrode, the mobility of holes in silicon is 250 $cm^2/V/s$ [184]). It is concluded that more than 97% of the energy is deposited within one pixel due to the short collection time. Even for the possible maximum energy deposition (633 keV), the energy diffused to neighbor pixels is below the energy threshold (≈3.4 keV). Thus, the charge diffusion effect is expected to be less than one pixel. The energy spectrum and topology of pixels are almost unchanged. Thus, the charge diffusion effect does not influence the detection and simulation results significantly and was therefore not included in the simulation.

6.3.5. Spatial resolution vs. sensitivity

It is estimated by simulation that (5.8±1.2)% of 3-pixel clusters, (21.4±0.6)% of 4-pixel clusters, (24.6±2.1)% of 5-pixel clusters, and (32.3±2.2)% of more-pixel clusters are not correctly classified. The imaging sensitivity decreases by 16.6% on average as observed in the absorbing edge protocol. This sensitivity loss can be compensated by energy weighted centroid approximation in the proposed method, although the compensation worsens the spatial resolution by 6.3%. In the application of imaging a radioactive leaf sample, the compensation maintains the sensitivity (the sensitivity decreased by ≈23.9% without compensation), while the spatial resolution did not show obvious degradation. Therefore, we suggest compensating the sensitivity in particular for the measurements with low radioactive doses and dynamic imaging (short image acquisition time).

The misclassification, in particular the mixture of second and third pixels, limits the improvement of spatial resolution and the influence was estimated by simulation. An ideal ^{18}F point source was used for the theoretical spatial resolution assessment. The spatial resolution of

the image composed of only primary pixels is 58.9 μm, composed of both primary and second pixels is 69.6 μm, and composed of the mixture of primary, second and third pixels is 71.0 μm, in comparison with 138.4 μm spatial resolution of the image formed by all pixels. The proportions of second and third pixels are mixed here in consistency with measurements. Theoretically, the spatial resolution of an ^{18}F positron image can be enhanced 2.35-fold by selecting only primary pixels and the mixture of second and third pixels adds another 7.7% and 8.7% loss in spatial resolution. The involvement of second and third pixels helps to maintain the sensitivity, while it imposes relatively low influence on the spatial resolution.

Clusters with 2 fired pixels have shown lower classification accuracy than those with more fired pixels as their classification depends only on the energy features. For these clusters, simulations have shown a higher probability of the pixel with higher energy being the second pixel (67.6% of all 2-pixel clusters). In spite of a more frequent misclassification, the spatial resolution is influenced insignificantly since only 7.7% spatial resolution degradation can be introduced maximally for 2-pixel clusters. The treatment of 2-pixel clusters is more flexible. The energy weighted approximation can be an option. The hybrid method (energy weighted approximation for 2-pixel cluster and classification for longer clusters) may bring some advantages. The major reason responsible for spatial resolution loss is the misclassification and classifier failure on pixel-rich clusters.

6.3.6. Limitations

The proposed method is based on the assumption that the classifier learned by simulation data can be transferred to predict the measured data. However, discrepancies may exist between the Monte-Carlo simulation of a positron passing through the detector and the realistic physical procedure. The procedures of electron-hole pair collection and signal output also introduce deviations of simulation from the measurement. Therefore, the model learned by simulation data may introduce errors on the classification results. The optimal spatial resolution may not be achieved. However, it is impossible to acquire the experimental training data from direct measurements due to the hardware limitation. As Monte-Carlo simulation using Geant4 is widely validated in many applications [151], the construction of training sets using this realistic simulation is practical to transfer the theoretical knowledge in measurements. Improvement of the Monte-Carlo simulation may further enhance the performance of the proposed method.

Although there are statistics (*i.e.*, RMSE and Dice coefficient) to support the improvement of the algorithm on the leaf positron images, this improvement is hardly visible. The leaf veins have no clear sharp boundaries to sufficiently demonstrate the advantages of the proposed algorithm.

Nevertheless, this example with relatively fine structures could already explore the improvement with better preservation of the algorithm.

Around 10%~15% difference of normalized amplitude between the imaging using the positron camera and phosphor plate has been observed. The spatial resolution and contrast of a phosphor image are higher with direct exposure of the plate to beta particles or gammas [185] and smaller scanner pixel size. The scattering of positrons decreases the spatial resolution of the positron camera images and introduces partial volume effect, which is possibly one reason for the amplitude difference on the two types of images. Another reason may lie in the nonlinearity of phosphor imaging when the phosphor screen is exposed to low radioactivities. In addition, the errors from registration of positron and phosphor images and segmentation of field of interest may also lead to image amplitude difference. Here we used the phosphor image as a reference for the assessment of the effect of energy information from Timepix. It is not expected that the Timepix could outperform phosphor imaging plate. Nevertheless, the Timepix detector characterized by its high time resolution and capability of particle energy information acquisition has shown its potential for in-vitro and in-vivo dynamic imaging.

The scanned optical image as another reference has high spatial resolution. The similarity (characterized by Dice coefficient) between the positron and the optical image was employed to evaluate the spatial resolution of positron image. The differences between the optical and the positron image may still exist due to the following reasons: (1) The leaf cannot absorb the tracer thoroughly, so the positron radiation cannot be detected throughout the whole leaf; (2) the positron image is more affected by multiple scattering/partial volume effect; (3) image registration and segmentation errors.

6.4. Conclusions

In this chapter, Timepix was tested for positron measurement and the contributions of energy information were assessed experimentally and theoretically. Our results show that a slight enhancement of sensitivity and resolution can be achieved when recording the deposited energy in Timepix detector. Thus, a positron camera based on Timepix chip is proposed for positron imaging. As an imaging device with real-time single pixel read out (100 kHz), this positron camera based on Timepix has the potential to capture dynamic signals (*e.g.*, signals of microfluidic radioassays [18]).

With the characteristics knowledge of positron imaging, we have proposed a classification-based method to enhance the spatial resolution of ^{18}F positron imaging. By classifying the primarily

fired pixels of incident positrons, this method can reduce the influence of positron multiple-scattering on the spatial resolution of the positron camera. Enhancement of spatial resolution (up to 24.2%) has been achieved with the proposed method. Although these improvements only lead to slight visual advantage, it is encouraging to investigate the proposed algorithm further for the enhancement of sophisticated positron imaging in clinical and preclinical applications. The proposed classification method may be further extended to the imaging of other particles, which have high maximum energies and long trajectories with hardly recognizable primary pixels in the detector.

7. Summary

Molecular imaging has been used extensively on the investigation of tumor metabolism. However the physiological and systematic interpretations of tumor metabolism images are limited. The thesis interprets the signal mechanisms of positron imaging of tumor metabolism by advanced computational modeling methods. Computational modeling was systematically applied on the whole procedure of positron detection in solid tumor for the comprehensive understanding of signal formation mechanisms. The in-depth understanding of positron signals supports the development of tumor detection, therapy planning and monitoring. In particular, this thesis made the following two theoretical contributions: (I) a novel computational modeling method of tumor pathophysiology; (II) the first machine learning algorithm in the processing of positron signals for the enhancement of spatial resolution.

I. Computational models of tumor pathophysiology are proposed for the deep understanding of fundamental molecular pathways and metabolites interaction inside tumors. Compared with previous models, the current models integrate the mediations of physiological regulators (such as enzymes and transporters) into the tumor microenvironment to explore the quantitative relationship between the metabolism behind molecular imaging and the underlying phenotypes. More comprehensive substrates are introduced in the proposed models, which enables the explanation of complicated tumor metabolic phenomenon. The contributions of this computational modeling are listed as follows:

- Theoretical advancements have been made to model the complex interactions of a wide spectrum of metabolites (such as oxygen, glucose, FDG, lactate, protons, and other key ions) relating to tumor metabolism. In particular, for glucose, lactate and FDG, both extra- and intra-cellular components are simulated in the mediations of transporters (GLUT and MCTs). The majority of simulated substrate concentrations are validated to fall in the range of reported experimental data.
- Reaction-diffusion schemes incorporating with protein regulation kinetics are developed to enable the modeling of the influences of key transporter (GLUT) and enzyme (HK) during FDG uptake simulation. The simulated spatio-temporal FDG uptake and tissue activity curves are analyzed under different GLUT and HK kinetic parameters, and they can serve as the predictions of FDG PET measurements after the validation. The influences of vascular density on FDG uptake are also estimated.
- It is the first time to establish the quantitative relationship between the tumor phenotypes (*i.e.*, pathophysiological factors, such as transporter and enzyme expression levels, and

microvessel distributions) and metabolisms (represented by substrate distributions) using the proposed models. Analytic parameters are introduced to quantify the influences of multiple pathophysiological factors on tumor metabolisms.

- The computational models bring in-depth insights into the physiological phenomena observed in the experiments. For example, GLUT is more influential to glycolytic flux than HK; extracellular pH is not correlated with MCT expressions, *etc.*
- The computational modeling of tumor pathophysiology assists the generation of hypotheses to bridge the discrepancy between tumor metabolism and tumor phenotypes. It has the potential to accelerate the development of multi-modal imaging strategies for assessment of tumor phenotypes.

II. In order to reduce the effect of multiple scattering on the imaging with position-sensitive positron camera and improve the spatial resolution, a novel data-driven method is proposed based on the classification of primary pixels fired by positrons within the (Timepix) detector using support vector machine. A classification model is introduced to learn the features of fired pixels based on the data derived from Monte-Carlo simulations using Geant4. The primarily fired pixels along positron tracks in the measurements are estimated using the proposed classification method. The contributions of the method are as follows:

- We formulate the scattering-degraded resolution problem in a silicon detector into a classification problem and solve it using a supervised learning strategy. The proposed algorithm can be integrated into hardware to improve the spatial resolution of particle imaging.
- Monte-Carlo simulation is introduced to solve the problem where no training data is possible to obtain using current measurement technologies. The Monte-Carlo simulation systematically emulates the positron passing through and firing pixels in the silicon detector, and provides all the characteristics of positron scattering.
- Advanced topological and energy features are extracted for the supervised learning of classification model.
- A set of physical experiments are designed and carried on for systematic validation of the proposed algorithm. The positive results from the validation support the further investigation of the proposed classification algorithm for the enhancement of positron imaging performance in clinical and preclinical applications, and promote the direct positron imaging put into more delicate preclinical applications (such as cell metabolism monitoring).

Bibliography

1. Gambhir, S.S., *Molecular imaging of cancer with positron emission tomography.* Nature Reviews Cancer, 2002. **2**(9): p. 683-693.
2. Haberkorn, U., et al., *Molecular imaging of tumor metabolism and apoptosis.* Oncogene, 2011. **30**(40): p. 4141-4151.
3. Weissleder, R. and S.S. Gambhir, *Molecular imaging: principles and practice*. 2010: PMPH-USA.
4. Fox, M.D. and M.E. Raichle, *Spontaneous fluctuations in brain activity observed with functional magnetic resonance imaging.* Nature Reviews Neuroscience, 2007. **8**(9): p. 700-711.
5. Kim, R.J., et al., *The use of contrast-enhanced magnetic resonance imaging to identify reversible myocardial dysfunction.* New England Journal of Medicine, 2000. **343**(20): p. 1445-1453.
6. Houssami, N., et al., *Accuracy and surgical impact of magnetic resonance imaging in breast cancer staging: systematic review and meta-analysis in detection of multifocal and multicentric cancer.* Journal of Clinical Oncology, 2008. **26**(19): p. 3248-3258.
7. Weissleder, R. and U. Mahmood, *Molecular Imaging 1.* Radiology, 2001. **219**(2): p. 316-333.
8. Kovar, J.L., et al., *A systematic approach to the development of fluorescent contrast agents for optical imaging of mouse cancer models.* Analytical Biochemistry, 2007. **367**(1): p. 1-12.
9. Chen, K., J. Xie, and X. Chen, *RGD-human serum albumin conjugates as efficient tumor targeting probes.* Molecular Imaging, 2009. **8**(2): p. 65-73.
10. Kovar, J.L., et al., *Hyaluronidase expression induces prostate tumor metastasis in an orthotopic mouse model.* The American Journal of Pathology, 2006. **169**(4): p. 1415-1426.
11. Kovar, J.L., et al., *Characterization and performance of a near-infrared 2-deoxyglucose optical imaging agent for mouse cancer models.* Analytical Biochemistry, 2009. **384**(2): p. 254-262.
12. Humblet, V., et al., *High-affinity near-infrared fluorescent small-molecule contrast agents for in vivo imaging of prostate-specific membrane antigen.* Molecular Imaging, 2005. **4**(4): p. 448-462.
13. Elhendy, A., J.J. Bax, and D. Poldermans, *Dobutamine stress myocardial perfusion imaging in coronary artery disease.* Journal of Nuclear Medicine, 2002. **43**(12): p. 1634-1646.
14. Bonte, F.J., et al., *Tc-99m HMPAO SPECT in the differential diagnosis of the dementias with histopathologic confirmation.* Clinical Nuclear Medicine, 2006. **31**(7): p. 376-378.
15. Henderson, T.A., *The diagnosis and evaluation of dementia and mild cognitive impairment with emphasis on SPECT perfusion neuroimaging.* CNS Spectrums, 2012. **17**(04): p. 176-206.
16. Bailey, D.L., et al., *Positron emission tomography*. 2005: Springer.
17. Phelps, M.E., *Positron emission tomography provides molecular imaging of biological processes.* Proceedings of the National Academy of Sciences, 2000. **97**(16): p. 9226-9233.
18. Vu, N.T., et al., *A β-camera integrated with a microfluidic chip for radioassays based on real-time imaging of glycolysis in small cell populations.* Journal of Nuclear Medicine, 2011. **52**(5): p. 815-821.
19. Chen, L., et al., *Direct imaging of radionuclide-produced electrons and positrons with an ultrathin phosphor.* Journal of Nuclear Medicine, 2008. **49**(7): p. 1141-1145.
20. Lauria, A., et al., *Experimental study for an intraoperative probe for 18F imaging with a silicon pixel detector.* Nuclear Instruments and Methods in Physics Research Section A: Accelerators, Spectrometers, Detectors and Associated Equipment, 2007. **576**(1): p. 198-203.
21. Vaupel, P. *Tumor microenvironmental physiology and its implications for radiation oncology*. in *Seminars in Radiation Oncology*. 2004. Elsevier.
22. Hanahan, D. and R.A. Weinberg, *The hallmarks of cancer.* Cell. **100**(1): p. 57-70.
23. Konerding, M., et al., *Evidence for characteristic vascular patterns in solid tumours: quantitative studies sing corrosion casts.* British Journal of Cancer, 1999. **80**(5-6): p. 724-732.

24. Konerding, M., E. Fait, and A. Gaumann, *3D microvascular architecture of pre-cancerous lesions and invasive carcinomas of the colon.* British Journal of Cancer, 2001. **84**(10): p. 1354-1362.
25. Chaplain, M.A., S.R. McDougall, and A. Anderson, *Mathematical modeling of tumor-induced angiogenesis.* Annual Review of Biomedical Engineering, 2006. **8**: p. 233-257.
26. Risau, W., *Mechanisms of angiogenesis.* Nature, 1997. **386**(6626): p. 671-674.
27. Molls, M., et al., *The impact of tumor biology on cancer treatment and multidisciplinary strategies*. 2009: Springer.
28. Airley, R., et al., *Glucose transporter glut-1 expression correlates with tumor hypoxia and predicts metastasis-free survival in advanced carcinoma of the cervix.* Clinical Cancer Research, 2001. **7**(4): p. 928-934.
29. Wolf, A., et al., *Hexokinase 2 is a key mediator of aerobic glycolysis and promotes tumor growth in human glioblastoma multiforme.* The Journal of Experimental Medicine, 2011. **208**(2): p. 313-326.
30. Ullah, M.S., A.J. Davies, and A.P. Halestrap, *The plasma membrane lactate transporter MCT4, but not MCT1, is up-regulated by hypoxia through a HIF-1α-dependent mechanism.* Journal of Biological Chemistry, 2006. **281**(14): p. 9030-9037.
31. Boidot, R., et al., *Regulation of monocarboxylate transporter MCT1 expression by p53 mediates inward and outward lactate fluxes in tumors.* Cancer Research, 2012. **72**(4): p. 939-948.
32. Liu, Y., et al., *Hypoxia regulates vascular endothelial growth factor gene expression in endothelial cells identification of a 5' enhancer.* Circulation Research, 1995. **77**(3): p. 638-643.
33. Bayer, C., et al., *Acute versus chronic hypoxia: why a simplified classification is simply not enough.* International Journal of Radiation Oncology Biology Physics, 2011. **80**(4): p. 965-968.
34. Mönnich, D., et al., *Modelling and simulation of the influence of acute and chronic hypoxia on [18F] fluoromisonidazole PET imaging.* Physics in Medicine and Biology, 2012. **57**(6): p. 1675-1684.
35. Travasso, R.D., et al., *Tumor angiogenesis and vascular patterning: a mathematical model.* PloS One, 2011. **6**(5): p. e19989.
36. Ke, Q. and M. Costa, *Hypoxia-inducible factor-1 (HIF-1).* Molecular Pharmacology, 2006. **70**(5): p. 1469-1480.
37. Semenza, G.L., *Hypoxia-inducible factor 1: master regulator of O_2 homeostasis.* Current Opinion in Genetics & Development, 1998. **8**(5): p. 588-594.
38. Semenza, G.L., *Targeting HIF-1 for cancer therapy.* Nature Reviews Cancer, 2003. **3**(10): p. 721-732.
39. Warburg, O., *On the origin of cancer cells.* Science, 1956. **123**(3191): p. 309-314.
40. Fletcher, J.W., et al., *Recommendations on the use of 18F-FDG PET in oncology.* Journal of Nuclear Medicine, 2008. **49**(3): p. 480-508.
41. Mosconi, L., et al., *Pre-clinical detection of Alzheimer's disease using FDG-PET, with or without amyloid imaging.* Journal of Alzheimer's Disease, 2010. **20**(3): p. 843-854.
42. Kennedy, K.M. and M.W. Dewhirst, *Tumor metabolism of lactate: the influence and therapeutic potential for MCT and CD147 regulation.* Future Oncology, 2010. **6**(1): p. 127-148.
43. Sonveaux, P., et al., *Targeting lactate-fueled respiration selectively kills hypoxic tumor cells in mice.* The Journal of Clinical Investigation, 2008. **118**(12): p. 3930-3942.
44. Wang, Q. and M.E. Morris, *The role of monocarboxylate transporter 2 and 4 in the transport of γ-hydroxybutyric acid in mammalian cells.* Drug Metabolism and Disposition, 2007. **35**(8): p. 1393-1399.
45. Schwickert, G., et al., *Correlation of high lactate levels in human cervical cancer with incidence of metastasis.* Cancer Research, 1995. **55**(21): p. 4757-4759.
46. Walenta, S. and W.F. Mueller-Klieser. *Lactate: mirror and motor of tumor malignancy*. in *Seminars in Radiation Oncology*. 2004. Elsevier.

47. Vinnakota, K.C. and D.A. Beard, *Kinetic analysis and design of experiments to identify the catalytic mechanism of the monocarboxylate transporter isoforms 4 and 1*. Biophysical Journal, 2011. **100**(2): p. 369-380.
48. Levin, C.S. and E.J. Hoffman, *Calculation of positron range and its effect on the fundamental limit of positron emission tomography system spatial resolution.* Physics in Medicine and Biology, 1999. **44**(3): p. 781-799.
49. Harrison, R., et al. *Positron range and coincidence non-collinearity in SimSET*. in *Nuclear Science Symposium, 1999. Conference Record. 1999 IEEE*. 1999. IEEE.
50. Shields, A.F., et al., *Imaging proliferation in vivo with [F18] FLT and positron emission tomography*. Nature Medicine, 1998. **4**(11): p. 1334-1336.
51. Fahey, F.H., *Data acquisition in PET imaging.* Journal of Nuclear Medicine Technology, 2002. **30**(2): p. 39-49.
52. Khan, T.S., et al., *11C-metomidate PET imaging of adrenocortical cancer.* European Journal of Nuclear Medicine and Molecular Imaging, 2003. **30**(3): p. 403-410.
53. Minn, H., et al., *Imaging of adrenal incidentalomas with PET using 11C-metomidate and 18F-FDG.* Journal of Nuclear Medicine, 2004. **45**(6): p. 972-979.
54. Luster, M., et al., *Clinical value of 18F-fluorodihydroxyphenylalanine positron emission tomography/computed tomography (18F-DOPA PET/CT) for detecting pheochromocytoma.* European Journal of Nuclear Medicine and Molecular Imaging, 2010. **37**(3): p. 484-493.
55. Kantarci, K. and C.R. Jack Jr, *Neuroimaging in Alzheimer disease: an evidence-based review.* Neuroimaging Clinics of North America, 2003. **13**(2): p. 197-209.
56. Leyton, M., et al., *Amphetamine-induced increases in extracellular dopamine, drug wanting, and novelty seeking: a PET/[11C] raclopride study in healthy men.* Neuropsychopharmacology, 2002. **27**(6): p. 1027-1035.
57. Gründer, G., et al., *Brain and plasma pharmacokinetics of aripiprazole in patients with schizophrenia: an [18F] fallypride PET study.* American Journal of Psychiatry, 2008. **165**(8): p. 988-995.
58. Schreckenberger, M., et al., *The dopamine D2 receptor ligand 18F-desmethoxyfallypride: an appropriate fluorinated PET tracer for the differential diagnosis of parkinsonism.* European Journal of Nuclear Medicine and Molecular Imaging, 2004. **31**(8): p. 1128-1135.
59. Suehiro, M., et al., *A PET radiotracer for studying serotonin uptake sites: carbon-11-McN-5652Z.* Journal of Nuclear Medicine, 1993. **34**(1): p. 120-127.
60. Meyer, J.H., et al., *Occupancy of serotonin transporters by paroxetine and citalopram during treatment of depression: a [11C] DASB PET imaging study.* American Journal of Psychiatry, 2001. **158**(11): p. 1843-1849.
61. Rudd, J.H., et al., *Imaging atherosclerotic plaque inflammation with [18F]-fluorodeoxyglucose positron emission tomography*. Circulation, 2002. **105**(23): p. 2708-2711.
62. Oi, N., et al., *FDG-PET imaging of lower extremity muscular activity during level walking.* Journal of Orthopaedic Science, 2003. **8**(1): p. 55-61.
63. Esposito, M., et al., *Energy sensitive Timepix silicon detector for electron imaging.* Nuclear Instruments and Methods in Physics Research Section A: Accelerators, Spectrometers, Detectors and Associated Equipment, 2011. **652**(1): p. 458-461.
64. Pratx, G., et al., *Radioluminescence microscopy: measuring the heterogeneous uptake of radiotracers in single living cells.* PloS One, 2012. **7**(10): p. e46285.
65. Pratx, G., et al., *High-Resolution Radioluminescence Microscopy of 18F-FDG Uptake by Reconstructing the β-Ionization Track.* Journal of Nuclear Medicine, 2013. **54**(10): p. 1841-1846.
66. Ott, R., J. MacDonald, and K. Wells, *The performance of a CCD digital autoradiography imaging system.* Physics in Medicine and Biology, 2000. **45**(7): p. 2011-2027.
67. Kokkinou, E., et al., *Digital autoradiography imaging using direct irradiation of a CCD between 278-309 K.* IEEE Transactions on Nuclear Science, 2003. **50**(5): p. 1702-1707.

68. Cabello, J. and K. Wells, *The spatial resolution of silicon-based electron detectors in β-autoradiography.* Physics in Medicine and Biology, 2010. **55**(6): p. 1677-1699.
69. Barthe, N., et al., *Recent technologic developments on high-resolution beta imaging systems for quantitative autoradiography and double labeling applications.* Nuclear Instruments and Methods in Physics Research Section A: Accelerators, Spectrometers, Detectors and Associated Equipment, 2004. **527**(1): p. 41-45.
70. Karellas, A., et al., *Imaging of radionuclide emissions with a low-noise charge-coupled device.* IEEE Transactions on Nuclear Science, 1993. **40**(4): p. 979-982.
71. Barthe, N., et al., *Recent technologic developments on high-resolution beta imaging systems for quantitative autoradiography and double labeling applications.* Nucl. Instrum. Meth. A, 2004. **527**(1): p. 41-45.
72. Abate, L., et al., *GaAs pixel arrays for β imaging in medicine and biology.* Nuclear Instruments and Methods in Physics Research Section A: Accelerators, Spectrometers, Detectors and Associated Equipment, 2001. **460**(1): p. 97-106.
73. Bertolucci, E., et al., *BETAview: a digital β-imaging system for dynamic studies of biological phenomena.* Nuclear Instruments and Methods in Physics Research Section A: Accelerators, Spectrometers, Detectors and Associated Equipment, 2002. **478**(1): p. 109-113.
74. Mettivier, G., M.C. Montesi, and P. Russo, *First images of a digital autoradiography system based on a Medipix2 hybrid silicon pixel detector.* Physics in Medicine and Biology, 2003. **48**(12): p. N173-81.
75. Mettivier, G., M. Cristina Montesi, and P. Russo, *Tritium digital autoradiography with a Medipix2 hybrid silicon pixel detector.* Nuclear Instruments and Methods in Physics Research Section A: Accelerators, Spectrometers, Detectors and Associated Equipment, 2004. **516**(2): p. 554-563.
76. Mettivier, G., M. Montesi, and P. Russo, *Digital autoradiography with a Medipix2 hybrid silicon pixel detector.* IEEE Transactions on Nuclear Science, 2005. **52**(1): p. 46-50.
77. Esposito, M., G. Mettivier, and P. Russo, *14C autoradiography with an energy-sensitive silicon pixel detector.* Physics in Medicine and Biology, 2011. **56**(7): p. 1947-1965.
78. Byrne, H.M., *Dissecting cancer through mathematics: from the cell to the animal model.* Nature Reviews Cancer, 2010. **10**(3): p. 221-230.
79. Casciari, J., S. Sotirchos, and R. Sutherland, *Mathematical modelling of microenvironment and growth in EMT6/Ro multicellular tumour spheroids.* Cell Proliferation, 1992. **25**(1): p. 1-22.
80. Molavian, H.R., et al., *Fingerprint of cell metabolism in the experimentally observed interstitial pH and pO_2 in solid tumors.* Cancer Research, 2009. **69**(23): p. 9141-9147.
81. Helmlinger, G., et al., *Interstitial pH and pO_2 gradients in solid tumors in vivo: high-resolution measurements reveal a lack of correlation.* Nature Medicine, 1997. **3**(2): p. 177-182.
82. Daşu, A., I. Toma-Daşu, and M. Karlsson, *Theoretical simulation of tumour oxygenation and results from acute and chronic hypoxia.* Physics in Medicine and Biology, 2003. **48**(17): p. 2829-2842.
83. Kelly, C.J. and M. Brady, *A model to simulate tumour oxygenation and dynamic [18F]-Fmiso PET data.* Physics in Medicine and Biology, 2006. **51**(22): p. 5859-5873.
84. Dalah, E., D. Bradley, and A. Nisbet, *Simulation of tissue activity curves of 64Cu-ATSM for sub-target volume delineation in radiotherapy.* Physics in Medicine and Biology, 2010. **55**(3): p. 681-694.
85. Petit, S.F., et al., *Intra-voxel heterogeneity influences the dose prescription for dose-painting with radiotherapy: a modelling study.* Physics in Medicine and Biology, 2009. **54**(7): p. 2179-2196.
86. Mönnich, D., et al., *Modelling and simulation of [18F] fluoromisonidazole dynamics based on histology-derived microvessel maps.* Physics in Medicine and Biology, 2011. **56**(7): p. 2045-2057.
87. Mantzaris, N.V., S. Webb, and H.G. Othmer, *Mathematical modeling of tumor-induced angiogenesis.* Journal of Mathematical Biology, 2004. **49**(2): p. 111-187.

88. Newman, J. and K.E. Thomas-Alyea, *Electrochemical systems*. 2012: John Wiley & Sons.
89. Bisswanger, H., *Enzyme Kinetics*, in *Enzyme Kinetics*. 2005, Wiley-VCH Verlag GmbH & Co. KGaA. p. 51-160.
90. Bishop, C.M., *Pattern recognition and machine learning*. Vol. 4. 2006: springer New York.
91. Li, R., et al., *Deep learning based imaging data completion for improved brain disease diagnosis*, in *Medical Image Computing and Computer-Assisted Intervention–MICCAI 2014*. 2014, Springer. p. 305-312.
92. Stough, J.V., et al., *Automatic method for thalamus parcellation using multi-modal feature classification*, in *Medical Image Computing and Computer-Assisted Intervention–MICCAI 2014*. 2014, Springer. p. 169-176.
93. Zhu, X., H.I. Suk, and D. Shen, *Multi-modality canonical feature selection for Alzheimer's disease diagnosis*, in *Medical Image Computing and Computer-Assisted Intervention–MICCAI 2014*. 2014, Springer. p. 162-169.
94. Zhu, X., H.I. Suk, and D. Shen, *A novel multi-relation regularization method for regression and classification in AD diagnosis*, in *Medical Image Computing and Computer-Assisted Intervention–MICCAI 2014*. 2014, Springer. p. 401-408.
95. Gao, F., H. Liu, and P. Shi, *Patient-adaptive lesion metabolism analysis by dynamic PET images*, in *Medical Image Computing and Computer-Assisted Intervention–MICCAI 2012*. 2012, Springer. p. 558-565.
96. Gao, F., et al., *Reinforcement learning based model selection and parameter estimation for pharmacokinetic analysis in drug selection*, in *Augmented Reality Environments for Medical Imaging and Computer-Assisted Interventions*. 2013, Springer. p. 221-230.
97. Seber, G.A. and A.J. Lee, *Linear regression analysis*. Vol. 936. 2012: John Wiley & Sons.
98. Neter, J., et al., *Applied linear statistical models*. Vol. 4. 1996: Irwin Chicago.
99. Bates, D.M. and D.G. Watts, *Nonlinear regression: iterative estimation and linear approximations*. 1988: Wiley Online Library.
100. Boser, B.E., I.M. Guyon, and V.N. Vapnik. *A training algorithm for optimal margin classifiers*. in *Proceedings of the fifth annual workshop on Computational learning theory*. 1992. ACM.
101. Cortes, C. and V. Vapnik, *Support-vector networks.* Machine Learning, 1995. **20**(3): p. 273-297.
102. Chang, C. and C. Lin, *LIBSVM: a library for support vector machines.* ACM Transactions on Intelligent Systems and Technology (TIST), 2011. **2**(3): p. 1-27.
103. Jie, B., D. Shen, and D. Zhang, *Brain Connectivity Hyper-Network for MCI Classification*, in *Medical Image Computing and Computer-Assisted Intervention–MICCAI 2014*. 2014, Springer. p. 724-732.
104. Matoug, S., et al. *Predicting Alzheimer's disease by classifying 3D-Brain MRI images using SVM and other well-defined classifiers*. in *Journal of Physics: Conference Series*. 2012. IOP Publishing.
105. Morris, E.D., et al., *Kinetic modeling in positron emission tomography*. Emission Tomography: The Fundamentals of PET and SPECT. Academic, San Diego, 2004.
106. Patlak, C.S., R.G. Blasberg, and J.D. Fenstermacher, *Graphical Evaluation of Blood-to-Brain Transfer Constants from Multiple-Time Uptake Data.* Journal of Cerebral Blood Flow & Metabolism, 1983. **3**(1): p. 1-7.
107. Patlak, C.S. and R.G. Blasberg, *Graphical Evaluation of Blood-to-Brain Transfer Constants from Multiple-Time Uptake Data. Generalizations.* Journal of Cerebral Blood Flow & Metabolism, 1985. **5**(4): p. 584-590.
108. Logan, J., et al., *Graphical analysis of reversible radioligand binding from time-activity measurements applied to [N-11C-methyl]-(-)-Cocaine PET studies in human subjects.* Journal of Cerebral Blood Flow & Metabolism, 1990. **10**(5): p. 740-747.
109. Vaupel, P., A. Mayer, and M. Höckel, *Tumor hypoxia and malignant progression.* Methods in Enzymology, 2003. **381**: p. 335-354.

110. Mathupala, S., Y. Ko, and P. Pedersen, *Hexokinase II: cancer's double-edged sword acting as both facilitator and gatekeeper of malignancy when bound to mitochondria.* Oncogene, 2006. **25**(34): p. 4777-4786.
111. Aronen, H.J., et al., *High microvascular blood volume is associated with high glucose uptake and tumor angiogenesis in human gliomas.* Clinical Cancer Research, 2000. **6**(6): p. 2189-2200.
112. Mayer, A. and P. Vaupel, *Hypoxia, lactate accumulation, and acidosis: siblings or accomplices driving tumor progression and resistance to therapy?* Adv. Exp. Med. Biol. , 2013. **789**: p. 203-209.
113. Kennedy, K.M. and M.W. Dewhirst, *Tumor metabolism of lactate: the influence and therapeutic potential for MCT and CD147 regulation.* Future Oncol., 2009. **6**(1): p. 127-148.
114. Whitaker-Menezes, D., et al., *Evidence for a stromal-epithelial "lactate shuttle" in human tumors: MCT4 is a marker of oxidative stress in cancer-associated fibroblasts.* Cell Cycle, 2011. **10**(11): p. 1772-1783.
115. Bonen, A., *The expression of lactate transporters (MCT1 and MCT4) in heart and muscle.* European Journal of Applied Physiology, 2001. **86**(1): p. 6-11.
116. Shi, K., et al. *A flow-limited oxygen-dependent diffusion model using heterogeneous perfusion for quantitative analysis of dynamic [18F] FMISO PET*. in *Society of Nuclear Medicine Annual Meeting Abstracts*. 2011. Soc Nuclear Med.
117. Kelly, C., K. Smallbone, and M. Brady, *Tumour glycolysis: the many faces of HIF*. Journal of Theoretical Biology, 2008. **254**(2): p. 508-513.
118. Mueckler, M., *Facilitative glucose transporters.* European Journal of Biochemistry, 1994. **219**(3): p. 713-725.
119. Dimmer, K., et al., *The low-affinity monocarboxylate transporter MCT4 is adapted to the export of lactate in highly glycolytic cells.* Biochemical Journal, 2000. **350**: p. 219-227.
120. Carpenter, L. and A.P. Halestrap, *The kinetics, substrate and inhibitor specificity of the lactate transporter of Ehrlich-Lettre tumour cells studied with the intracellular pH indicator BCECF*. Biochemical Journal, 1994. **304**: p. 751-760.
121. Wilson, M.C., et al., *Lactic acid efflux from white skeletal muscle is catalyzed by the monocarboxylate transporter isoform MCT3.* Journal of Biological Chemistry, 1998. **273**(26): p. 15920-15926.
122. Li, Y., et al., *Catalysis and pH control by membrane-associated carbonic anhydrase IX in MDA-MB-231 breast cancer cells.* Journal of Biological Chemistry, 2011. **286**(18): p. 15789-15796.
123. Vaupel, P., *The pathophysiology of the tumor microenvironment: Coping with hostile conditions and spatio-temporal heterogeneities.* 2014.
124. Garg, L.C. and T.H. Maren, *The rates of hydration of carbon dioxide and dehydration of carbonic acid at 37.* Biochimica et Biophysica Acta (BBA)-General Subjects, 1972. **261**(1): p. 70-76.
125. Chen, C., et al., *Regulation of glut1 mRNA by hypoxia-inducible factor-1 Interaction between H-ras and hypoxia.* Journal of Biological Chemistry, 2001. **276**(12): p. 9519-9525.
126. Wada, H., et al., *Expression pattern of angiogenic factors and prognosis after hepatic resection in hepatocellular carcinoma: importance of angiopoietin-2 and hypoxia-induced factor-1a.* Liver International, 2006. **26**(4): p. 414-423.
127. Jiang, B.H., et al., *Hypoxia-inducible factor 1 levels vary exponentially over a physiologically relevant range of O_2 tension.* American Journal of Physiology-Cell Physiology, 1996. **40**(4): p. C1172-1180.
128. Leedale, J., et al., *Modeling the dynamics of hypoxia inducible factor-1α (HIF-1α) within single cells and 3D cell culture systems.* Mathematical Biosciences, 2014. **258**: p. 33-43.
129. Ganapathy, V., M. Thangaraju, and P.D. Prasad, *Nutrient transporters in cancer: relevance to Warburg hypothesis and beyond.* Pharmacology and Therapeutics, 2009. **121**(1): p. 29-40.

130. Muzi, M., et al., *Kinetic characterization of hexokinase isoenzymes from glioma cells: implications for FDG imaging of human brain tumors.* Nuclear Medicine and Biology, 2001. **28**(2): p. 107-116.
131. Malatesha, G., et al., *Comparison of arterial and venous pH, bicarbonate, PCO_2 and PO_2 in initial emergency department assessment.* Emergency Medicine Journal, 2007. **24**(8): p. 569-571.
132. Walkey, A.J., et al., *The accuracy of the central venous blood gas for acid–base monitoring.* Journal of Intensive Care Medicine, 2009. **25**(2): p. 104-10.
133. Gullino, P.M., S.H. Clark, and F.H. Grantham, *The interstitial fluid of solid tumors.* Cancer Research, 1964. **24**(5): p. 780-797.
134. Gullino, P.M., et al., *Modifications of the acid-base status of the internal milieu of tumors.* Journal of the National Cancer Institute, 1965. **34**(6): p. 857-869.
135. Casciari, J.J., S.V. Sotirchos, and R.M. Sutherland, *Glucose diffusivity in multicellular tumor spheroids.* Cancer Research, 1988. **48**(14): p. 3905-3909.
136. Fatt, I., C.J. Giasson, and T.D. Mueller, *Non-steady-state diffusion in a multilayered tissue initiated by manipulation of chemical activity at the boundaries.* Biophysical Journal, 1998. **74**(1): p. 475-486.
137. Rivenzon-Segal, D., et al., *Glucose transporters and transport kinetics in retinoic acid-differentiated T47D human breast cancer cells.* American Journal of Physiology-Endocrinology and Metabolism, 2000. **279**(3): p. E508-E519.
138. Rodr ́guez-Enr ́quez, S., et al., *Kinetics of transport and phosphorylation of glucose in cancer cells.* Journal of Cellular Physiology, 2009. **221**(3): p. 552-559.
139. Smith, T.A., et al., *Decreased [18F] fluoro-2-deoxy-d-glucose incorporation and increased glucose transport are associated with resistance to 5FU in MCF7 cells in vitro.* Nuclear Medicine and Biology, 2007. **34**(8): p. 955-960.
140. Burrows, R.C., et al., *[18F]-2-fluoro-2-deoxyglucose transport kinetics as a function of extracellular glucose concentration in malignant glioma, fibroblast and macrophage cells in vitro.* Nuclear Medicine and Biology, 2004. **31**(1): p. 1-9.
141. Halestrap, A. and N. Price, *The proton-linked monocarboxylate transporter (MCT) family: structure, function and regulation.* Biochemical Journal, 1999. **343**: p. 281-299.
142. Mar ́n-Hern ́ndez, A., et al., *Determining and understanding the control of glycolysis in fast-growth tumor cells.* FEBS Journal, 2006. **273**(9): p. 1975-1988.
143. Fox, J.E.M., D. Meredith, and A.P. Halestrap, *Characterisation of human monocarboxylate transporter 4 substantiates its role in lactic acid efflux from skeletal muscle.* The Journal of Physiology, 2000. **529**(2): p. 285-293.
144. Aloj, L., et al., *Glut-1 and Hexokinase Expression Relationship with 2-Fluoro-2-deoxy-d-glucose Uptake in A431 and T47D Cells in Culture.* Cancer Research, 1999. **59**(18): p. 4709-4714.
145. Jackson, V.N. and A.P. Halestrap, *The kinetics, substrate, and inhibitor specificity of the monocarboxylate (lactate) transporter of rat liver cells determined using the fluorescent intracellular pH indicator, 2', 7'-bis (carboxyethyl)-5 (6)-carboxyfluorescein.* Journal of Biological Chemistry, 1996. **271**(2): p. 861-868.
146. Semenza, G.L., *Targeting HIF-1 for cancer therapy.* Nat Rev Cancer, 2003. **3**(10): p. 721-732.
147. Llopart, X., et al., *Timepix, a 65k programmable pixel readout chip for arrival time, energy and/or photon counting measurements.* Nuclear Instruments and Methods in Physics Research Section A: Accelerators, Spectrometers, Detectors and Associated Equipment, 2007. **581**(1–2): p. 485-494.
148. Llopart, X., et al., *Medipix2: a 64-k pixel readout chip with 55-μm square elements working in single photon counting mode.* IEEE Transactions on Nuclear Science, 2002. **49**(5): p. 2279-2283.
149. Žemlička, J., et al., *Energy-and position-sensitive pixel detector Timepix for X-ray fluorescence imaging.* Nuclear Instruments and Methods in Physics Research Section A: Accelerators, Spectrometers, Detectors and Associated Equipment, 2009. **607**(1): p. 202-204.

150. Jakubek, J., et al., *A coated pixel device TimePix with micron spatial resolution for UCN detection.* Nuclear Instruments and Methods in Physics Research Section A: Accelerators, Spectrometers, Detectors and Associated Equipment, 2009. **600**(3): p. 651-656.
151. Allison, J., et al., *Geant4 developments and applications.* IEEE Transactions on Nuclear Science, 2006. **53**(1): p. 270-278.
152. Bouchami, J., et al., *Study of charge sharing in a silicon pixel detector with heavy ionizing particles interacting with a Medipix2 device.* Nuclear Instruments and Methods in Physics Research Section A: Accelerators, Spectrometers, Detectors and Associated Equipment, 2009. **607**(1): p. 196-198.
153. Nilsson, H.E., C. Frojdh, and E. Dubaric, *Monte Carlo simulation of charge sharing effects in silicon and GaAs photon-counting x-ray imaging detectors.* IEEE Transactions on Nuclear Science, 2004. **51**(4): p. 1636-1640.
154. Lam, C., et al., *Positron lifetime studies on 8 MeV electron-irradiated n-type 6H silicon carbide.* Journal of Physics: Condensed Matter, 2004. **16**(46): p. 8409-8419.
155. Hsu, C.-W., C.-C. Chang, and C.-J. Lin, *A practical guide to support vector classification*. 2003.
156. Russo, P., et al., *18F-FDG positron autoradiography with a particle counting silicon pixel detector.* Physics in Medicine and Biology, 2008. **53**(21): p. 6227-6243.
157. Wang, Q., et al., *Evaluation of Timepix silicon detector for the detection of 18F positrons.* Journal of Instrumentation, 2014. **9**(5): p. C05067.
158. Jakubek, J., *Precise energy calibration of pixel detector working in time-over-threshold mode.* Nuclear Instruments and Methods in Physics Research Section A: Accelerators, Spectrometers, Detectors and Associated Equipment, 2011. **633**: p. S262-S266.
159. Vaupel, P., M. Höckel, and A. Mayer, *Detection and characterization of tumor hypoxia using pO_2 histography.* Antioxidants & Redox Signaling, 2007. **9**(8): p. 1221-1236.
160. Vaupel, P., et al., *O_2 extraction is a key parameter determining the oxygenation status of malignant tumors and normal tissues.* International Journal of Oncology, 2003. **22**(4): p. 795-798.
161. Vaupel, P., *The role of hypoxia-induced factors in tumor progression.* The Oncologist, 2004. **9**(Supplement 5): p. 10-17.
162. Zhang, X., Y. Lin, and R.J. Gillies, *Tumor pH and its measurement.* Journal of Nuclear Medicine, 2010. **51**(8): p. 1167-1170.
163. Vaupel, P., F. Kallinowski, and P. Okunieff, *Blood flow, oxygen and nutrient supply, and metabolic microenvironment of human tumors: a review.* Cancer Research, 1989. **49**(23): p. 6449-6465.
164. Lee, T.S., et al., *Comparison of 18 F-FDG, 18 F-FET and 18 F-FLT for differentiation between tumor and inflammation in rats.* Nuclear Medicine and Biology, 2009. **36**(6): p. 681-686.
165. Piert, M., et al., *Positron detection for the intraoperative localisation of cancer deposits.* European Journal of Nuclear Medicine and Molecular Imaging, 2007. **34**(10): p. 1534-1544.
166. Dellian, M., et al., *Fluorescence ratio imaging of interstitial pH in solid tumours: effect of glucose on spatial and temporal gradients.* British Journal of Cancer, 1996. **74**(8): p. 1206-1215.
167. Kunz-Schughart, L.A., W. Mueller-Klieser, and P. Vaupel, *Tumorpathophysiologie.* Strahlentherapie und Onkologie, 2012. **188**(3): p. 299-303.
168. Young, C.D., et al., *Modulation of glucose transporter 1 (GLUT1) expression levels alters mouse mammary tumor cell growth in vitro and in vivo.* PloS One, 2011. **6**(8): p. e23205.
169. Gilkes, D.M. and G.L. Semenza, *Role of hypoxia-inducible factors in breast cancer metastasis.* Future Oncology, 2013. **9**(11): p. 1623-1636.
170. Semenza, G.L., *HIF-1 mediates metabolic responses to intratumoral hypoxia and oncogenic mutations.* The Journal of Clinical Investigation, 2013. **123**(9): p. 3664-3671.
171. Macheda, M.L., S. Rogers, and J.D. Best, *Molecular and cellular regulation of glucose transporter (GLUT) proteins in cancer.* Journal of Cellular Physiology, 2005. **202**(3): p. 654-662.

172. Mobasheri, A., et al., *Hypoxia inducible factor-1 and facilitative glucose transporters GLUT1 and GLUT3: putative molecular components of the oxygen and glucose sensing apparatus in articular chondrocytes.* Histology and Histopathology, 2005. **20**(4): p. 1327-1338.
173. Riddle, S.R., et al., *Hypoxia induces hexokinase II gene expression in human lung cell line A549.* American Journal of Physiology-Lung Cellular and Molecular Physiology, 2000. **278**(2): p. L407-L416.
174. Höckel, M. and P. Vaupel. *Biological consequences of tumor hypoxia*. in *Seminars in Oncology*. 2001. Elsevier.
175. Kallinowski, F., et al., *Tumor blood flow: the principal modulator of oxidative and glycolytic metabolism, and of the metabolic micromilieu of human tumor xenografts in vivo.* International journal of cancer, 1989. **44**(2): p. 266-272.
176. Kallinowski, F., et al., *Glucose uptake, lactate release, ketone body turnover, metabolic micromilieu, and pH distributions in human breast cancer xenografts in nude rats.* Cancer Research, 1988. **48**(24): p. 7264-7272.
177. Kallinowski, F., et al., *Blood flow, metabolism, cellular microenvironment, and growth rate of human tumor xenografts.* Cancer Research, 1989. **49**(14): p. 3759-3764.
178. Park, S.G., et al., *Biologic correlation between glucose transporters, hexokinase-II, Ki-67 and FDG uptake in malignant melanoma.* Nuclear Medicine and Biology, 2012. **39**(8): p. 1167-1172.
179. Shim, H.K., et al., *Relationship between FDG uptake and expressions of glucose transporter type 1, type 3, and hexokinase-II in Reed-Sternberg cells of Hodgkin lymphoma.* Oncology Research Featuring Preclinical and Clinical Cancer Therapeutics, 2009. **17**(7): p. 331-337.
180. Semenza, G.L. *Regulation of cancer cell metabolism by hypoxia-inducible factor 1*. in *Seminars in Cancer Biology*. 2009. Elsevier.
181. Vaupel, P., *Atemgaswechsel und Glucosestoffwechsel von Implantationstumoren (DS-Carcinosarkom) in vivo: experimentelle Untersuchungen u. theoret. Analysen z. Frage d. krit. Sauerstoff-u. Glucoseversorgung im Tumorgewebe*. 1974: Akademie der Wiss. ud Literatur.
182. Žemlička, J., et al., *Energy- and position-sensitive pixel detector Timepix for X-ray fluorescence imaging.* Nuclear Instruments and Methods in Physics Research Section A: Accelerators, Spectrometers, Detectors and Associated Equipment, 2009. **607**(1): p. 202-204.
183. Zou, K.H., et al., *Statistical validation of image segmentation quality based on a spatial overlap index* Academic Radiology, 2004. **11**(2): p. 178-189.
184. Arora, N.D., J.R. Hauser, and D.J. Roulston, *Electron and hole mobilities in silicon as a function of concentration and temperature.* IEEE Transactions on Electron Devices, 1982. **29**(2): p. 292-295.
185. Charon, Y., P. Laniece, and H. Tricoire, *Radio-imaging for quantitative autoradiography in biology.* Nuclear Medicine and Biology, 1998. **25**(8): p. 699-704.

Publications, book chapter and conference talks

- **Qian Wang**, Zhen Liu, Sibylle I. Ziegler, Kuangyu Shi, 2015, Enhancing spatial resolution of 18F positron imaging with Timepix detector by classification of primary fired pixels using support vector machine, *Physics in Medicine and Biology*, **60**(13), 5261-5278
- **Qian Wang**, Peter Vaupel, Sibylle I. Ziegler, Kuangyu Shi, 2015, Exploring the quantitative relationship between metabolism and enzymatic phenotype by physiological modeling of glucose metabolism and lactate oxidation in solid tumors, *Physics in Medicine and Biology*, **60**(6), 2547-2571
- **Qian Wang**, Jan Tous, Zhen Liu, Sibylle I. Ziegler, and Kuangyu Shi, 2014, Evaluation of Timepix silicon detector for the detection of 18F positrons, *Journal of Instrument*, **9**, C05067
- **Qian Wang**, Zhen Liu, Sibylle I. Ziegler, Kuangyu Shi, 2015, A reaction diffusion simulation model of [18F]FDG PET imaging for the quantitative interpretation of cancerous metabolism (*Series Title: Lecture Notes in Computational Vision and Biomechanics; Book: Computational Methods for Molecular Imaging*), Springer, **22**, 123-137
- **Qian Wang**, Exploring the metabolite sensitivity to enzyme expression by physiological modeling of glucose metabolism and lactate oxidation in solid tumors, *Society of Nuclear Medicine and Molecular Imaging*, St. Louis, United States, Jun. 2014
- **Qian Wang**, Enhancing spatial resolution of Timepix positron camera based on classification of primary interactions using SVM, *IEEE Medical Imaging Conference*, Seoul, Korea, Oct. 2013
- **Qian Wang**, A reaction diffusion simulation model of [18F]FDG PET imaging for the quantitative interpretation of cancerous metabolism, *IEEE Medical Imaging Conference*, Valencia, Spain, Oct. 2011